Technical University of Denmark

DTU

Wind Turbines: Unsteady Aerodynamics and Inflow Noise

Broe, Brian Riget; Mann, Jakob; Aagaard Madsen , Helge; Sørensen, Jens Nørkær

Publication date:
2009

Document Version
Publisher's PDF, also known as Version of record

Link back to DTU Orbit

DTU Library
Technical Information Center of Denmark

Wind Turbines: Unsteady Aerodynamics and Inflow Noise

Brian Riget Broe
Risø-PhD-47(EN)
December 2009
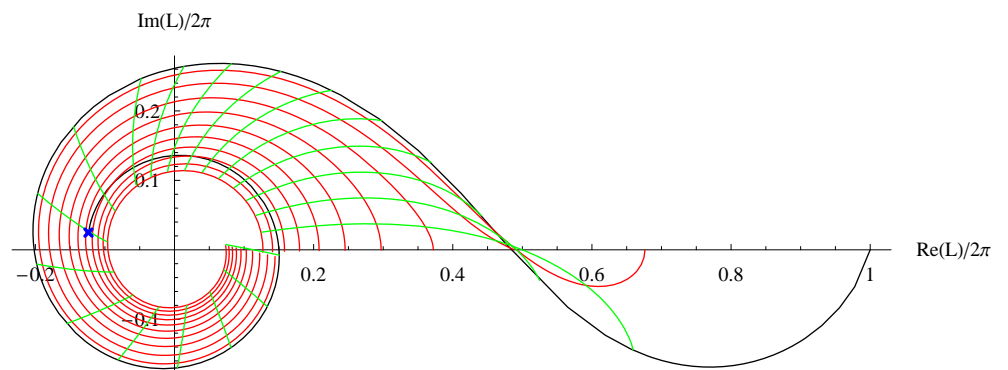
Figure on front page:

Plot of the lift response of a sinusoidal gust as function of reduced wave number. The black line is the 1-D sinusoidal gust on a flat aerofoil (Section 2.1.2). The absolute value of the lift response $|L|$ is the distance from the origin of the plot to a point on, say, the black line. The argument of L is the corresponding phase of the lift relative to the phase of the gust at the midpoint of the aerofoil to the gust. The green and red lines show a 2-D sinusoidal gust on a 2-D flat aerofoil (Section 2.1.4). The red lines are functions of the chordwise wave number for different values of fixed spanwise wave number. The green lines are functions of the spanwise wave number when the chord wise wave number is fixed.

Author: Brian Riget Broe
Title: Wind Turbines: Unsteady Aerodynamics and Inflow Noise
Division: Wind Energy Division

Abstract (max. 2000 char.):
Aerodynamical noise from wind turbines due to atmospheric turbulence has the highest emphasis in semi-empirical models. However it is an open question whether inflow noise has a high emphasis. This illustrates the need to investigate and improve the semi-empirical model for noise due to atmospheric turbulence. Three different aerodynamical models are investigated in order to estimate the lift fluctuations due to unsteady aerodynamics (Sears, W. R.: 1941, Some aspects of non-stationary airfoil theory and its practical application; Goldstein, M. E. and Atassi, H. M.: 1976, A complete second-order theory for the unsteady flow about an airfoil due to a periodic gust; and Graham, J. M. R.: 1970, Lifting surface theory for the problem of an arbitrarily yawed sinusoidal gust incident on a thin aerofoil in incompressible flow). Two of these models are investigated to find the unsteady lift distribution or pressure difference as function of chordwise position on the aerofoil (Sears, W. R.: 1941; and Graham, J. M. R.: 1970). An acoustic model is investigated using a model for the lift distribution as input (Amiet, R. K.: 1975, Acoustic radiation from an airfoil in a turbulent stream). The two models for lift distribution are used in the acoustic model. One of the models for lift distribution is for completely anisotropic turbulence and the other for perfectly isotropic turbulence, and so is also the corresponding models for the lift fluctuations derived from the models for lift distribution. The models for lift distribution and lift are compared with pressure data which are obtained by microphones placed flush with the surface of an aerofoil. The pressure data are from two experiments in a wind tunnel, one experiment with a NACA0015 profile and a second with a NACA63415 profile. The turbulence is measured by a triple wired hotwire instrument in the experiment with a NACA0015 profile. Comparison of the aerodynamical models with data shows that the models capture the general characteristics of the measurements, but the data are hampered by background noise from the fan propellers in the wind tunnel. The measurements are in between the completely anisotropic turbulent model and the perfectly isotropic turbulent model. This indicates that the models capture the aerodynamics well. Thus the measurements suggest that the noise due to atmospheric turbulence can be described and modeled by the two models for lift distribution. It was not possible to test the acoustical model by the measurements presented in this work.

www.risoe.dtu.dk

Acknowledgements

I thank my supervisors, Jakob Mann at Risø DTU, and Jens Nørkær Sørensen, for the valuable discussions in the course of this work.

This work was never done without the moral support and fruitful discussions with Sven-Erik Gryning. Further Lise Lotte Sørensen has contributed with moral support, which has been highly appreciated.

I also use the opportunity to express my gratitude to my colleagues in the Wind Energy Department at Risø DTU for their support in the course of the Ph.D. study.

Contents

Nomenclature

a	Dimensionless constant in Section 2.4.
a_i	Acceleration in Section 2.2.
a_y	Vertical acceleration in aerofoil plane.
a_n	Normal acceleration in cylinder plane.
$A(\rho, c, U)$	Amplification factor. $A(\rho, c, U) = \frac{1}{2}\rho c U$
A_d	Admittance.
A_{ij}	Coefficients defined in Section 2.1.4.
A_m	Coefficient for the complex acceleration potential, $m \geq 0$.
b	Half chord, $b = \frac{c}{2}$.
B	Length of bridge section.
B_{ij}	Coefficients defined in Section 2.1.4.
c	Chord length.
c_0	Speed of sound in air, $c_0 = 340\text{m/s}$.
$c_h(z)$	Coefficient, $c_h(z) = -\frac{\sin(h \arccos(z))}{h}$, $h \geq 1$, $c_0(z) = \frac{\pi}{2} + \arcsin(z)$.
coh_{ww}	Coherence of vertical turbulence.
$coh_{ww}^{1/2}$	Co-coherence of vertical turbulence.
$coh_{LL}^{1/2}$	Co-coherence of lift.
$C(\kappa)$	Theodorsen function, $C(\kappa) = \frac{K_1(\imath\kappa)}{K_0(\imath\kappa)+K_1(\imath\kappa)}$.
d	Half span.
d_1	Diameter of hole flush with surface of aerofoil.
d_2	Diameter of microphone membrane.
$E(k)$	Total turbulent kinetic energy.
$E_A(\kappa)$	Function defined in Section 2.1.3.
$E_v[\,]$	Expected value.
f	Cyclic frequency.
$f(D, d)$	Function defined in Section 2.4.
f_c	Center frequency in the one third octave band.
f_h	Upper frequency in the one third octave band.
f_l	Lower frequency in the one third octave band.
f_H	Eigenfrequency of a Helmholtz resonator.
$f_{0w}(x)$	Functions defined in Section 2.1.4, $w \in \{1, 2, 3\}$.

$f_w(z)$	$f_w(z) = f_{0w}(x)$.
F	Acoustic force.
$F(z)$	Function defined in Section 2.1.4.
$F_\pm(z)$	Function defined in Section 2.1.3.
$\mathbf{g}$	Acceleration due to gravity in Section 2.1.1.
g_z	Vertical acceleration due to gravity in Section 2.1.1.
g	Transfer function for either lift distribution or lift.
$G(\hat{\omega})$	Transfer function for lift distribution.
$G_A(z)$	Function defined in Section 2.1.3.
h_1	Length of tube.
h_2	Height to estimate V in Eqn. (3.2).
h_3	Height to estimate V in Eqn. (3.2).
$H_n^{(1)}(z)$	Bessel functions of third kind (Hankel functions) of order n.
$H_\pm(z)$	$H_0^{(1)}(z) \pm \imath H_1^{(1)}(z)$.
$\imath$	Imaginary unit in the complex time domain.
I	Turbulence intensity, $I = \frac{\sqrt{\sigma_U^2}}{U}$.
I_{wt}	Turbulence intensity at tip speed of wind turbine.
j	Imaginary unit in the spatial complex plane.
J_n	Bessel function of first kind of order n.
$J_\pm(z)$	$J_0(z) \pm \imath J_1(z)$.
k_c	$\kappa + \imath\mu$ in Section 2.1.4.
k	Wave number vector.
$\mathbf{k}$	Wave number vector.
k_e	$\frac{\sqrt{\pi}}{L}\frac{\Gamma(5/6)}{\Gamma(1/3)}$.
k_x	Chordwise wave number, $\frac{\omega}{U}$.
$\hat{k}_x$	k_x/k_e.
k_y	Spanwise wave number.
$\hat{k}_y$	k_y/k_e.
k_1	Chordwise wave number.
k_2	Spanwise wave number.
k_3	Vertical wave number.
K_n	Modified Bessel function of second kind of order n.
K_x	$-\frac{\omega}{U}$.
$\hat{K}_x$	K_x/k_e.
$K_1'(z)$	$K_1(z),\ z > 0,\ K_1(-z),\ z < 0,\ \pm\infty,\ z = 0$.
l	Lift distribution, $\Delta p(x)$, on aerofoil.
$\mathbf{L}$	Lift force vector.
L	Absolute value of lift in Section 2.1.1.
L_T	Length scale of turbulence.
L'	lift fluctuation.

L'_e Effective length of a flanged tube, $L' = h_1 + 1.7d_1/2$, in Section 3.1.

L_β Response (transfer) function of lift due to AOA.

L_m Response (transfer) function of lift due to camber.

$\mathcal{L}$ Acoustic lift.

m Second order fit coefficient to camber line.

M Mach number, $\frac{U}{c_0}$.

$\mathbf{n}$ Vector of unit length.

N Normal force.

$o(z)$ Complex acceleration potential, $o(z) = \phi(z) + j\psi(z)$.

$O(z)$ Complex velocity potential.

p Pressure.

P_m Coefficient, $P_m = (-\imath)^m J_m(\kappa)$.

P_1 Acoustic pressure at receiver position in Section 2.4.

r Radius of cylinder.

r_1 $2\cos\theta_1$.

R Distance of integration.

R_{pp} Cross correlation of pressure.

R_T Total response (transfer) function of lift in 2-D model

s Distance along surface of aerofoil from leading edge.

$S(\kappa)$ Sears function, $S(\kappa) = 2\pi[\{J_0(\kappa) - \imath J_1(\kappa)\}C(\kappa) + \imath J_1(\kappa)]$.

S Integration domain of aerofoil surface in Section 2.1.4.

S_{cav} Area, $S_{cav} = \pi(d_1/2)^2$, in Section 3.1.

$Si(x)$ Sine integral. $Si(x) = \int_0^x \frac{\sin t}{t} dt$.

S_p Pressure spectrum.

S_L Lift spectrum.

S_{PP} Cross spectrum of acoustic pressure.

S_{QQ} Cross spectrum of pressure difference.

S_U Spectrum of turbulent velocity in direction of mean flow.

S_V Spectrum of Volt signal in Chapter 3.1.

S_V Spectrum of turbulent horizontal velocity perpendicular to mean flow.

S_W Spectrum of turbulent vertical velocity.

S_{var} Spectrum of variable var.

t Time.

T_F Tangential force in Section 2.1.1.

T Limit of time integration in Section 2.4.

$T_i(z)$ Chebychev polynomial of ith order, $T_i(z) = \cos(i\arccos(z))$.

$\mathbf{u}$ Velocity vector.

u Amplitude of chordwise gust in Section 2.1.3.

u_* Friction velocity.

$\overline{u^2}$ Variance of velocity in direction of mean flow.

U Velocity in direction of mean flow.

U_{wt} Tip speed of wind turbine.

$U(z)$ Logarithmic wind profile.

U_∞ Mean velocity in direction of mean flow.

v_{1D} 1-D gust in Section 2.1.2.

v_{3D} vertical gust in Section 2.1.4.

V_{cav} Volume between tube and microphone membrane in Section 3.1.

V Horizontal velocity perpendicular to mean flow.

w vertical gust

$\hat{\hat{w}}$ Fourier amplitude of vertical velocity.

w_F Fourier amplitude of vertical velocity at a given mode in Section 2.4.

w_0 Upwash at aerofoil.

w_1 Upwash in wake.

W_w Integration domain over the wake in Section 2.1.4.

W Vertical velocity (z-direction).

x Chordwise coordinate.

x_0 Chordwise coordinate restricted to the aerofoil in Section 2.1.4.

y_t Coordinate transformation, $y_t = \frac{k_y}{1+k_y}$, in Section 4.1.1.

y Spanwise coordinate.

y_0 Spanwise coordinate restricted to the aerofoil in Section 2.1.4.

z_c Complex coordinate, $z_c = x + jz$ in Section 2.1.1 and Section 2.1.2.

z_n Normalized chordwise coordinate, $z_n = \frac{2x}{c} - 1$ in Section 2.1.4.

z_v Variable, which can be both complex and real.

z Vertical coordinate.

$z_{n,0}$ Normalized chordwise coordinate, $z_{n,0} = \frac{2x_0}{c} - 1$ in Section 2.1.4.

$z_{0,R}$ Rougness length in Section 4.4.

α_{AOA} Angle of attack (AOA) in Section 2.1.1.

α Spectral Kolmogorov constant set to 1.7.

α_{cor} Free stream corrected AOA.

β_t Angle to the horizontal of the trailing edge in the aerofoil plane in Section 2.1.1.

β $\sqrt{1 - M^2}$ in Section 2.4.

β_A AOA in radians, $\beta = \frac{AOA}{180°}\pi$.

γ Constant.

γ_1 Chordwise vorticity.

γ_2 Spanwise vorticity.

Γ Gamma function.

$\delta()$ Dirac Delta function.

δ_{ij} Kroenecker delta, $\delta_{ij} = 0$, $i \neq j$, $\delta_{ij} = 1$, $i = j$,.

Δf The width of a frequency band in the one third octave band.

Δp Pressure difference of pressure fluctuations.

ΔP Pressure difference.

ΔP_T Pressure difference in Fourier space (frequency domain).

ϵ Energy dissipation rate.

ζ Complex coordinate in the aerofoil plane.

η Separation distance, $\eta = y_2 - y_1$.

θ Complex argument, $e^{j\theta}$, in the cylinder plane.

θ_1 $\frac{\theta}{2}$.

$\Theta_\pm$ Function defined in Section 2.1.3.

κ_c Circulation in Section 2.1.1.

κ_K von Kármán constant set to 0.4 in Section 4.4.

κ Reduced chordwise wavenumber, $\kappa = \frac{k_x c}{2}$.

λ Joukowski parameter in Section 2.1.1.

$\Lambda_\pm$ Function defined in Section 2.1.3.

μ Vertical reduced wave number, $\mu = \frac{k_z c}{2}$, in Section 2.1.3.

ν Reduced spanwise wave number, $\nu = \frac{k_y c}{2} = \frac{\mu c}{2}$.

ν_k Kinematic viscosity $\sim 1.6 \cdot 10^{-5} \mathrm{m}^2/\mathrm{s}$.

ρ Air density.

ρ_0 Mean air density.

σ Auxiliary distance parameter, $\sigma = \sqrt{x^2 + \beta^2(y^2 + z^2)}$.

σ_i Chebychev coefficient.

σ_{var} Standard deviation of variable var.

σ_{var}^2 Variance of variable var.

τ Time.

ϕ_v Velocity potential in Section 2.1.1.

ϕ Acceleration potential.

Φ_{ij} Energy spectrum of turbulence by von Kármán in velocity components ij.

Φ_{ww} Energy spectrum of turbulence by von Kármán of vertical velocities.

χ_{ww} Cross spectrum of vertical turbulence.

χ_{LL} Cross spectrum of lift.

ψ Streamlines of acceleration.

ω Vorticity in Section 2.1.1.

ω Angular frequency.

$\hat{\omega}$ Reduced angular frequency, $\hat{\omega} = \frac{\omega b}{U}$.

$\overline{(\ )}$ Complex conjugate.

$\langle\ \rangle$ Mean of quantity in $\langle\ \rangle$.

Chapter 1

Introduction

Noise from wind turbines is a subject which has a considerable public interest in Denmark. It is a subject of much debate before establishing wind turbines at any site. Therefore it is important to gain knowledge of noise from wind turbines.

The noise from wind turbines can be split up into two major sources, a mechanical source and an aero acoustic source (Wagner, Bareiß and Guidati 1996). The mechanical source of noise can be avoided or minimized by engineering means (Henderson 2005). The aero acoustic part can not be avoided but the design of the aerofoil has an important role of how much noise is produced by aero acoustical means.

The aero acoustic source is due to turbulence in the flow around the wind turbine blades. The turbulence is generated by different mechanisms such as atmospheric turbulence and separation and thus the aero acoustic source can be split up into several components (Wagner et al. 1996).

The aero acoustic noise due to atmospheric turbulence is the subject of this thesis. It is also called inflow noise. The atmospheric flow is not steady but contains eddies, turbulence (Panofsky and Dutton 1984). The pressure at any point is constant in time when the flow is steady, incompressible, and inviscid. The turbulence create pressure fluctuations. Some part of the pressure fluctuations caused by the turbulence will be emitted as sound (Amiet 1975). The nature of turbulence causes the noise to be emitted in a continuum of frequencies and the inflow noise is of broadband character (Wagner et al. 1996).

The aeroacoustic noise can be treated by computational fluid dynamics (Zhu 2007) which is time consuming and demands powerful computer resources, or it can be treated in a semi-empirical approach which simplifies the physics (Amiet 1975).

The inflow noise has been treated in a semi-empirical approach (Amiet
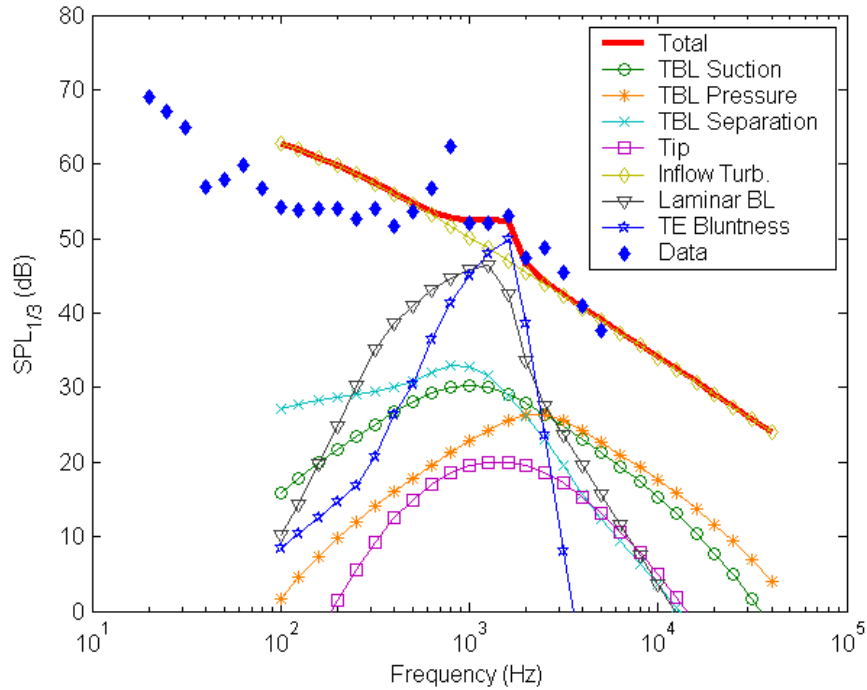
Figure 1.1: Plot of the $SPL_{1/3}$ at the one third octave frequencies for aero acoustic sources described in Moriarty and Migliore (2003). This figure is identical to Figure 9 in Moriarty and Migliore (2003).

1975). The semi-empirical approach has the advantage that it is less demanding on computer resources as compared to approaches based on computational fluid dynamics. The semi-empirical approach is suitable for guidelines for design purposes because an answer is quickly obtained when design parameters are changed.

The semi-empirical inflow model, which is widely used, accounts for the major part of the total aero acoustical noise, Moriarty and Migliore (2003), as seen in Figure 1.1. According to this model inflow noise is seen to be dominating. Some experimental evidence indicates, however, that inflow noise is not the most significant aero acoustic component (Personal communication, P. Moriarty). Trailing edge noise is argued to be responsible for major part of the noise emitted aero acoustically (Moriarty and Migliore 2003, Oerlemans, Sijtsmaa and López 2007).

It follows from the discussion above that the semi-empirical model of noise due to atmospheric turbulence must be revised because it has too much emphasis of the total aero acoustical noise compared to trailing edge noise. Other approaches to improve the semi-empirical noise model due to atmo-

spheric turbulence have been carried out by Guidati (2004) and by Moriarty, Guidati and Migliore (2005). The input models by Sears (1941), Goldstein and Atassi (1976), and Graham (1970) in the acoustical model by Amiet (1975) are investigated in this thesis.

The model of inflow noise shown in Figure 1.1 is based on the model by Amiet (1975). This model assumes that the noise due to atmospheric turbulence is emitted like a dipole. It is based on isotropic turbulence as described by von Kármán (1948), and the lift distribution (pressure difference) due to turbulence along the chord of the aerofoil described by Adamczyk (1974).

The lift distribution due to turbulence is also described by Sears (1941) and Graham (1970). The models by Adamczyk (1974), Sears (1941), and Graham (1970) are all based on a flat plate. Further a model for the fluctuating lift due to turbulence is described, where the aerofoil is a bend flat plate at an angle of attack (Goldstein and Atassi 1976, Atassi 1984).

This work will focus on the aerodynamical basis of the acoustical model by Amiet (1975). Experiments have been conducted that investigate the aerodynamical pressure at discrete points of two sections of an aerofoil. The aerofoils that are investigated are a NACA0015 profile and a NACA63415 profile. The effects of camber and angle of attack (AOA) on the fluctuating aerodynamical pressure are investigated. The effect of thickness is not investigated because the two profiles have identical thicknesses.

The flow is considered not to be affected by viscous effects. It is seen in Figure 1.1 that neglecting viscous effects may be reasonable because it appears from these semi-empirical models that those contributions are dominated by the inflow noise. Inflow noise is of broad band character.

The problem handled in this thesis is aerodynamical noise from wind turbines due to atmospheric turbulence. The characteristics of the flow in that context are described below. The relative mean velocity of the flow, U, is up to 80m/s at the span wise point where the source of noise is most significant (Oerlemans et al. 2007), and this gives a Mach number, $M = \frac{U}{c_0} \sim 0.25$, where c_0 is the speed of sound. The Mach number in the experiments is ~ 0.1 because the highest wind speed available in the wind tunnel used is 40m/s. The aerodynamical models do not depend on Mach number because of assumed incompressibility but the acoustical model does.

Another characteristic of the flow is the Reynolds number based on the the chord length, $R_e = \frac{Uc}{\nu_k}$, where c is the chord length and ν_k is the kinematic viscosity. The Reynolds number in the experiments described in this work are between $\sim 1.0 \cdot 10^6$ and $\sim 3.0 \cdot 10^6$ whereas in the atmosphere it would be $\sim 4.0 \cdot 10^6$. The models assume that $R_e \rightarrow \infty$ or equivalently that $\nu_k \approx 0$.

The typical turbulence length scale in the atmosphere is comparable to the hub height of present wind turbines, which is ~ 70m, and furthermore

the turbulence is not isotropic because the length scale in the direction of mean flow is typically larger than the scales perpendicular to the mean flow. The turbulence model applied in this work assumes isotropy which simplifies the mathematics.

The experiments on which this thesis is based do not meet the flow conditions of the atmosphere completely.

This thesis is organized in 3 chapters: a chapter that describes the models used, a chapter that describes data from two experiments conducted on two different profiles, and a chapter that compares data from experiments with models.

Both the aerodynamically and the acoustical models are described. Details of the derivation of the models are shown.

The experiments were carried out in a wind tunnel. Two different profiles were used, a NACA0015 and a NACA63415 profile. The data from these experiments are obtained by various means to get the properties of the flow such as angle of attack, mean wind speed, turbulence and surface pressure at the aerofoil.

Chapter 2

Theory and Models

This chapter discusses and derives the models used in this thesis. The models are aerodynamical, turbulence, and acoustical models.

The aerodynamical models describe the unsteady aerodynamics when an aerofoil is subject for incoming turbulence. They are based on potential theory and the incompressible and inviscid form of Navier-Stokes equations which are linearized.

Isotropic turbulence is discussed and a model is shown that gives the energy spectrum of the isotropic turbulence as well as the coherence of turbulence. The turbulence model is used to estimate pressure and lift spectra together with the aerodynamical models.

The acoustical model predicts the noise due to turbulence in the incoming flow. The model is based on that the force which is responsible for emitting sound pressure is acting as a dipole.

The width and thickness of a real wind turbine blade is not constant in the spanwise direction, and this causes that the flow will develop aerodynamics with 3-D characteristics and one section of the aerofoil will not have the same characteristics as another section. Further the length of a wind turbine blade is finite, and this causes yet other 3-D characteristics where the aerofoil ends. However, it is for the aerodynamical models assumed that strip theory can be applied in order that 3-D effects and tip-effects can be neglected.

The aerodynamics and acoustics are treated as if the aerofoil is fixed and not influenced by the presence of more aerofoils and the noise is radiated from one aerofoil only. The mean wind is perpendicular to the rotor plane, but the movement of a wind turbine blade makes the relative wind coming at an angle that is relatively small relatively to the chord line, such that theories of unsteady aerodynamics are applicable. The turbulence generated by the blade is assumed to be advected away from the rotor plane. It then follows that it can be assumed as a first approximation that the blade is not

influenced by the wake of the other blades (for typically three bladed wind
turbines). The inflow model by Amiet (1975) is used in wind turbine appli-
cations (Lowson 1994) without any consideration of the number of blades or
their wakes. This seems a reasonable assumption in the light of Oerlemans
et al. (2007) where it is found that the main source of aerodynamical noise is
in a radius of approximately two thirds of the length of blade from the center
and is in position of approximately 2 O'clock when measured and visualized
in front of the rotor plane.

The models in this chapter are used throughout this thesis and are orig-
inated from three different fields, aerodynamics, turbulence, and acoustics.
The use of three different fields causes problems regarding the usual notation
in each field, thus the symbols might be different than usual.

2.1   Aerodynamics

Aerodynamics is a broad field, and this text will cover the basics needed to
understand the flow around an aerofoil. Steady flow and pressure fluctuations
due to a gust in one, two, and three dimensions will be discussed.

The dimensions of the unsteady models in this thesis are defined by the
author and might deviate from other texts in the definition. The different
definition is made to make it easy to distinguish between models throughout
the thesis. The model by Sears (1941) is regarded as a 1-D theory because it
is treating a flat plate without any spanwise effects and with no angle to the
mean flow. The model by Goldstein and Atassi (1976) and Atassi (1984) is
defined as a 2-D model because it is a profile of an aerofoil, though infinitely
thin. The 2-D model has no spanwise effects as well. The model by Graham
(1970) is regarded as a 3-D model because it includes spanwise effects from
a vertical gust.

The theory for unsteady flow is treated for both the case of a flat plate
and for an angle of attack (AOA) of zero in 1-D and 3-D. The unsteady flow
in 2-D is treated for a flat plate with camber and an arbitrary AOA. In the
case of unsteady aerodynamics the time derivative of the velocity potential
is not zero, and it has to be included when solving for the pressure by use of
Bernoulli´s theorem.

Unsteady flow is characterized by a mean part and an unsteady part,
where the unsteady part is due to turbulence. Turbulence can be split into a
range of wave numbers by Fourier analysis. This means that the turbulence
can be decomposed into a range of sinusoidal waves.

2.1.1   Steady Flow

Steady flow is treated in many textbooks and this Section is based on the treatment by Batchelor (1967).

The flow around wind turbine aerofoils can be treated as incompressible because the ratio of the speed of the flow and the speed of sound in air ($c_0 \simeq 340\frac{m}{s}$) is low and this ratio is the Mach number, $M \equiv \frac{u}{c_0}$ (below ~ 0.25, because the tip speed of a wind turbine blade is $u \simeq 80 \frac{m}{s}$ and the relative speed decreases from tip to the center of the rotor). The flow in an incompressible, irrotational, and inviscid fluid can be described by a velocity potential. Furthermore, the condition of no flow through the aerofoil is applied. The velocity potential for a section of an infinite cylinder with circulation is

$$O(z_c) = (U - jW)z_c + (U + jW)\frac{r2}{z_c} + \frac{j\kappa_c}{2\pi}\log\frac{z_c}{r}, \qquad (2.1)$$

where $z_c = x + jz$ is the position in complex notation and j denotes the imaginary unit, U the x-component of the far field flow, W the z-component, r the radius of the cylinder, and κ the circulation around the cylinder. The lines, where the imaginary part of the complex potential, $O(z_c)$, is constant $(\text{Im}(O(z_{c,1})) = \text{Im}(O(z_{c,2})) = constant)$, are streamlines and the flow is parallel with these streamlines. The flow around a subset of aerofoils can be found by a coordinate transformation defining the so-called the Joukowski aerofoils. They are created by the complex transformation

$$\zeta = z_c + \frac{\lambda^2}{z_c} \qquad \lambda = x_0 + \sqrt{r^2 - z_0{}^2}, \qquad (2.2)$$

which transforms a circle in a complex plane (z_c-plane) into the shape of the profile of an aerofoil in another complex plane (ζ-plane). The shape of the profile is dependent of the choice of the centre of the circle (x_0, z_0), an example is shown in Figure 2.1. The transformation will be a flat plate if (x_0, z_0) is placed in the origin of the coordinate system, (0,0). The Joukowski airfoil will be symmetric around the x-axis if z_0 is zero, and the aerofoil will have a camber line if z_0 is different from zero. The camber line will bend downwards when $z_0 > 0$. The streamlines for a circular cylinder are stretched like a rubber sheet so they fit around the Joukowski profile. In other words, the velocity potential at a given position (x, z) in the plane of the circle has the exact same value at the new position according to the transformation given by Eqn. (2.2) of (x, z). Figure 2.2 shows the streamlines in the plane of the circular cylinder and in the plane of the aerofoil, and it shows a transformation of the streamlines by Eqn. (2.2). The flow is parallel
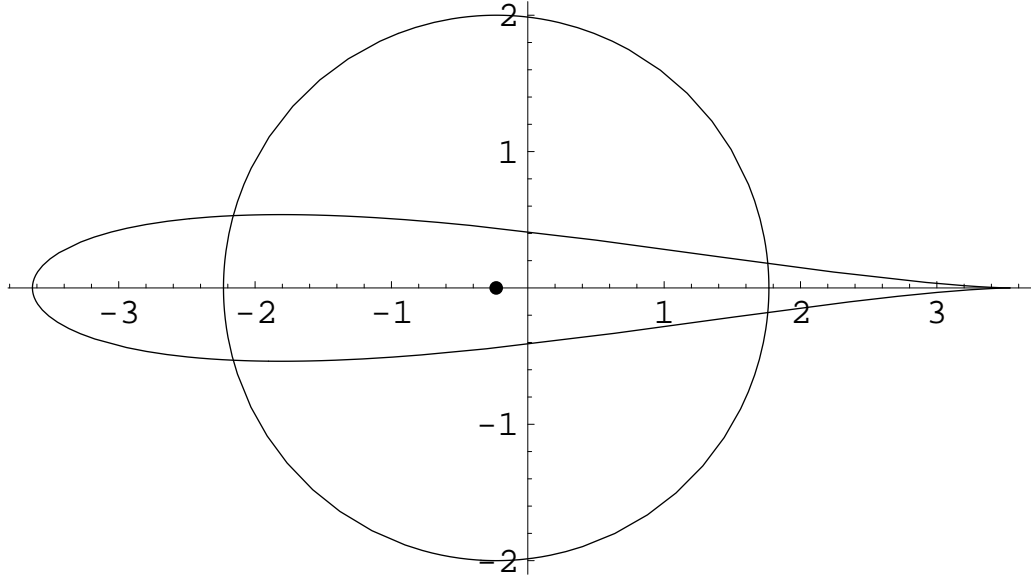
Figure 2.1: The Joukowski aerofoil for (x_0, z_0)=(-0.23173,0), which gives a value of λ from Eqn. (2.2) using $r = 2$ of 1.76827. The circle shown (z_c-plane) is transformed (ζ-plane) and the centre of the circle is shown by a big dot. The aerofoil (ζ-plane) meet the flow from the left, the curved edge.

to the aerofoil at the surface and has a non-zero value because the fluid is assumed inviscid and has a slip condition. Another necessary condition is that the flow at the trailing edge (the sharp edge of the aerofoil at the opposite side of the incoming flow) is finite, has a pressure difference of zero, and smooth outflow. This is called the Joukowski condition.

The velocities at the surface of the aerofoil in the circle plane (z_c-plane) are

$$U - jW = \left.\frac{dO}{dz_c}\right|_{z_c=circle} \tag{2.3}$$

and in the plane of the aerofoil (ζ-plane) the velocities at the surface are

$$U - jW = \frac{dO}{d\zeta} = \frac{dO}{dz_c}\left(\frac{d\zeta}{dz_c}\right)^{-1} \tag{2.4}$$

by use of the chain rule for differentiation. In order to satisfy the Joukowski condition on the trailing edge (finite flow at the trailing edge) then the circulation (κ_c in Eqn. (2.1)) is given by (Batchelor 1967)

$$\kappa_c = 4\pi\sqrt{U^2 + W^2}c\sin(\alpha_{AOA} + \beta_t), \tag{2.5}$$

where c the chord length of the aerofoil, α_{AOA} the angle to the horizontal of the inflow in the far field, and β_t the angle to the horizontal of the trailing

(a) Circle plane (z_c-plane)

(b) Aerofoil plane (ζ-plane)
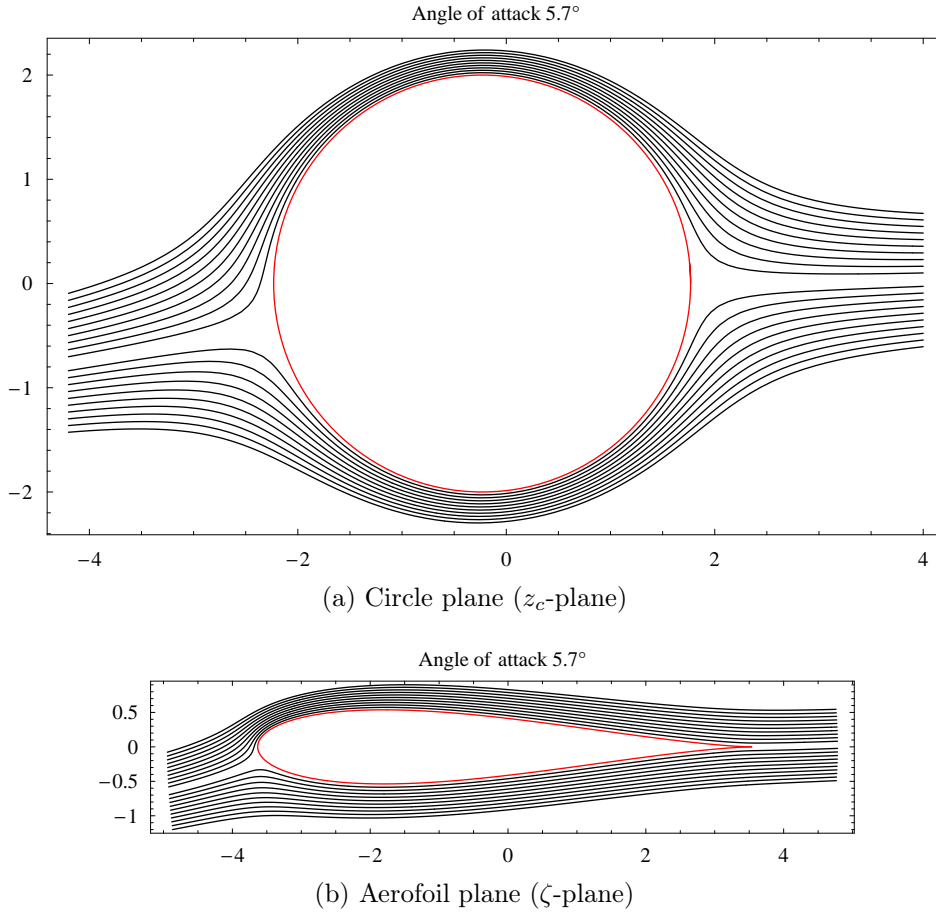
Figure 2.2: The streamlines in the plane of the circle (z_c-plane) and in the plane of the Joukowski aerofoil (ζ-plane). The parameters x_0, z_0, and λ are the same as for Figure 2.1. The AOA is 5.7°.

edge of the aerofoil in the ζ-plane. The velocities at the surface of the airfoil shown in Figure 2.1 and Figure 2.2 are plotted in Figure 2.3, and it reveals why the resulting force is upward according to Bernoulli's theorem described below in Eqn. (2.11).

Bernoulli´s theorem can be derived from the inviscid equation of motion

$$\frac{D\mathbf{u}}{Dt} = \mathbf{g} - \frac{1}{\rho}\nabla p \Leftrightarrow \frac{\partial \mathbf{u}}{\partial t} + \mathbf{u} \cdot \nabla \mathbf{u} = \mathbf{g} - \frac{1}{\rho}\nabla p. \tag{2.6}$$

In Eqn. (2.6) $\mathbf{g}$ is the acceleration due to gravity. When the assumption of
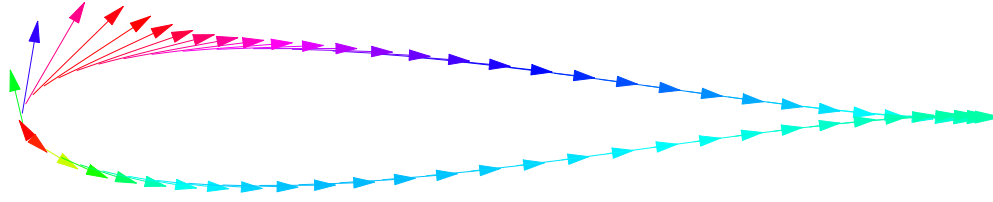
Figure 2.3: The velocity vector at the surface of the Joukowski aerofoil with parameters as the aerofoil in Figure 2.1 and Figure 2.2 and an angle of the inflow relative to the horizontal of $5.71°$. It is noted that the resulting force has it highest contribution at the upper side of the leading edge according to Bernoulli´s theorem described by Eqn. (2.11). This is because the length of the velocity vectors are largest above the aerofoil than below. Red colours indicate long vectors (upper leading edge) relative to green colours (lower leading edge), and blue colours are in between in length.

incompressible and irrotational flow is used

$$\mathbf{u} \quad = \quad \nabla\phi_v, \text{ (Implied by incompressibility)} \tag{2.7}$$

$$\omega \quad = \quad \nabla \times \mathbf{u} = 0, \text{ (Irrotational)} \tag{2.8}$$

$$\frac{1}{2}\nabla(\mathbf{u} \cdot \mathbf{u}) \quad = \quad \mathbf{u} \cdot \nabla\mathbf{u} + \mathbf{u} \times \omega, \text{ (Vector identity)} \tag{2.9}$$

the equation of motion becomes

$$\frac{\partial}{\partial t}\left(\nabla\phi_v\right) + \frac{1}{2}\nabla(\mathbf{u} \cdot \mathbf{u}) = \mathbf{g} - \frac{1}{\rho}\nabla p \Leftrightarrow \nabla\left(\frac{\partial\phi_v}{\partial t} + \frac{1}{2}\mathbf{u} \cdot \mathbf{u} + \frac{p}{\rho} - \mathbf{g} \cdot \mathbf{x}\right) = 0, \tag{2.10}$$

from which it can be concluded that the sum in the brackets has to be a constant

$$\frac{\partial\phi_v}{\partial t} + \frac{1}{2}|\mathbf{u}|^2 + \frac{p}{\rho} - g_z z = constant \tag{2.11}$$

where g_z is the vertical value of $\mathbf{g}$ and $g_z z$ is taken as a constant and therefore can be moved to the right side of Eqn. (2.11), and the equation becomes Bernoulli's theorem.

Bernoulli´s theorem Eqn. (2.11) can be shown to be valid in two cases: The case when the vorticity is zero and the case along a streamline for flow with vorticity as long as the flow is inviscid, Batchelor (1967), Section 7.1 and Section 7.4. The latter case is used for unsteady aerodynamics.

The magnitude of the resulting force due to the flow on the aerofoil is the lift, L, and is given by

$$L = \rho\sqrt{U^2 + W^2}\kappa_c. \tag{2.12}$$

This equation can also be found by integration of the pressure or velocity at the surface of the aerofoil at a cross section. This can be written as

$$\mathbf{L} = T_F - jN = -\oint p(dy + jdx) = -j\oint pd\bar{\zeta} = \frac{1}{2}j\rho\oint \left(\frac{dO}{d\zeta}\right)^2 d\zeta, \quad (2.13)$$

where the line integral is along the surface of the aerofoil, p the pressure at the surface, and $\overline{(\quad)}$ the complex conjugate. In the last equality in Eqn. (2.13) Bernoulli´s theorem in Eqn. (2.11) is used to relate the pressure to the velocity. The force is decomposed into a horizontal force which is tangential to the flow, T_F, and a vertical force which normal to the flow, N.

Eqn. (2.11) together with Eqn. (2.12) gives the information, that a high pressure difference across the aerofoil gives a large lift, e.g. low pressure (high velocity) at the upper side of the aerofoil and high pressure (low velocity) at the lower side of the aerofoil.

When the problem is to find the sound pressure level produced by the force from an aerodynamical source the distribution of the pressure fluctuations or the fluctuations of the pressure difference between the upper side and the lower side of an aerofoil is important to know. It is usually a simpler task to find the lift, because this is an integral of the pressure distribution and some terms thereby integrate to zero. The aerodynamical input to Amiet (1975) is pressure fluctuations on the aerofoil. The most important factor is lift fluctuations.

2.1.2 1-D Unsteady Aerodynamics

The theory for the unsteady pressure and lift fluctuations due to an 1-D gust is derived in detail in this Subsection. The theory is derived from Fung (1969). The theory is derived step by step in this thesis because the details are not shown in Fung (1969).

The simplest case of turbulence is when the unsteady part of the inflow only have a component in one direction, and in particular the upward direction. This means that fluctuations, w, are only in the vertical component of the wind. Further the variation of w is in the direction of the mean flow, U, see Figure 2.5. This motivates that this case of unsteady aerodynamics is called one-dimensional. The derivation of this case uses potential theory, and when the fluctuating part of the lift is calculated, the theory leads to Sears' solution (Sears 1941).

The calculation of unsteady aerodynamics on a flat plate with a gust which is varying in the flow direction only, can be done by use of potential theory as in the steady state case. The pressure fluctuations can be described

by potential theory by introducing an acceleration potential as

$$\phi = -\rho p \tag{2.14}$$

where ρ is taken as a constant because the flow is assumed incompressible and has no net circulation, ϕ is the real part of the complex acceleration potential, and p is the pressure fluctuation. The gust is subject of deformation caused by the presence of the aerofoil and has vertical movements which cause an acceleration normal to the aerofoil. The complex acceleration potential close to an infinite cylinder is for unsteady flow in the subsonic case from thin-aerofoil theory (Fung 1969) given as

$$o(z_c) = \phi + j\psi = \frac{jA_0}{z_c + 1} + \sum_{m=1}^{\infty} \frac{A_m}{z_c^m}, \ |z_c| \geq 1 \tag{2.15}$$

where j is the imaginary unit. Below the imaginary unit $\imath$ will be introduced. It is important to distinguish between j and $\imath$, because $j \neq \imath$. The imaginary unit j is in the spatial complex plane, whereas $\imath$ is in the time domain, i.e. it relates to a phase. The real part of the complex potential is the acceleration potential (ϕ) and the imaginary part is the stream function (ψ). The coordinates of the surface of the cylinder is $z_c = e^{j\theta}$ which have the property $|z_c| = 1$. The acceleration of the fluid close to the aerofoil is given as

$$a_i = \frac{\partial \phi}{\partial x_i}. \tag{2.16}$$

When inserting the coordinates of the cross section of the cylinder, z_c, into Eqn. (2.15) we get

$$\phi_0 = \frac{A_0 \sin \theta_1}{r_1} \qquad \psi_0 = \frac{A_0 \cos \theta_1}{r_1} \tag{2.17}$$

$$\phi_m = \frac{A_m \sin m\theta}{r^m} \qquad \psi_m = \frac{A_m \cos m\theta}{r^m} \tag{2.18}$$

$$\phi = \phi_0 + \sum_{m=1}^{\infty} \phi_m \qquad \psi = \psi_0 + \sum_{m=1}^{\infty} \psi_m \tag{2.19}$$

where the coordinates are visualized in Figure 2.4. The aerofoil is given by the Joukowski transformation described previously in Eqn. (2.2). In order to have the leading edge at $x = -1$ and the trailing edge at $x = 1$ at a flat plate, the transformation is

$$\zeta = \frac{1}{2} \left(z_c + \frac{1}{z_c} \right) \tag{2.20}$$

where the coordinates of the plate are given by transforming $z_c = e^{j\theta}$. When the circle described by $z_c = e^{j\theta}$ is transformed to the ζ-plane by Eqn. (2.20) it becomes the flat plate depicted in Figure 2.4. The vertical acceleration of the fluid, a_y, at the aerofoil in the ζ-plane is related to the normal acceleration, a_n, at the circle in the z_c-plane. The acceleration normal to the cylinder, a_n, will be normal to the plate, a_y, when the cylinder is stretched like a rubber sheet into a flat plate. It is only the vertical acceleration of the gust (the normal acceleration to the cylinder) that is of interest because the change in vertical velocity of the gust due to the aerofoil is to be found. The acceleration in complex notation is given as

$$\frac{do}{d\zeta} = \frac{do}{dz_c} \left(\frac{d\zeta}{dz_c} \right)^{-1} \tag{2.21}$$

and thus the magnitude of scaling of the acceleration from the ζ-plane to the z_c-plane becomes

$$\left| \frac{d\zeta}{dz_c} \right| = \frac{1}{2} \left| \frac{1}{z_c} \left(z_c - \frac{1}{z_c} \right) \right| = |\sin \theta| . \tag{2.22}$$

Then the acceleration normal to the cylinder has the relation to the acceleration vertical to the aerofoil

$$a_n(\theta, t) = a_y(x, t) \sin \theta. \tag{2.23}$$

The acceleration in the normal direction to the cylinder in the z_c-plane is then given from Eqn. (2.16)

$$a_n = \left. \frac{\partial \phi}{\partial r} \right|_{r=1} = 0 + \sum_{m=1}^{\infty} -m A_m \sin m\theta \tag{2.24}$$

The first term in Eqn. (2.24) is zero because

$$\left. \frac{\partial \phi_0}{\partial r} \right|_{r=1} = \frac{-1}{r \sin \theta} \left. \frac{\partial \psi_0}{\partial \theta} \right|_{r=1} = \frac{-1}{r \sin \theta} \frac{\partial}{\partial \theta} \frac{A_0}{2} \Big|_{r=1} = 0 \tag{2.25}$$

according to Figure 2.4. The velocity fluctuations an aerofoil feels due to a 1-D sinusoidal gust can be described as

$$v_{1D}(x, t) = -w \exp \iota \omega (t - x/U) = -w \exp(\iota \omega t) \exp(-\iota \kappa \cos \theta) \tag{2.26}$$

under the assumption of Taylor's hypothesis of frozen turbulence, which in fact follows from the linear assumption, where the wave number is $k_x = \frac{\omega}{U}$,
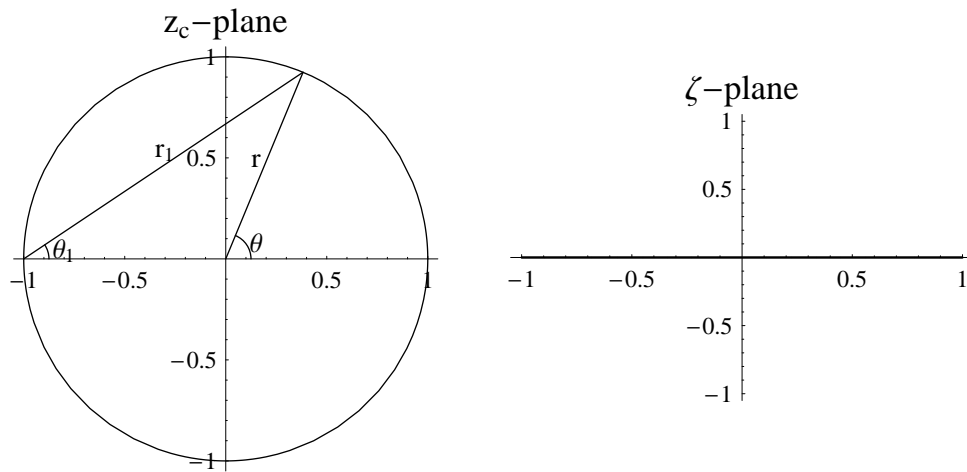
Figure 2.4: A circle in the z_c-plane is transformed by Eqn. (2.20) into an aerofoil (flat plate) in the ζ-plane. The circle has origin at $\{0,0\}$ and is described by $re^{i\theta}$. Under the angle θ_1 with origin at $\{-1,0\}$ the distance r_1 to the circle is $2r\cos\theta_1$, further it is quite easily seen that $\theta_1 = \frac{\theta}{2}$.
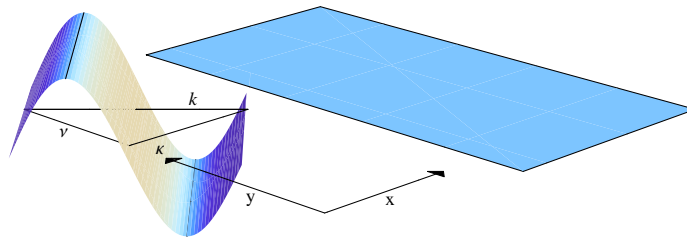
Figure 2.5: Sketch of a skewed sinusoidal gust entering a flat plate. The width in the x-direction is the chord length, c.

the reduced wave number is $\kappa = \frac{k_x c}{2}$, and $x = \frac{c}{2}\cos\theta$. The chord length, c, is in the following set to 2 for convenience. The $\imath$ describes the oscillation in the time domain and thus $\imath j \neq -1$. The gust is visualized in Figure 2.5. Eqn. (2.26) can be expanded as

$$v_{1D}(\theta, t) = -we^{\imath\omega t}\left(J_0(\kappa) + 2\sum_{m=1}^{\infty}(-\imath)^m J_m(\kappa)\cos m\theta\right) \quad (2.27)$$

$$= -we^{\imath\omega t}\left(P_0(\kappa) + 2\sum_{m=1}^{\infty}P_m(\kappa)\cos m\theta\right), \quad (2.28)$$

$$P_m(\kappa) = (-\imath)^m J_m(\kappa) \quad (2.29)$$

with use of Eqns. (A.52) and (A.7), where $J_m(\kappa)$ is the Bessel function of first kind of order m, see also Appendix A. Below $P_m(\kappa)$ is denoted P_m for convenience. The upward acceleration at the aerofoil in the ζ-plane is found by

$$a_y = \frac{Dv_{1D}}{Dt} = \frac{\partial v_{1D}}{\partial t} - U\frac{1}{r\sin\theta}\frac{\partial v_{1D}}{\partial\theta} \quad (2.30)$$

$$= i\omega v_{1D}(\theta, t) - 2Uwe^{\imath\omega t}\sum_{m=1}^{\infty}mP_m\frac{\sin m\theta}{\sin\theta}. \quad (2.31)$$

This becomes in the z_c-plane with use of Eqns. (A.53) and (2.23)

$$a_n(\theta, t) = -wUe^{\imath\omega t}\left(\imath\kappa\left[P_0\sin\theta + \sum_{m=1}^{\infty}P_m(\sin(m+1)\theta - \sin(m-1)\theta)\right]\right.$$

$$\left. +2\sum_{m=1}^{\infty}mP_m\sin m\theta\right) \quad (2.32)$$

$$= -2Uwe^{\imath\omega t}\sum_{m=1}^{\infty}\sin m\theta\left(\frac{\imath\kappa}{2}P_{m-1} + mP_m - \frac{\imath\kappa}{2}P_{m+1}\right). \quad (2.33)$$

When this is equated to Eqn. (2.24) then the coefficients

$$A_m = 2Uwe^{\imath\omega t}\left(\frac{\imath\kappa}{2m}P_{m-1} + P_m - \frac{\imath\kappa}{2m}P_{m+1}\right), \quad m \geq 1 \quad (2.34)$$

are found. To find A_0 the boundary condition of the velocity at the leading edge is a natural choice. The vertical velocity can be found by integration of the vertical acceleration given in Eqn. (2.30) by using the condition that the velocity is zero far upstream ($x = -\infty$), and then the velocity in the aerofoil

plane can be written as (Fung 1969)

$$v_{1D}(x) = \frac{e^{-\iota\kappa x}}{U} \int_{-\infty}^{x} a_y(x')e^{\iota\kappa x'}dx' = -\frac{e^{-\iota\kappa x}}{U} \int_{-\infty}^{x} \left(\sum_{m=0}^{\infty} \frac{\partial\psi_m}{\partial x'}\right) e^{\iota\kappa x'}dx'$$
(2.35)

where the stream function, ψ_m, in the aerofoil plane from Eqns. (2.17) and (2.18) and inversion of Eqn. (2.20) is

$$\psi_0(x) = \frac{-A_0}{-x-1+\sqrt{x^2-1}} = \frac{A_0}{2}\left(1 + \frac{x-1}{\sqrt{x^2-1}}\right)$$
(2.36)

$$\psi_m(x) = \frac{(-1)^m A_m}{\left(-x+\sqrt{x^2-1}\right)^m} = A_m\left(x+\sqrt{x^2-1}\right)^m,$$
(2.37)

$$x \in]-\infty, -1[,\ m \geq 1.$$

The stream function in Eqn. (2.19) is hereby defined upstream of the aerofoil and at $y = 0$ which corresponds to $\theta = \pi$ in the coordinates of the cylinder in the z_c-plane. At the leading edge Eqn. (2.35) is

$$v_{1D}(\pi, t) = -e^{\iota\kappa}\left[e^{\iota\kappa x}\frac{\psi_0(x)}{U}\right]_{-\infty}^{-1} + \frac{e^{\iota\kappa}}{U}\int_{-\infty}^{-1}\left(\iota\kappa\psi_0 - \sum_{m=1}^{\infty}\frac{\partial\psi_m}{\partial x}\right)e^{\iota\kappa x}dx$$
(2.38)

where partial integration of ψ_0 is necessary because of its singularity at the leading edge. The left hand side in Eqn. (2.38) is with use of Eqn. (2.28) written as

$$v_{1D}(\pi, t) = -we^{\iota\omega t}(P_0 + 2\sum_{m=1}^{\infty}(-1)^m P_m).$$
(2.39)

Because $\psi_0 = \frac{A_0}{2}$ by use of Eqn. (2.17) on the aerofoil and ψ_0 vanishes far upstream of the aerofoil by Eqn. (2.36) then

$$-e^{\iota\kappa}\left[e^{\iota\kappa x}\frac{\psi_0(x)}{U}\right]_{-\infty}^{-1} + \frac{e^{\iota\kappa}}{U}\int_{-\infty}^{-1}\iota\kappa\psi_0 e^{\iota\kappa x}dx = -\frac{A_0}{2U}\iota\kappa e^{\iota\kappa}\left[K_0(\iota\kappa) + K_1(\iota\kappa)\right]$$
(2.40)

where Eqns. (2.36), (A.37), and (A.46) is recalled. The remaining terms in Eqn. (2.38) are

$$-\frac{e^{\iota\kappa}}{U}\int_{-\infty}^{-1}\sum_{m=1}^{\infty}\frac{\partial\psi_m}{\partial x}e^{\iota\kappa x}dx = -we^{\iota\omega t}\left[\left(P_0 + 2\sum_{m=1}^{\infty}(-1)^m P_m\right)\right.$$

$$\left. -2\frac{\iota\kappa}{2}e^{\iota\kappa}P_0 K_1(\iota\kappa) + 2\frac{\iota\kappa}{2}e^{\iota\kappa}P_1 K_0(\iota\kappa)\right]$$
(2.41)
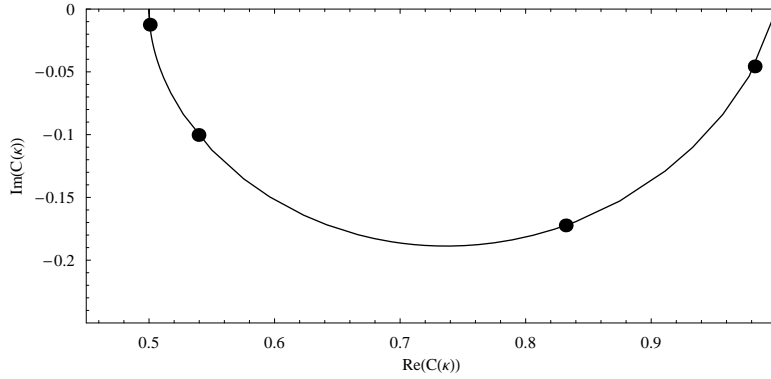
Figure 2.6: The behavior of the Theodorsen function, $C(\kappa)$. The Theodorsen function is a complex function, and thus it is plotted in the complex plane. The range of the argument, κ, in the plot is from 0 to ∞, where $\kappa = 0$ is on the real axis at 1, and $\kappa \to \infty$ is on the real axis at 0.5. The dots are from right to left on the line for $\kappa = \{0.01, 0.1, 1, 10\}$, respectively.

where the details are given in Eqn. (B.4). Inserting Eqns. (2.40), (2.41) and (2.39) into Eqn. (2.38) then finally A_0 is found as

$$A_0 = 2Uwe^{\imath\omega t}\left[C(\kappa)(P_0 + P_1) - P_1\right], \; C(\kappa) = \frac{K_1(\imath\kappa)}{K_0(\imath\kappa) + K_1(\imath\kappa)}. \qquad (2.42)$$

The function $C(\kappa)$ is called the Theodorsen function and is illustrated in Figure 2.6. The Theodorsen function is the solution for vertical translation oscillations of a flat plate, Theodorsen and Garrick (1942) and Fung (1969).

The acceleration potential in the z_c-plane is then easily found from Eqn. (2.19)

$$\phi(\theta, t) = \frac{A_0}{2}\tan\frac{\theta}{2} + \sum_{m=1}^{\infty} A_m \sin m\theta. \qquad (2.43)$$

The pressure difference over the aerofoil is $l(x) = -2p(x)$ according to thin aerofoil theory applied to a flat plate (Fung 1969). The lift distribution, the pressure difference across the plate, is according to Eqn. (2.14) equal to

$$l(x, t) = 2\rho\phi(x, t). \qquad (2.44)$$

When Eqn. (2.43) is inserted in Eqn. (2.44) then

$$l(\theta, \kappa, t) = \rho A_0 \tan\frac{\theta}{2} + 2\rho \sum_{m=1}^{\infty} A_m \sin m\theta \qquad (2.45)$$
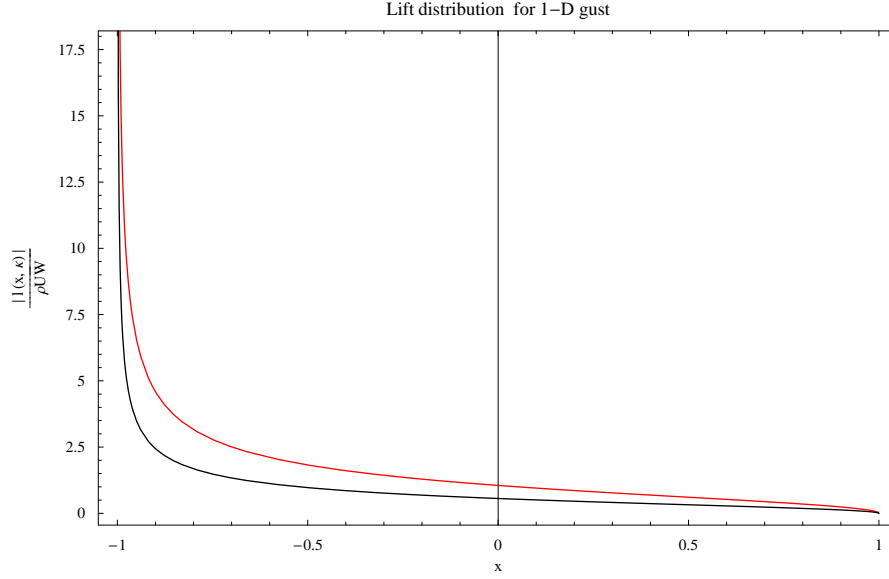
Figure 2.7: The lift magnitude of distribution normalized with $\rho U w e^{\iota \omega t}$ as function of the chordwise position, x, where $x = -1$ is the leading edge and $x = 1$ is trailing edge. The red line is for $\kappa = 0.5$, and the black line is for $\kappa = 2$.

where A_0 and A_m and thus also P_m are defined in Eqns. (2.42), (2.34), and (2.29), respectively.

The magnitude of the lift distribution is seen to decrease from the leading edge towards the trailing edge, see Figure 2.7. Furthermore the higher the wave number is the less the fluctuation is.

The lift fluctuation is the integrated pressure difference fluctuation

$$L' = \int_{-1}^{1} l(x) dx \qquad (2.46)$$

where the integration is in the ζ-plane and

$$L' = \int_{0}^{\pi} l(\theta) \sin \theta d\theta \qquad (2.47)$$

in the z_c-plane. When Eqn. (2.45) is inserted in Eqn. (2.47) then

$$L' = \rho U w e^{\iota \omega t} 2\pi \left[(P_0 + P_1)C(k) + (P_0 - P_2)\frac{\iota \kappa}{2} \right] \qquad (2.48)$$

because only terms including A_0 and A_1 contribute to the lift. When the relations Eqns. (2.29) and (A.6) are used and Eqn. (2.48) is generalized to

any chord length, c, of the aerofoil, then

$$L'(\kappa) = \frac{1}{2}\rho c U w e^{\imath\omega t} 2\pi \left[(J_0(\kappa) - \imath J_1(\kappa))C(\kappa) + \imath J_1(\kappa) \right] \qquad (2.49)$$

is obtained. It is recalled that $\kappa = \frac{k_x c}{2}$ and $c = 2$ in the above derivations. The term in square brackets is Sears function

$$S(\kappa) = 2\pi[(J_0(\kappa) - \imath J_1(\kappa))C(\kappa) + \imath J_1(\kappa)]. \qquad (2.50)$$

Its behavior is seen in Figure 2.8, where it is seen that no frequency cause instability. The steady state reduced wave number $\kappa = 0$ is at the real axis at 2π. The reduced wave number is increased along the black line in Figure 2.8 and ends at a reduced wave number of 10 (shown by a blue cross). The absolute value of the lift is decreasing as the wave number is increased. Dependent on the wave number the lift at the midpoint is either lagging or ahead of the gust signal at the midpoint, see Figure 2.8. The lift is lagging when $Im\{S(\kappa)\} < 0$, and ahead when $Im\{S(\kappa)\} > 0$.

The expressions for the fluctuating lift distribution and fluctuating lift can for convenience be split into a transfer function and an amplitude. When Eqn. (2.44) is split into an amplitude and a transfer function then

$$l(x, \kappa) = A(\rho, c, U)wg(x, \kappa) \qquad (2.51)$$

where the amplitude and transfer function are

$$A(\rho, c, U) = \frac{1}{2}\rho c U \qquad (2.52)$$

$$g(x, \kappa) = \frac{A_0}{Uw}\tan\left(\frac{\arccos x}{2}\right) + 2\sum_{m=1}^{\infty}\frac{A_m}{Uw}\sin(m\arccos x), \quad (2.53)$$

respectively, and w is the amplitude of the vertical gust. The coefficients A_0 and A_m are defined in Eqns. (2.42) and (2.34), respectively. Similarly Eqn. (2.49) gives

$$L'(\kappa) = A(\rho, c, U)wg(\kappa) \qquad (2.54)$$

where $A(\rho, c, U)$ is defined in Eqn. (2.52) and $g(\kappa)$ is defined in Eqn. (2.50).

2.1.3   2-D Unsteady Aerodynamics

A model is described below that will be referred to as the 2-D model. This model is for a section of an aerofoil like the one just described and is
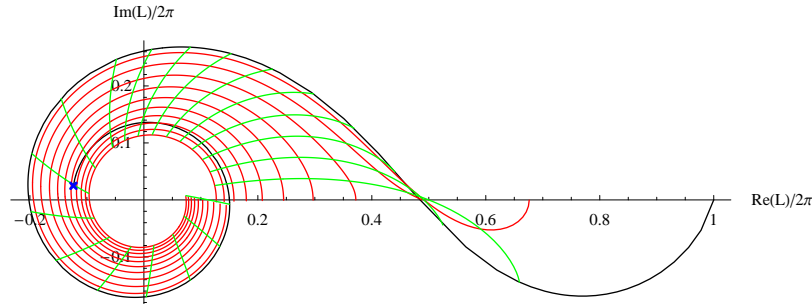
Figure 2.8: Plot of the lift response due a sinusoidal gust as function of reduced wave number. The black line is due to a 1-D sinusoidal gust on a flat aerofoil as discussed in section 2.1.2. Note that the absolute value of the lift response $|L|$ is the distance from the origin of the plot to a point on, say, the black line. The argument of L is the corresponding phase of the lift relative to the phase of the gust at the midpoint of the aerofoil to the gust. The green and red lines in the plot show the case of a 2-D sinusoidal gust on a 2-D flat aerofoil and are discussed in section 2.1.4. The red lines are functions of κ for different values of fixed ν, where ν is varied from 0 to 2.5 in steps of .25. The green lines are functions of ν when κ is fixed, and κ takes values from 0 to 2.5 in steps of 0.25 and from 3 to 7 in steps of 0.5.

with a 2-D sinusoidal gust impinging the aerofoil. The gust has an u- and a w- component which are in the x- and z-direction, respectively. Further the model is for a bend plate with an AOA to the mean flow.

The unsteady aerodynamics can be solved for a section of a profile with camber at an AOA to the mean flow, which means that there are mean lift as well as fluctuating lift. A 2-D gust causes fluctuating lift on this bend flat plate because the u- and w-components give an upwash, see Figure 2.9. The figure shows the problem to solve and show the definitions of the wave numbers to be explicitly defined below.

The 2-D model is based on Goldstein and Atassi (1976) and Atassi (1984). This model is in principle valid for a section of an aerofoil with camber and thickness at an AOA to the mean flow, Goldstein and Atassi (1976). Explicit solutions for the model are given in Atassi (1984) for a section with camber at an AOA to the mean flow. The model is linear so it is split up in a contribution due to the camber and a contribution due to AOA. The 2-D model is based on the inviscid and incompressible Navier-Stokes equations which are linearized.
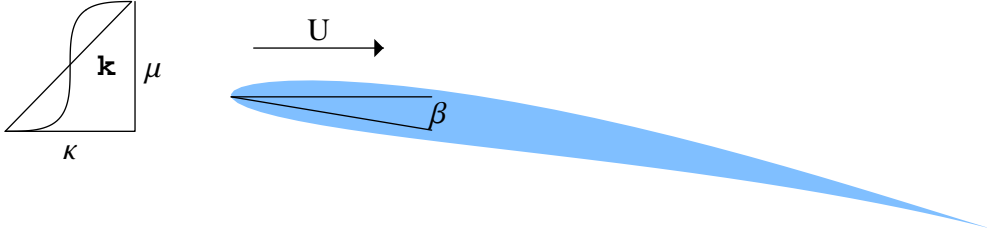
Figure 2.9: Sketch of a skewed sinusoidal gust entering an aerofoil with thickness and camber at an AOA to the mean flow.

This leads to the total response given as

$$R_T(\kappa, \mu) = \frac{\kappa}{\sqrt{\kappa^2 + \mu^2}} \frac{\overline{S(\kappa)}}{2\pi} + \beta_A L_{\beta_A}(\kappa, \mu) + m L_m(\kappa, \mu) \qquad (2.55)$$

where the response due to a flat plate is included, $L_{\beta_A}(\kappa, \mu)$ is the response due to AOA, and $L_m(\kappa, \mu)$ is the response due to camber. The parameters κ, μ, β_A, and m are defined below.

When the model is linearized for small AOA it can be found that the lift response due to the AOA in radians, β_A, Atassi (1984), is

$$
\begin{aligned}
L_{\beta_A}(\kappa, \mu) &= \frac{1}{|k_c|} \left\{ \kappa \left[-\frac{4\kappa\mu}{|k_c|^2} \frac{\overline{S(\kappa)}}{2\pi} + \Theta_+\left(\frac{k_c}{2}\right) - \overline{\Theta_-\left(\frac{k_c}{2}\right)} \right] \right. \\
&\quad \left. + \imath C(\kappa) \left[\Lambda_+\left(\frac{k_c}{2}\right) - \overline{\Lambda_-\left(\frac{k_c}{2}\right)} \right] \right\}
\end{aligned}
\qquad (2.56)
$$

where

$$\Lambda_\pm(z_v) \equiv \pm \imath \pi z_v^2 Im\left\{ H_\pm(z_v)\overline{J_\pm(z_v)} \right\} \qquad (2.57)$$

$$\Theta \pm (z_v) \equiv \pm \imath \frac{\pi z J_1(z_v) Im\left\{ H_\pm(z_v)\overline{J_\pm(z_v)} \right\} - \overline{J_\pm(z_v)}}{J_\pm(z_v)} \qquad (2.58)$$

$$J_\pm(z_v) \equiv J_0(z_v) \pm \imath J_1(z_v) \qquad (2.59)$$

$$H_\pm(z_v) \equiv H_0^{(1)}(z_v) \pm \imath H_1^{(1)}(z_v) \qquad (2.60)$$

$$k_c \equiv \kappa + \imath\mu, \ \kappa = \frac{k_x c}{2}, \ \mu = \frac{k_z c}{2} \qquad (2.61)$$

where as previously c is the chord length. The Bessel functions, $J_0(z_v)$, $J_1(z_v)$, $J_2(z_v)$ (below), $H_0^{(1)}(z_v)$, and $H_1^{(1)}(z_v)$ are defined in Appendix A. Further

$\overline{S(\kappa)}$ is the complex conjugated of Eqn. (2.50) and $C(\kappa)$ is defined in Eqn. (2.42).

Figure 2.10a) and b) show Eqn. (2.56). It is seen that at low μ the response approaches zero as κ is increased and the larger μ gets the slower it converges to zero. The absolute value of the response approaches to an asymptotic value for values of μ large enough, see blue line in Figure 2.10b).

The camber is approximated to a parabolic line which describes the camber line best, Atassi (1984), and implies that the parameter, m, is describing the bending of the parabolic line. When the lift response is linearized in the camber it can be found that the lift response due to camber, Atassi (1984), is

$$
L_m(\kappa, \mu) = \frac{4}{|k_c|} \left\{ -i \frac{8\kappa\mu(\kappa^2 - \mu^2)}{|k_c|^4} \frac{\overline{S(\kappa)}}{2\pi} + \frac{4\kappa\mu}{|k_c|^2} \left[\pi\kappa G_A \left(\frac{k_c}{2} \right) - E_A(\kappa) \right] \right.
$$
$$
\left. + C(\kappa) \left[F_+ \left(\frac{k_c}{2} \right) - \overline{F_- \left(\frac{k_c}{2} \right)} \right] \right\} \tag{2.62}
$$

where

$$
E_A(\kappa) \equiv \kappa J_2(\kappa) + C(\kappa) \left[\kappa J_+(\kappa) - J_1(\kappa) \right] \tag{2.63}
$$
$$
G_A(z_v) \equiv Im \left\{ \overline{H_1^{(1)}(z_v)} J_1(z_v) \right\} \tag{2.64}
$$
$$
F_\pm(z_v) \equiv \frac{z_v}{\bar{z}_v} \frac{\pi z J_\pm(z_v) G_A(z_v) - \overline{J_1(z_v)}}{J_1(z_v)}. \tag{2.65}
$$

Figure 2.10c) and d) show the response due to camber according to Eqn. (2.62). Similar to the response function of the AOA the response function for camber is approaching zero as κ is increased until a certain μ where an asymptotic value of the absolute value of the response is approached, see red and green line in Figure 2.10d).

The model is based on the convention that the time part is defined as $e^{-i\omega t}$ whereas it is defined as $e^{i\omega t}$ in the 1-D model above and in the 3-D model below. In order to compare with these models the complex conjugate of Eqn. (2.55) is taken throughout this thesis.

Figure 2.10e) and f) show the complex conjugate of the total response. The complex response and the absolute response is shown, and when the AOA is different from zero the total response is seen to approach an asymptotic value that is not going to zero as κ is increased. The response with camber and AOA=0° is seen to vanish as κ is increased.

When the total response function of the fluctuating lift is known the lift fluctuation is found as

$$
L'(\kappa, \mu) = A(\rho, c, U)(w + u)g(\kappa, \mu) \tag{2.66}
$$

where $A(\rho, c, U)$ is defined in Eqn. (2.52) and

$$g(\kappa, \mu) = 2\pi \overline{R_T(\kappa, \mu)} \tag{2.67}$$

in order to be compared with Eqn. (2.54).

The model described above is able to take some aerodynamically important parameters of an aerofoil into account. The parameters for which explicit expressions are given are camber and AOA to the mean flow. The thickness is also a part of the model, Goldstein and Atassi (1976), but no explicit expression is found for this parameter. This author has made an attempt to solve for the thickness but further work is needed in order for an explicit expression to be given.

2.1.4   3-D Unsteady Aerodynamics

The unsteady aerodynamics has been solved for a skewed gust on a semi-infinite flat plate, Graham (1970). This model is referred to as the 3-D model below. The model is called 3-D because a sinusoidal gust (where only the w-component is taken into account) can be skewed arbitrarily when it impinges the aerofoil which is infinite in spanwise direction. This means that the vertical gust can have any variation in the chord wise and spanwise directions, see Figure 2.5. The paper by Graham (1970) suggest a method of finding the lift distribution but an explicit expression is not given. The lift distribution is found in this Subsection and an explicit expression is given.

This model solves for the upwash for an sinusoidal wave of arbitrarily yawed angle to the leading edge of the aerofoil. The upwash can be described by potential theory by Poisson's equation and is given by, $v_{3D}(x_0, y_0)$,

$$\int_{S+W_w} \frac{\gamma_1(x - x_0) - \gamma_2(y - y_0)dxdy}{4\pi[(x - x_0)^2 + (y - y_0)^2]^{3/2}} + v_{3D}(x_0, y_0) = 0. \tag{2.68}$$

where γ_1 is the spanwise vorticity and γ_2 is the chord wise vorticity. The integration is over all space in the xy-plane in which vorticity due to the aerofoil is present, being over the surface and in the wake. The vertical gust is given by

$$v_{3D} = U_\infty e^{\iota(k_x x + k_y y - \omega t)} \tag{2.69}$$

where k_x and k_y are the chord wise and spanwise wave numbers, respectively, U_∞ is the mean velocity of the flow far upstream of the aerofoil, and $\omega = k_x U_\infty$. The upwash at the aerofoil is thus given as

$$w_0(x_0, y_0) = \int_{-\infty}^{\infty} \int_0^c \frac{\gamma_1(x - x_0) - \gamma_2(y - y_0)}{4\pi[(x - x_0)^2 + (y - y_0)^2]^{3/2}} dxdy \tag{2.70}$$

Response function due to an AOA to the mean flow.
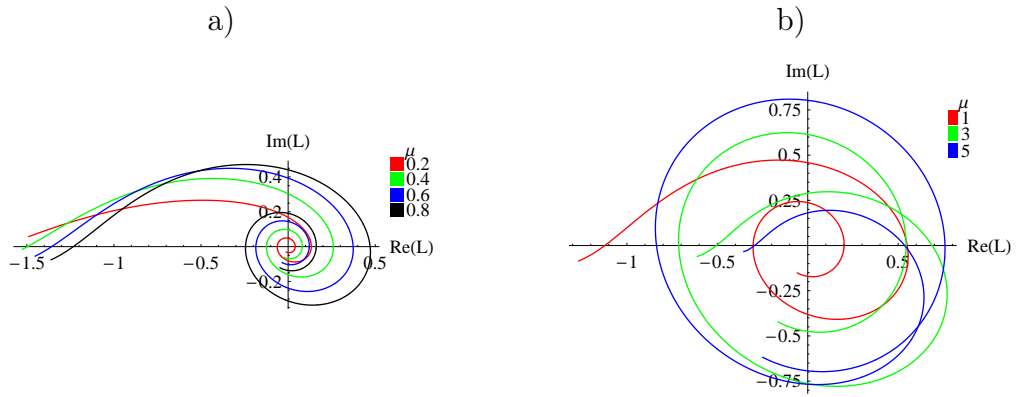
Response function due to camber.
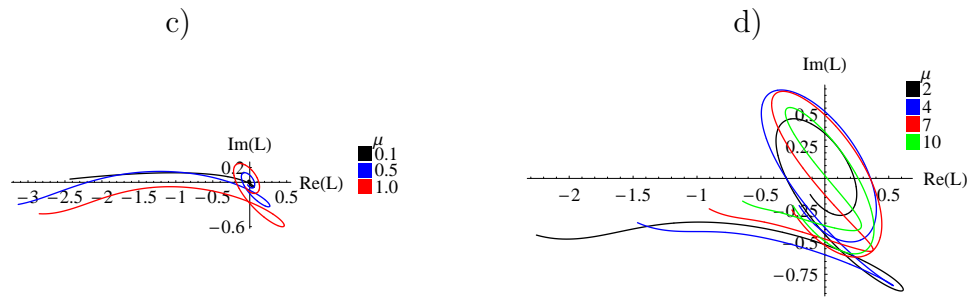
Total response function.
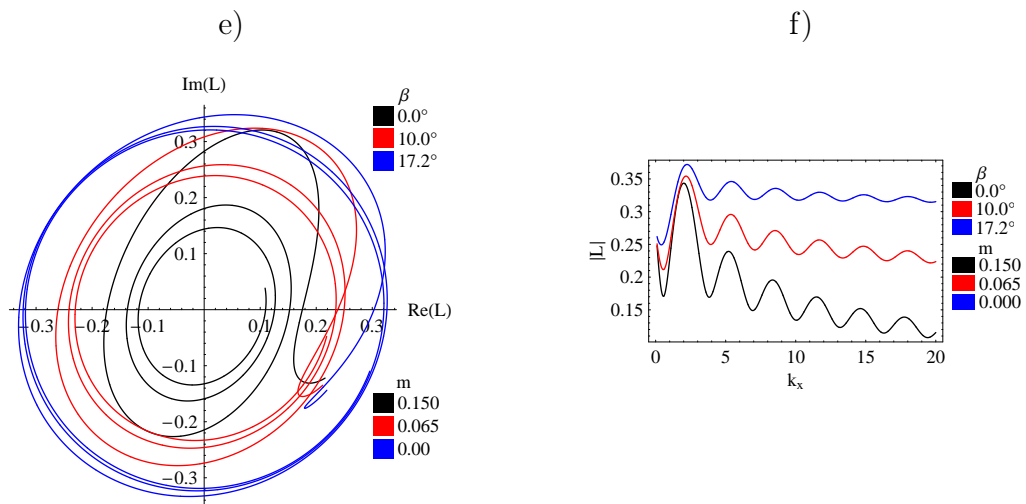
Figure 2.10: The transfer functions of the 2-D model. The figures a) to e) is similar to the plots in Atassi (1984). The lines are at fixed μ and κ is varied in a) to d). A 2-D gust for which the wave front has an angle of 45° to the mean flow and the wave length of this gust is varied in e) and f).

where x_0 and y_0 is any point on the aerofoil in the chord wise and spanwise direction, respectively, and c is the chord length as previously.

Continuity of the vorticity is assumed which leads to

$$\gamma_1 = 2U_\infty f_{01}(x)e^{\iota(k_y y - \omega t)} \tag{2.71}$$

$$\gamma_2 = -2\iota U_\infty k_y c f_{02}(x)e^{\iota(k_y y - \omega t)} \tag{2.72}$$

$$f_{02}(x) = \int_0^x f_{01}(x')\frac{dx'}{c} \tag{2.73}$$

where the functions $f_{01}(x)$ and $f_{02}(x)$ are to be found. When inserting Eqns. (2.71) and (2.72) into Eqn. (2.70) the upwash at the aerofoil can be evaluated to give

$$w_0(x_0, y_0) = \frac{U_\infty}{\pi}e^{\iota(k_y y_0 - \omega t)}\int_0^c \left\{ k_y f_{01}(x)\frac{(x - x_0)}{|x - x_0|}K_1(k_y|x - x_0|) \right.$$
$$\left. -k_y^2 c f_{02}(x)K_0(k_y|x - x_0|) \right\}dx \tag{2.74}$$

where $K_0(z_v)$ and $K_1(z_v)$ are modified Bessel functions of second kind as defined in Appendix A and z_v is real.

When a coordinate transformation is made and two new functions are defined then the upwash on the aerofoil can be given as

$$w_0(z_{n,0}, y_0) = \frac{U_\infty}{\pi}e^{\iota(k_y y_0 - \omega t)}\left\{ \int_{-1}^1 [\nu F(z_n)K_1'(\nu[z_n - z_{n,0}])]dz_n - 4\nu^2 f_3(1)K_0(\nu[z_n - z_{n,0}]) \right\} \tag{2.75}$$

where

$$z_n = \frac{2x}{c} - 1, \ z_{n,0} = \frac{2x_0}{c} - 1, \ x \in [0, c] \tag{2.76}$$

$$\nu = \frac{k_y c}{2}, \ \kappa = \frac{k_x c}{2}$$

$$f_{03}(x) = \int_0^x f_{02}(x')\frac{dx'}{c} \tag{2.77}$$

$$f_w(z_n) = f_{0w}(x)$$

$$F(z_n) = f_1(z_n) - 4\nu^2 f_3(z_n) \tag{2.78}$$

$$K_1'(z_n) = K_1(z_n), \ z_n > 0$$

$$K_1'(z_n) = -K_1(-z_n), \ z_n < 0$$

$$K_1'(0) = \pm\infty$$

is defined. The wave numbers ν and κ are reduced wave numbers in the sense that $\nu = \frac{k_y c}{2}$ and $\kappa = \frac{k_x c}{2}$.

Similarly the upwash can be found in the wake (Graham 1970) to be

$$
\begin{aligned}
w_1(z_{n,0}, y_0) \;=\; & \frac{U_\infty}{\pi} e^{i(k_y y_0 - \omega t)} i k_x c f_2(1) \Bigg[(1 + \nu^2/\kappa^2) \\
& \times \left\{ \int_{-1}^{\infty} \nu e^{i\kappa} (1 + z_n) K_1'(\nu[2 + z_n - z_{n,0}]) dz_n \right\} \\
& -\nu^2/\kappa^2 K_0(\nu[1 - z_{n,0}]) \Bigg]
\end{aligned}
\tag{2.79}
$$

The Eqns. (2.75) and (2.79) has to be equal

$$
w_0(z_{n,0}, y_0) = w_1(z_{n,0}, y_0). \tag{2.80}
$$

and the function, $F(z_n)$, in Eqn. (2.78) can be defined as

$$
F(z_n) = \frac{2}{\pi\sqrt{1 - z_n^2}} \sum_{k=0}^{N}{}'' \sigma_k T_k(z_n) \tag{2.81}
$$

where $T_k(z_n)$ is the Chebyshev polynomial of kth order, and σ_k is the kth coefficient, which is necessary to solve Eqn. (2.68). The Chebyshev polynomial is useful for approximating functions that are defined in the interval $-1 \le z_n \le 1$. The double prime in the sum of Eqn. (2.78) denotes that σ_0 and σ_N has to be multiplied with $\frac{1}{2}$, and σ_k has to be multiplied by 1 for $1 \le k < N$. A coordinate transform of the aerofoil has been conducted such that the leading edge is at $z_n = -1$ and the trailing edge is at $z_n = 1$, see Eqn. (2.76). The coefficients σ_k is found by solving a linear system of order k.

Eqn. (2.74) can be solved by expanding the terms in Eqn. (2.80) in Chebychev series which have the property that they converge fast. Then Eqn. (2.80) becomes linear system of n equations where n is the number of Chebychev coefficients used to expand the function in Eqn. (2.80). The transfer function of the lift is then found to be

$$
\overline{g(\kappa, \nu)} = 4[f_2(1) - i k_x c f_3(1)] \tag{2.82}
$$

with a phase at the leading edge relative to the gust at the leading edge. In order to get the transfer function of the lift with the phase at mid chord to the gust at mid chord relative like the 1-D model described in Section 2.1.2 then the transfer function, Graham (1970) is

$$
g(\kappa, \nu) = 4 e^{i\kappa} [\overline{f_2(1)} + i k_x c \overline{f_3(1)}] \tag{2.83}
$$

The transfer function is seen in Figure 2.8. It reduces to Eqn. (2.50) when $\nu = 0$, and when the spanwise wave number is different from zero the lift fluctuations approaches zero faster when κ is increasing. Likewise the lift fluctuations is seen to approach zero when κ is fixed and ν goes towards infinity. The complex lift indicates a lag in the response of the lift at mid chord in comparison to the inflow at mid chord.

The lift fluctuation is in the notation of Eqns. (2.54) and (2.66) given as

$$L'(\kappa, \nu) = A(\rho, c, U)wg(\kappa, \nu) \tag{2.84}$$

where $A(\rho, c, U)$ is defined in Eqn. (2.52) and $g(\kappa, \nu)$ is defined in Eqn. (2.83).

When Eqn. (2.68) is solved the pressure distribution is (Graham 1970)

$$\Delta p(z_n) = \frac{1}{2}\rho c U_\infty w_0(f_1(z_n) - 2\iota\kappa f_2(z_n)) \tag{2.85}$$

where

$$f_1(z_n) = F(z_n) + \nu \int_{-1}^{z_n} F(z_n') \sinh[\nu(z_n - z_n')]dz_n' \tag{2.86}$$

$$f_2(z_n) = \frac{1}{2} \int_{-1}^{z_n} F(z_n') \cosh[\nu(z_n - z_n')]dz_n' \tag{2.87}$$

Two singularities exist for Eqn. (2.85), namely at the leading and trailing edge. The singularity at the trailing edge is not physical, because the Joukowski condition are applied here, and this implies that $\Delta p(1) = 0$.

An explicit expression of the pressure difference distribution in Eqn. (2.85) is found here by another method than the one suggested in Graham (1970). The method uses the fact that $F(z_n)$ is known. Then the expressions can be manipulated to give the transfer function of the lift distribution.

When the following approximations are used

$$\sinh[\nu(z_n - z_n')] = \sum_{i=0}^{N}{}''\sum_{j=0}^{N}{}'' A_{ij}T_i(z_n)T_j(z_n') \tag{2.88}$$

$$\cosh[\nu(z_n - z_n')] = \sum_{i=0}^{N}{}''\sum_{j=0}^{N}{}'' B_{ij}T_i(z_n)T_j(z_n') \tag{2.89}$$

then Eqn. (2.85) becomes

$$
\begin{aligned}
\Delta p(z_n) &= \frac{1}{2}\rho c U_\infty w_0 \sum_{i=0}^{N}{}'' \left(\frac{2}{\pi\sqrt{1-z_n^2}}\sigma_i \right. \\
&\quad + \sum_{j=0}^{N}{}'' \left\{ \sum_{k=0}^{N}{}'' \frac{2}{\pi}\sigma_k(\nu A_{ij} - \imath\kappa B_{ij}) \int_{-1}^{z_n} \frac{1}{\sqrt{1-z_n'^2}} T_k(z_n')T_j(z_n')dz_n' \right\} \bigg) T_i(z_n) \\
&= \frac{1}{2}\rho c U_\infty w_0 \sum_{i=0}^{N}{}'' \left(\frac{2}{\pi\sqrt{1-z_n^2}}\sigma_i + \sum_{j=0}^{N}{}'' \left\{ \sum_{k=0}^{N}{}'' \frac{1}{\pi}\sigma_k(\nu A_{ij} - \imath\kappa B_{ij}) \right. \right. \\
&\quad \times \left. \left. \int_{-1}^{z_n} \frac{1}{\sqrt{1-z_n'^2}} (T_{k+j}(z_n') + T_{|k-j|}(z_n'))dz_n' \right\} \right) T_i(z_n).
\end{aligned}
\tag{2.90}
$$

The identity $T_k(z_n')T_j(z_n') = \frac{1}{2}\left(T_{k+j}(z_n') + T_{|k-j|}(z_n')\right)$, Fox and Parker (1968), is used in the equality. This can be further simplified to

$$
\begin{aligned}
\Delta p(z_n) &= \frac{1}{2}\rho c U_\infty w_0 \sum_{i=0}^{N}{}'' T_i(z_n) \left(\frac{2}{\pi\sqrt{1-z_n^2}}\sigma_i + \sum_{j=0}^{N}{}'' \left\{ \sum_{k=0}^{N}{}'' \frac{1}{\pi}\sigma_k(\nu A_{ij} - \imath\kappa B_{ij}) \right. \right. \\
&\quad \times \left. \left. \left[c_{k+j}(z_n) + c_{|k-j|}(z_n) \right] \right\} \right),
\end{aligned}
\tag{2.91}
$$

where the identity $T_h(x) = \cos\left\{h\cos^{-1}(x)\right\}$ is used to evaluate the integrals, which is $c_{k+j}(z_n)$ and $c_{|k-j|}(z_n)$, and has the value

$$
c_h(z_n) = -\frac{\sin\left(h\cos^{-1}z_n\right)}{h}, \qquad h \geq 1 \tag{2.92}
$$

$$
c_h(z_n) = \frac{\pi}{2} + \sin^{-1}z_n, \qquad h = 0. \tag{2.93}
$$

When ν is zero in Eqn. (2.91) the 1-D case is obtained, see Eqn. (2.45). Comparison of the two models shows that they coincide in this case, and this means that Eqn. (2.91) is validated for the 1-D case. The transfer function for a range of normalized wave numbers are shown in Figure 2.11 for leading edge, mid chord, and trailing edge. The figure shows that the lift distribution is decreasing when either the chordwise, the spanwise or both of the wave number are increased. This is expected because the fluctuations become so small in spatial scale, much smaller than the chord, so that the waves are averaged out.

The lift distribution can similar to Eqn. (2.51) be written as

$$
l(x, \kappa, \nu) = A(\rho, c, U)wg(x, \kappa, \nu) \tag{2.94}
$$
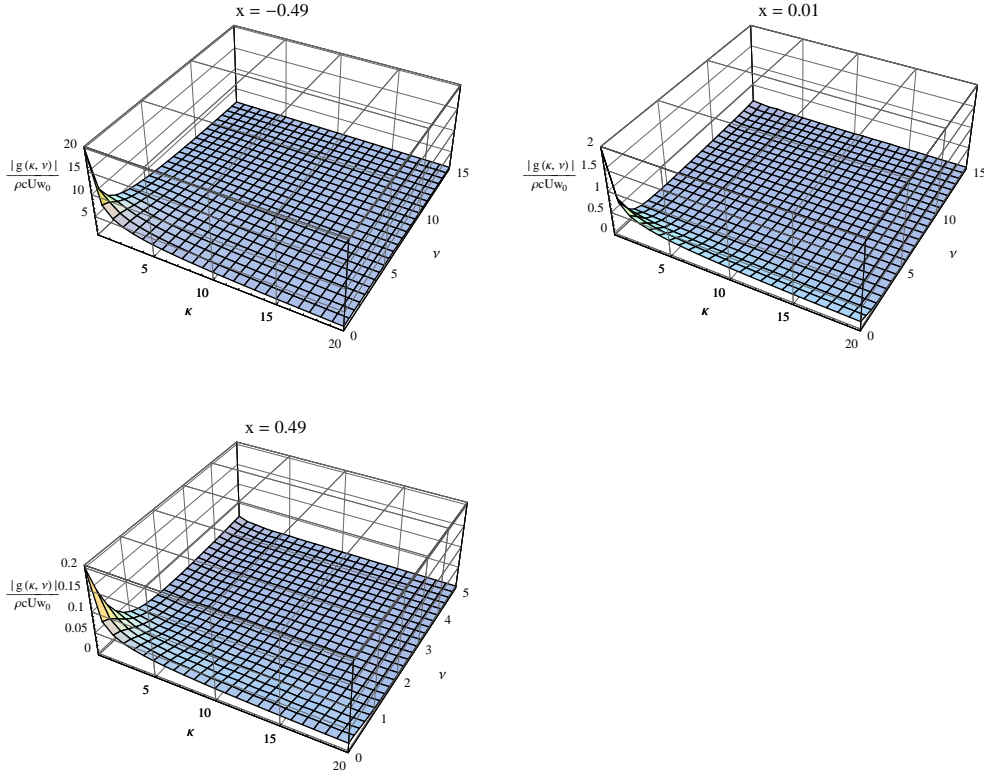
Figure 2.11: The transfer function for the lift distribution in the case of a 2-D gust. The positions are at $x = -0.49$, $x = 0.01$, and $x = 0.49$. The leading edge is defined as $x = -0.50$, the mid chord is defined as $x = 0.00$, and the trailing edge as $x = 0.50$. The wave numbers are normalized such that $\kappa = \frac{k_x c}{2}$ and $\nu = \frac{k_y c}{2}$. Note the different interval in ν at $x = 0.49$.

where $A(\rho, c, U)$ is defined in Eqn. (2.52) and $g(x, \kappa, \nu)$ is defined in Eqn. (2.91) by

$$
\begin{aligned}
g(x, \kappa, \nu) \;=\; & \sum_{i=0}^{N} {}'' T_i(z_n) \left(\frac{2}{\pi \sqrt{1 - z_n^2}} \sigma_i + \sum_{j=0}^{N} {}'' \left\{ \sum_{k=0}^{N} {}'' \frac{1}{\pi} \sigma_k (\nu A_{ij} - \imath \kappa B_{ij}) \right. \right. \\
& \left. \left. \times \left[c_{k+j}(z_n) + c_{|k-j|}(z_n) \right] \right\} \right).
\end{aligned}
\tag{2.95}
$$

Note that z_n is a function x as defined in Eqn. (2.76).

Figure 2.11 also shows that the magnitude of the transfer function is decreasing as the position at the aerofoil is changed from the leading edge

towards trailing edge. The model in Eqn. (2.91) has to be inspected because it gives unphysical results near the trailing edge when the spanwise wave number is increased at a fixed chordwise wave number.

2.2   Statistical Measures and their Properties

Statistics are useful when information of e.g. pressure and lift are obtained in two different spaces, which in this work are the wave number space and frequency space. When spectra of e.g. pressure and lift are found then the two spaces can be compared. This Section introduces properties and relations of spectra which will be used in Chapter 3 to inspect data and in Chapter 4 to compare data and models.

The pressure spectrum is calculated theoretically by

$$S_p(k_x, x) = A^2(\rho, c, U) \int_{-\infty}^{\infty} \Phi_{ww}(k_x, k_y)|g(x, k_x, k_2)|^2 dk_y. \tag{2.96}$$

where k_x is the chordwise wave number, k_y is the spanwise wave number, $A(\rho, c, U)$ is given in Eqn. (2.52), and $\Phi_{ww}(k_x, k_y)$ is the von Kármán (1948) spectrum of the vertical turbulence component. Further $g(x, k_x, k_y)$ is the transfer function for the lift distribution over the aerofoil and is given by Eqn. (2.53) or Eqn. (2.95) depending on whether it is the 1-D model or the 3-D model, respectively.

The lift spectrum is found by integrating pressure over a section of the aerofoil as

$$S_L(k_x) = A^2(\rho, c, U) \int_{-\infty}^{\infty} \Phi_{ww}(k_x, k_2) |g(k_x, k_2)|^2 dk_2 \tag{2.97}$$

where $A(\rho, c, U)$ and $\Phi_{ww}(k_x, k_2)$ are defined above, and $g(k_x, k_2)$ is the transfer function for the lift. The transfer function is given by Eqn. (2.50), Eqn. (2.67), or Eqn. (2.83) for the 1-D model, the 2-D model, or 3-D model, respectively. The wave number, k_2, is k_z or k_y in the 2-D model and in the 3-D model, respectively.

The property below is used throughout this thesis to compare data with models

$$f S_{var}(f) = k S_{var}(k), \quad k = \frac{2\pi f}{U} \tag{2.98}$$

where var is any variable such as wind speed, pressure, or lift etc. The models are defined for wave numbers whereas frequency information is obtained from data.

When the pressure is measured at different mean velocities the spectrum for the pressure scales with the mean velocity. This scaling is discussed here. In order to find it, we imagine we have two measurements. One timeseries is $x(t)$, the other experiment is run twice as fast and is given as $x_2(2t)$. It is understood that fluid particles are advected past the point twice as fast in the other measurement than in the first. The first gives a velocity and acceleration of $v(t)$ and $a(t)$ respectively. The other then gives $2v(2t)$ and $4a(2t)$ by partial differentiation with respect to t. Now pressure is related to acceleration by considering Navier-Stokes equation without any viscous forces, the so-called Euler equation,

$$\frac{\partial v_i}{\partial t} + v_j \frac{\partial v_i}{\partial x_j} = a_i = -\frac{\partial p}{\partial x_i} \tag{2.99}$$

thus pressure at the first measurement is $p(x,t)$ and the other is $4p(x,2t)$. The pressure spectrum is given as (von Kármán 1948)

$$S_p(f) = \int_{-\infty}^{\infty} R_{pp}(\tau) e^{i2\pi f \tau} d\tau \tag{2.100}$$

for the first time series, where the pressure co-variance function is $R_{pp}(\tau) = \langle p(x,0)p(x,t) \rangle$. The pressure spectrum for the other time series is

$$
\begin{aligned}
S_{p2}(f) &= \int_{-\infty}^{\infty} 16 \langle p(x,0)p(x,2\tau) \rangle e^{i2\pi f \tau} d\tau \\
&= \int_{-\infty}^{\infty} 16 R_{pp}(2\tau) e^{i2\pi f \tau} d\tau \\
&= \int_{-\infty}^{\infty} 16/2 R_{pp}(2\tau) e^{i2\pi \frac{f}{2} 2\tau} d(2\tau) \\
&= 8 S_p(f/2). \tag{2.101}
\end{aligned}
$$

Note the different subscripts. Now this can be generalized with $p(x,t)$ and $\gamma^2 p(x, \gamma t)$ (γ, a constant) to give

$$
\begin{aligned}
S_{p_\gamma}(f) &= \int_{-\infty}^{\infty} \gamma^4 \langle p(x,0)p(x,\gamma\tau) \rangle e^{i2\pi f \tau} d\tau \\
&= \int_{-\infty}^{\infty} \gamma^4/\gamma R_{pp}(\gamma\tau) e^{i2\pi \frac{f}{\gamma} \gamma\tau} d(\gamma\tau) \\
&= \gamma^3 S_p(f/\gamma). \tag{2.102}
\end{aligned}
$$

This leads to

$$\frac{f}{\gamma} S_p(f/\gamma) = f S_{p_\gamma}(f)/\gamma^4. \tag{2.103}$$
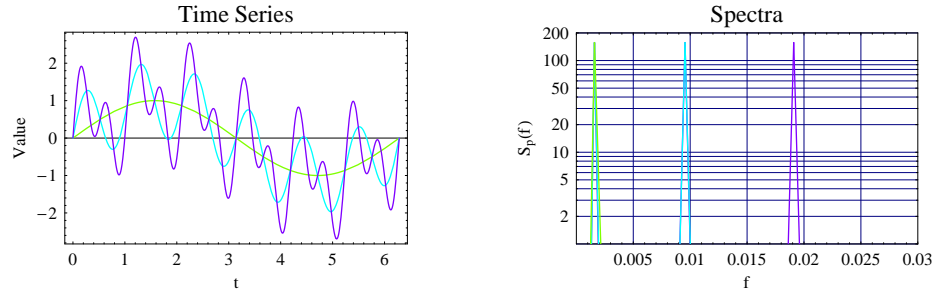
Figure 2.12: The purple line shows the total signal. The blue and green lines are low pass filtered. The spectra on the right plot show the effects of this filtering. The variances are in the example, green line: $\sigma^2 = 0.50$, blue line: $\sigma^2 = 1.00$, and purple line: $\sigma^2 = 1.50$.

This relation is used to compare if pressure spectra at different velocities scale with each other.

From the definition

$$\sigma_{var} = \sqrt{E_v[(x(t) - \bar{x})^2]} \tag{2.104}$$

where var is any variable, the standard deviation valid for a stationary time series $x(t)$ can be derived for a double sided spectrum to be

$$\sigma_{var} = \sqrt{2 \int_0^\infty S_{var}(f)df} \tag{2.105}$$

where var is any variable as above. The standard deviation in a specific frequency range can be found as

$$\sigma_{var,filter} = \sqrt{2 \int_{f_L}^{f_H} S_{var}(f)df} \tag{2.106}$$

where f_L and f_H are the low and high limit, respectively. Sometimes a time series contains useful information at certain frequencies and thus variance in a specific frequency range is wanted. The discrete version of Eqn. (2.106) is

$$\sigma_{var,filter} = \sqrt{2 \sum_{k=L}^{H} S_{var}(f_k)\Delta f_k} \tag{2.107}$$

When different instruments with different properties are used to measure the same quantity at the same time the statistics may not be comparable.

Instruments may have different frequency ranges in which they can measure. One instrument (I_1) which is able to measure up to a given frequency (f_1) is compared with another instrument (I_2) which is able to measure up to frequency (f_2) lower than f_1. The variance (σ^2_{var}) is not comparable, that is

$$\sigma^2_{var,I_1} \neq \sigma^2_{var,I_2} \qquad (2.108)$$

but the spectra are comparable in the frequency range they can measure, that is

$$S_{var,I_1}(f_i) = S(f_i)_{var,I_2}, \quad f_i \leq f_2. \qquad (2.109)$$

These two properties are illustrated in Figure 2.12.

2.3 Turbulence

Turbulence is a common state of fluids at high Reynolds numbers. It has several properties that are universal, some will be briefly described below. In this work the focus is exclusively on first-order and second-order statistics, such as spectra. Several models have been proposed to describe turbulence. The turbulence is assumed isotropic, this means that no direction is preferred. The model that will be used to describe isotropic turbulence is proposed by von Kármán (1948).

Turbulence is the fluctuations in velocity about a mean fluid velocity, and exists in every atmospheric flow. The standard deviation of these turbulent fluctuations in the wind is typically in the atmosphere in the order of 1 to 10 percent relative to the mean flow, Panofsky and Dutton (1984).

Turbulence can continuously be decomposed into sinusoidal waves. Thus the turbulence can be described by wave numbers, and in particular the energy spectrum tensor for isotropic turbulence can be described by the total kinetic energy Panofsky and Dutton (1984)

$$\Phi_{ij}(k_1, k_2, k_3) = \frac{E(k)}{4\pi \left(k^2\right)^2} \left(k^2 \delta_{ij} - k_i k_j\right) \qquad (2.110)$$

where the indices, i and j, are from 1 to 3 and k is the vector $\{k_1, k_2, k_3\}$. The indices number corresponds to U, V, and W, respectively in Φ_{ij}, and to x, y, and z in k_i. The direction for x, y, and z are chordwise, spanwise, and vertical, respectively. The turbulence spectrum for a given velocity component will have a shape that has a maximum at a certain wave number, k_{max} which is related to a certain eddy size. The maximum corresponds to a length scale, L_T, which is related as $k_{max} = \frac{1}{L_T}$. The size of an eddy is inversely proportional to the wave number. From the wave number where

the highest kinetic energy is found towards higher wave numbers, the energy
is transported from larger eddies to smaller eddies. This range of wave num-
bers is called the inertial subrange. The spectrum is decreasing as $k^{-5/3}$ in
the inertial subrange.

The energy is by the von Kármán (1948) model given as Mann (1994a)

$$E(k_x, k_y, k_z) = \alpha\epsilon^{2/3}\frac{\left(k_x^2 + k_y^2 + k_z^2\right)^2}{\left(k_x^2 + k_y^2 + k_z^2 + \frac{1}{L_T^2}\right)^{17/6}}. \tag{2.111}$$

The vertical energy spectrum, Φ_{ww} is of interest in this work because the
vertical wind component causes an upwash on the aerofoil, that gives a fluc-
tuating lift, see the previous section. When inserting Eqn. (2.111) into Eqn.
(2.110) and the ww-component is taken then

$$\phi(\mathbf{k}) = \Phi_{ww}(k_x, k_y, k_z) = \alpha\epsilon^{2/3}\frac{\left(k_x^2 + k_y^2\right)}{4\pi\left(k_x^2 + k_y^2 + k_z^2 + \frac{1}{L_T^2}\right)^{17/6}}. \tag{2.112}$$

In the 3-D model in the previous section the upwash is dependent on the
chordwise and spanwise wave number, that is k_x and k_y. When integrating
Eqn. (2.112) over all wave numbers then the 2-D energy spectrum is given
as

$$\Phi_{ww}(k_x, k_y) = \int_{-\infty}^{\infty}\Phi_{ww}(k_x, k_y, k_z)dk_z = \alpha\epsilon^{2/3}\frac{\left(k_x^2 + k_y^2\right)\Gamma\left(\frac{7}{3}\right)}{4\sqrt{\pi}\Gamma\left(\frac{17}{6}\right)\left(k_x^2 + k_y^2 + \frac{1}{L_T^2}\right)^{7/3}} \tag{2.113}$$

For the 1-D model in the previous section then Eqn. (2.113) is further inte-
grated over all k_y as

$$\Phi_{ww}(k_x) = \int_{-\infty}^{\infty}\Phi_{ww}(k_x, k_y)dk_y = \alpha\epsilon^{2/3}\frac{3L_T^{5/3}\left(8k_x^2L_T^2 + 3\right)}{110\left(k_x^2L_T^2 + 1\right)^{11/6}}. \tag{2.114}$$

The spectrum then gives the amplitude of the sinusoidal wave given the wave
number for both 1-D and 3-D models. The 2-D model needs a combination
because the wave numbers in $x-$ and $z-$direction are affecting the aerofoil.

The cross spectrum separated by a distance, Δy, in spanwise direction
can be derived, Kristensen and Jensen (1979). Then the coherence of the
w-component of turbulence given, Kristensen and Jensen (1979), as

$$coh_{ww}(k_x, \Delta y) = \frac{|\chi_{ww}(k_x, \Delta y)|^2}{|\chi_{ww}(k_x, 0)|^2} \tag{2.115}$$

can be found for isotropic turbulence. When the spectrum by von Kármán (1948) is used then the coherence becomes (Mann, Kristensen and Courtney 1991)

$$coh_{ww}(k_x, \Delta y) = \frac{\Delta y^{5/6} L_T (3 + 8k_x^2 L_T^2) K_{5/6}\left(\frac{\Delta y \sqrt{1+k_x^2 L_T^2}}{L_T}\right)}{12 L_T^{1/6} 2^{5/6} (1 + k_x^2 L_T^2)^{17/12}}$$
$$- \frac{3\Delta y^{11/6}\sqrt{1+k_x^2 L_T^2} K_{1/6}\left(\frac{\Delta y \sqrt{1+k_x^2 L_T^2}}{L_T}\right)}{12 L_T^{1/6} 2^{5/6} (1 + k_x^2 L_T^2)^{17/12}}. \quad (2.116)$$

where K_ν is the modified Bessel function of second kind of order ν as defined in Appendix A. Then the co-coherence can be found. It is defined as

$$coh^{1/2}(k_x, \Delta y) = \sqrt{coh_{ww}(k_x, \Delta y)}. \quad (2.117)$$

2.4   Inflow Noise Model

Inflow noise is a field of concern. The semi-empirical models that estimate the aerodynamical noise consist of models for different components of noise generated by the flow around an aerofoil. The inflow noise is the dominant component and is the subject of this section. It is believed based on measurements by Moriarty and Migliore (2003) and Oerlemans et al. (2007) that inflow noise does not have that high importance for the total noise as the inflow noise model suggests. The model for inflow noise is based on Amiet (1975), and this model is presented below.

2.4.1   Derivation of Acoustical Pressure Spectrum

The analysis is based on flat plate theory. In this case the vertical fluctuations in the flow are responsible for lift fluctuations. These force fluctuations give pressure fluctuations that can be observed far from the flat plate. Acoustic noise is pressure fluctuations that travel with the speed of sound. The task is to estimate the fraction of pressure fluctuations that are radiated acoustically given that the force fluctuations (lift fluctuations) are known.

The vertical turbulence component will in nature vary in all dimensions, i.e. horizontal, vertical, and in time. To simplify the analysis the turbulence is considered to be advected by the mean flow, so the structure and amplitude of turbulence are static in time. This is called frozen turbulence or Taylor's hypothesis. Further the vertical variation in the vertical turbulence component is assumed to have no effect on the lift fluctuations. Only

fluctuations in the plane of the plate have effect. The turbulence is assumed to be isotropic in space, also.

The vertical turbulence, $w(x, y, t)$, can be described as a Fourier transformation

$$w(x, y, t) = \int_{-\infty}^{\infty} \int_{-\infty}^{\infty} \hat{w}(k_x, k_y) \exp[\imath(k_x\{x - Ut\} + k_y y)]dk_x dk_y. \quad (2.118)$$

The pressure difference on the wing can be described as

$$\Delta P(x, y, t, k_x, k_y) = 2\pi\rho_0 U b w_F g(x, k_x, k_y) \exp[\imath(k_y y - k_x Ut)] \quad (2.119)$$

Where $b = \frac{c}{2}$, c is the chord length, and w_F is the Fourier amplitude of a given mode of k_x and k_y ($\hat{w}(k_x, k_y)$). The function $g(x, k_x, k_y)$ is a transfer function for how the pressure fluctuations on the aerofoil responds to a gust at a given chordwise position and can be given by Eqn. (2.53) or Eqn. (2.95). This transfer function is the wave number dependent part of the lift distribution. Eqn. (2.119) is identified as the lift distribution. Then

$$\Delta P(x, y, t) = 2\pi\rho_0 U b \int_{-\infty}^{\infty} \int_{-\infty}^{\infty} \hat{w}(k_x, k_y) g(x, k_x, k_y) \exp[\imath(k_y y - k_x Ut)]dk_x dk_y$$
$$(2.120)$$

When this is Fourier transformed into frequency space it reads

$$\begin{aligned}
\Delta \hat{P}_T(x, y, \omega) &= \frac{1}{2\pi} \int_{-T}^{T} \Delta P(x, y, t) \exp[-\imath\omega t]dt \\
&= 2\pi\rho_0 U b \frac{1}{2\pi} \int_{-T}^{T} \int_{-\infty}^{\infty} \int_{-\infty}^{\infty} \hat{w}(k_x, k_y) g(x, k_x, k_y) \\
&\quad \times \exp[\imath(k_y y - k_x Ut)] \exp[-\imath\omega t]dk_x dk_y dt. \quad (2.121)
\end{aligned}$$

By use of the relations

$$\lim_{T \to \infty} \int_{-T}^{T} \exp[\imath\gamma t]dt = 2\pi\delta(\gamma) \quad (2.122)$$

$$\delta(ax) = \frac{1}{|a|}\delta(x) \quad (2.123)$$

Eqn. (2.121) simplifies to

$$
\begin{aligned}
\Delta \hat{P}_T(x, y, \omega) &= \rho_0 U b \int_{-T}^{T} \int_{-\infty}^{\infty} \int_{-\infty}^{\infty} \hat{\hat{w}}(k_x, k_y) g(x, k_x, k_y) \exp[-\imath(\omega + k_x U)t] \\
&\quad \times \exp[\imath k_y y] dk_x dk_y dt \\
&= 2\pi \rho_0 U b \int_{-\infty}^{\infty} \int_{-\infty}^{\infty} \hat{\hat{w}}(k_x, k_y) g(x, k_x, k_y) \delta(\omega + k_x U) \exp[\imath k_y y] dk_x dk_y \\
&= 2\pi \rho_0 b \int_{-\infty}^{\infty} \hat{\hat{w}}(-\frac{\omega}{U}, k_y) g(x, -\frac{\omega}{U}, k_y) \exp[\imath k_y y] dk_y \\
&= 2\pi \rho_0 b \int_{-\infty}^{\infty} \hat{\hat{w}}(K_x, k_y) g(x, K_x, k_y) \exp[\imath k_y y] dk_y.
\end{aligned} \tag{2.124}
$$

The only chordwise frequency excited is $K_x = -\omega/U$.

The cross spectrum is

$$
S_{QQ}(x_1, x_2, y_1, y_2, \omega) = \lim_{T \to \infty} \left\{ \frac{\pi}{T} \overline{\langle \Delta \hat{P}_T(x_1, y_1, \omega), \Delta \hat{P}_T(x_2, y_2, \omega) \rangle} \right\}. \tag{2.125}
$$

When looking at Eqn. (2.124) the only statistical quantity is $\hat{\hat{w}}(K_x, k_y)$. That is

$$
\begin{aligned}
S_{QQ}(x_1, x_2, y_1, y_2, \omega) &= (2\pi \rho_0 b)^2 \\
&\quad \times \int_{-\infty}^{\infty} \int_{-\infty}^{\infty} \lim_{T \to \infty} \left\{ \frac{\pi}{T} \overline{\langle \hat{\hat{w}}(K_x, k_y) \hat{\hat{w}}(K_x, k_y') \rangle} \right\} \\
&\quad \times \overline{g(x_1, K_x, k_y)} g(x_2, K_x, k_y') \\
&\quad \times \exp[-\imath(k_y y_1 - k_y' y_2)] dk_y dk_y'.
\end{aligned} \tag{2.126}
$$

In order to get a continuous representation of the frequency the time (T) has to go to infinity when operating with statistical quantities.

$$
\begin{aligned}
\overline{\langle \Delta \hat{P}_T(x_1, y_1, \omega), \Delta \hat{P}_T(x_2, y_2, \omega) \rangle} &= (2\pi \rho_0 b)^2 \int_{-\infty}^{\infty} \int_{-\infty}^{\infty} \overline{\langle \hat{\hat{w}}(K_x, k_y) \hat{\hat{w}}(K_x, k_y') \rangle} \\
&\quad \times \overline{g(x_1, K_x, k_y)} g(x_2, K_x, k_y') \\
&\quad \times \exp[-\imath(k_y y_1 - k_y' y_2)] dk_y dk_y'
\end{aligned} \tag{2.127}
$$

The mean vertical velocity spectrum can be described by

$$
\overline{\langle \hat{\hat{w}}(K_x, k_y), \hat{\hat{w}}(K_x, k_y') \rangle} = \frac{R}{\pi} \delta(k_y - k_y') \Phi_{ww}(K_x, k_y') \tag{2.128}
$$

where $\Phi_{ww}(K_x, k_y')$ is the energy spectrum of the vertical velocity fluctuations as defined in Eqn. (2.113), and R is the distance over which $\hat{\hat{w}}(K_x, k_y')$ is

integrated to find Eqn. (2.128). Further

$$\lim_{T \to \infty} \left(\frac{R}{T} \right) = U. \tag{2.129}$$

Use of Eqn. (2.128) in Eqns. (2.125) and (2.127) gives

$$
\begin{aligned}
S_{QQ}(x_1, x_2, y_1, y_2, \omega) &= \lim_{T \to \infty} \{ (2\pi\rho_0 b)^2 \frac{\pi}{T} \int_{-\infty}^{\infty} \int_{-\infty}^{\infty} \frac{R}{\pi} \delta(k_y - k_y') \\
&\quad \times \Phi_{ww}(K_x, k_y') \overline{g(x_1, K_x, k_y)} g(x_2, K_x, k_y') \\
&\quad \times \exp[-\imath(k_y y_1 - k_y' y_2)] dk_y dk_y' \} \\
&= U(2\pi\rho_0 b)^2 \int_{-\infty}^{\infty} \Phi_{ww}(K_x, k_y) \overline{g(x_1, K_x, k_y)} \\
&\quad \times g(x_2, K_x, k_y) \exp[\imath k_y \eta] dk_y \tag{2.130}
\end{aligned}
$$

where $\eta = y_2 - y_1$ is the spanwise separation distance.

The effective distance traveled from the emitting point to the receiver because of advection by the mean flow is

$$\sigma = \sqrt{x^2 + \beta^2(y^2 + z^2)} \tag{2.131}$$

where $\beta = \sqrt{1 - M^2}$. When the pressure fluctuations on the surface of the aerofoil are known then the acoustic pressure at the receiver position is (Amiet 1975)

$$
\begin{aligned}
P_1(x, y, z, \omega, x_0, y_0) &= \frac{\imath \omega z F(x_0, y_0, \omega)}{4\pi c_0 \sigma^2} \exp\left[\imath \omega \left(t + \frac{M(x - x_0) - \sigma}{c_0 \beta^2} + \frac{xx_0 + yy_0 \beta^2}{c_0 \beta^2 \sigma} \right) \right] \\
&= \frac{\imath \omega z \Delta \hat{P}_T(x_0, y_0, \omega)}{4\pi c_0 \sigma^2} \\
&\quad \times \exp\left[\imath \omega \left(t + \frac{M(x - x_0) - \sigma}{c_0 \beta^2} + \frac{xx_0 + yy_0 \beta^2}{c_0 \beta^2 \sigma} \right) \right]. \tag{2.132}
\end{aligned}
$$

An oscillating force produces a dipole radiation. The expression in Eqn. (2.132) is valid in the far field, where the acoustical pressure of a dipole fall of inversely to the square of the distance. The cross spectrum of the acoustic

pressure in the far field is then

$$
\begin{aligned}
S_{PP}(x, y, z, \omega) &= \lim_{T \to \infty} \{ \frac{\pi}{T} \int_{-b}^{b} \int_{-b}^{b} \int_{-d}^{d} \int_{-d}^{d} \\
&\quad \overline{\langle P_1(x, y, z, \omega, x_1, y_1), P_1(x, y, z, \omega, x_2, y_2) \rangle} dy_1 dy_2 dx_1 dx_2 \} \\
&= \left(\frac{\omega z}{4\pi c_0 \sigma^2} \right)^2 \int_{-b}^{b} \int_{-b}^{b} \int_{-d}^{d} \int_{-d}^{d} \lim_{T \to \infty} \{ \frac{\pi}{T} \overline{\langle \Delta \hat{P}_T(x_1, y_1, \omega), \Delta \hat{P}_T(x_2, y_2, \omega) \rangle} \} \\
&\quad \exp \left[\imath \frac{\omega}{c_0 \beta^2} \{ (x_1 - x_2)(M - x/\sigma) + y\beta^2 \eta/\sigma \} \right] dy_1 dy_2 dx_1 dx_2 \\
&= \left(\frac{\omega z}{4\pi c_0 \sigma^2} \right)^2 \int_{-b}^{b} \int_{-b}^{b} \int_{-d}^{d} \int_{-d}^{d} S_{QQ}(x_1, x_2, y_1, y_2, \omega) \\
&\quad \exp \left[\imath \frac{\omega}{c_0 \beta^2} \{ (x_1 - x_2)(M - x/\sigma) + y\beta^2 \eta/\sigma \} \right] dy_1 dy_2 dx_1 dx_2 \quad (2.133)
\end{aligned}
$$

where d is the half span. An acoustic lift is found as

$$
\mathcal{L}(x, K_x, k_y) = \int_{b}^{b} g(x_0, K_x, k_y) \exp \left[-\imath \omega x_0 (M - x/\sigma)/c_0 \beta^2 \right] dx_0. \quad (2.134)
$$

It is called acoustic because it is the integrated lift distribution advected by an acoustic wave, i.e. the acoustical pressure fluctuation in the far field due to the fluctuating lift distribution on the aerofoil. Now the cross spectrum

of the acoustic pressure can be simplified

$$
\begin{aligned}
S_{PP}(x,y,z,\omega) &= \left(\frac{\omega z}{4\pi c_0\sigma^2}\right)^2 U(2\pi\rho_0 b)^2 \int_{-\infty}^{\infty}\int_{-b}^{b}\int_{-b}^{b}\int_{-d}^{d}\int_{-d}^{d} \\
&\quad \times \exp[\imath k_y\eta]\Phi_{ww}(K_x,k_y)\overline{g(x_1,K_x,k_y)}g(x_2,K_x,k_y) \\
&\quad \times \exp\left[\imath\frac{\omega}{c_0\beta^2}\left\{(x_1-x_2)(M-x/\sigma)+y\beta^2\eta/\sigma\right\}\right]dy_1 dy_2 dx_1 dx_2 dk_y \\
&= \left(\frac{\omega z\rho_0 b}{2c_0\sigma^2}\right)^2 U\int_{-\infty}^{\infty}|\mathcal{L}(x,K_x,k_y)|^2\Phi_{ww}(K_x,k_y) \\
&\quad \times \int_{-d}^{d}\int_{-d}^{d}\exp\left[\imath\eta\left(\frac{\omega y}{c_0\sigma}+k_y\right)\right]dy_1 dy_2 dk_y \\
&= \left(\frac{\omega z\rho_0 b}{2c_0\sigma^2}\right)^2 U\int_{-\infty}^{\infty}\left(\frac{2\sin\left(d\left[k_y+\frac{\omega y}{c_0\sigma}\right]\right)}{k_y+\frac{\omega y}{c_0\sigma}}\right)^2 \\
&\quad \times |\mathcal{L}(x,K_x,k_y)|^2\Phi_{ww}(K_x,k_y)dk_y \\
&= \left(\frac{\omega z\rho_0 b}{c_0\sigma^2}\right)^2 U\pi d\int_{-\infty}^{\infty}\frac{\sin^2\left(d\left[k_y+\frac{\omega y}{c_0\sigma}\right]\right)}{\left(k_y+\frac{\omega y}{c_0\sigma}\right)^2\pi d} \\
&\quad \times |\mathcal{L}(x,K_x,k_y)|^2\Phi_{ww}(K_x,k_y)dk_y.
\end{aligned}
\tag{2.135}
$$

The following identity can be used to simplify Eqn. (2.135) further

$$
\lim_{d\to\infty}\left[\frac{\sin^2(\xi d)}{\xi^2\pi d}\right] = \delta(\xi).
\tag{2.136}
$$

When $d\to\infty$ and the plane in interest is the $y=0$-plane then Eqn. (2.135) can be approximated to

$$
\begin{aligned}
S_{PP}(x,0,z,\omega) &= \left(\frac{\omega z\rho_0 b}{c_0\sigma^2}\right)^2 U\pi d \\
&\quad \times \int_{-\infty}^{\infty}\delta(k_y)|\mathcal{L}(x,K_x,k_y)|^2\Phi_{ww}(K_x,k_y)dk_y \tag{2.137} \\
&\approx \left(\frac{\omega z\rho_0 b}{c_0\sigma^2}\right)^2 U\pi d|\mathcal{L}(x,K_x,0)|^2\Phi_{ww}(K_x,0). \tag{2.138}
\end{aligned}
$$

This approximation uses that

$$
f(D,d) = \int_0^D \sin^2(\xi d)\frac{d\xi}{\xi^2} = -\frac{\sin^2(Dd)}{D}+dSi(2Dd)
\tag{2.139}
$$

where $Si(D) = \int_0^D \frac{\sin t}{t} dt$. The integral in Eqn. (2.137) obtains most of its value close to $D = 0$ because

$$\lim_{r \to \infty} \{f(\frac{10}{d}, d)/f(\frac{r}{d}, d)\} = 0.9668. \tag{2.140}$$

The approximation in Eqn. (2.138) is thus under the assumption that $|\mathcal{L}(x, K_x, k_y)|^2$ and $\Phi_{ww}(K_x, k_y)$ does not vary much in the integration range given by Eqn. (2.140).

2.4.2 Estimation of one third octave Sound Pressure Level

The spectrum of the acoustic pressure in far field is from Eqn. (2.138) found to be (Amiet 1975)

$$S_{PP}(0, 0, z, \omega) = \left(\frac{\omega \rho_0 b}{c_0 z}\right)^2 \pi U d |G(\hat{\omega})|^2 \Phi_{ww}(K_x, 0) \tag{2.141}$$

where $G(\hat{\omega})$ is the transfer function from Adamczyk (1974) and $K_x = -\frac{\omega}{U}$. In the high frequency limit the transfer function becomes

$$\lim_{\omega \to \infty} G(\hat{\omega}) = \frac{-\imath}{\pi \hat{\omega} \sqrt{M}}, \quad \hat{\omega} = \frac{\omega b}{U}, \quad M = \frac{U}{c_0} \tag{2.142}$$

and then

$$|G(\hat{\omega})|^2 = \frac{U c_0}{(\pi \omega b)^2}. \tag{2.143}$$

$\Phi_{ww}(k_x, k_y)$ from Eqn. (2.113) is reformulated by Amiet (1975) as

$$\Phi_{ww}(k_x, k_y) = \frac{4}{9\pi} \frac{\overline{u^2}}{k_e^2} \frac{\hat{k}_x^2 + \hat{k}_y^2}{(1 + \hat{k}_x^2 + \hat{k}_y^2)^{7/3}} \tag{2.144}$$

where $k_e = \frac{\sqrt{\pi}}{L_T} \frac{\Gamma(5/6)}{\Gamma(1/3)}$, $\hat{k}_x = \frac{k_x}{k_e}$, and $\hat{k}_y = \frac{k_y}{k_e}$. Then the energy spectrum of the w-component of turbulence in Eqn. (2.141) is

$$\Phi_{ww}(K_x, 0) = \frac{4}{9\pi} \frac{\overline{u^2}}{k_e^2} \frac{\hat{K}_x^2}{(1 + \hat{K}_x^2)^{7/3}}. \tag{2.145}$$

Inserting Eqn. (2.145) and Eqn. (2.143) in Eqn. (2.138) then

$$
\begin{aligned}
S_{PP}(0,0,z,\omega) &= \left(\frac{\rho_0}{z}\right)^2 \frac{U^2 dL^2}{\pi^3 c_0}\left(\frac{2}{3}\right)^2 \overline{u^2}\left[\frac{\Gamma(1/3)}{\Gamma(5/6)}\right]^2 \frac{\hat{K}_x^2}{(1+\hat{K}_x^2)^{7/3}} \\
&= \frac{d}{\pi c_0}\left(\frac{2L_T}{3\pi z}\right)^2 \frac{\overline{u^2}}{U^2}(\rho_0 U^2)^2\left[\frac{\Gamma(1/3)}{\Gamma(5/6)}\right]^2 \frac{\hat{K}_x^2}{(1+\hat{K}_x^2)^{7/3}} \\
&= \left(\frac{\rho_0}{\pi}\right)^2 \frac{4}{9}c_0^3 \frac{\overline{u^2}}{U^2}M^4 d\frac{\Gamma(1/3)}{\Gamma(5/6)}\frac{L_T}{z^2\sqrt{\pi}}\frac{\hat{K}_x^2}{k_e(1+\hat{K}_x^2)^{7/3}} \quad (2.146)
\end{aligned}
$$

Before the sound pressure level in the one-third octave band, $\text{SPL}_{1/3}$ is estimated, we look at the definitions of the one-third octave band. The center frequency, the lower limit, and the upper limit of an one-third octave band are defined by

$$
\begin{aligned}
f_c &= 1000\cdot 10^{0.1i}, &i \in \mathbb{Z} \land i \in [-20,13] & \quad (2.147) \\
f_L &= 1000\cdot 10^{0.1(i-0.5)}, &i \in \mathbb{Z} \land i \in [-20,13] & \quad (2.148) \\
f_H &= 1000\cdot 10^{0.1(i+0.5)}, &i \in \mathbb{Z} \land i \in [-20,13] & \quad (2.149)
\end{aligned}
$$

which imply that the center frequency is between 10Hz and 20.0kHz. Then the center frequency is defined in the human hearing range. This implies that the frequency range of a band is

$$
\Delta f = f_H - f_L = f_c(10^{0.05} - 10^{-0.05}) \approx 0.231 f_c \quad (2.150)
$$

Further $\Delta\omega = 2\pi\Delta f = 2\pi 0.231 f_c = 0.231\omega_c$ The sound pressure level in the one-third octave band, $\text{SPL}_{1/3}$ is given by

$$
\text{SPL}_{1/3} = 10\log_{10}\left[\frac{2S_{PP}\Delta\omega}{p_{ref}^2}\right], \quad p_{ref} = 2\cdot 10^{-5}\text{Pa}. \quad (2.151)
$$

When inserting Eqn. (2.146) in Eqn. (2.151) and recalling $K_x = -\frac{\omega}{U}$, it is seen that the expression in square brackets is dimensionless. S_{PP} is derived for a double sided distribution of wave numbers and thus it is necessary to multiply with 2 to get the estimate for positive frequencies. The estimate of

the sound pressure level in the one-third octave band becomes then

$$
\begin{aligned}
\mathrm{SPL}_{1/3} &= 10\log_{10}\left[\frac{0.231\cdot 10^{10}}{2}\omega_c\left(\frac{\rho_0}{\pi}\right)^2\frac{4}{9}c_0^3\frac{\overline{u^2}}{U^2}M^4 d\frac{\Gamma(1/3)}{\Gamma(5/6)}\frac{L_T}{z^2\sqrt{\pi}}\frac{\hat{K}_x^2}{k_e(1+\hat{K}_x^2)^{7/3}}\right]\\
&= 10\log_{10}\left[\frac{0.231\cdot 10^{10}}{2}\left(\frac{\rho_0}{\pi}\right)^2\frac{4}{9}c_0^4\frac{\overline{u^2}}{U^2}M^5 d\frac{\Gamma(1/3)}{\Gamma(5/6)}\frac{L_T}{z^2\sqrt{\pi}}\frac{\hat{K}_x^3}{(1+\hat{K}_x^2)^{7/3}}\right]\\
&= 10\log_{10}\left[\frac{L_T d}{z^2}\frac{\overline{u^2}}{U^2}M^5\frac{\hat{K}_x^3}{(1+\hat{K}_x^2)^{7/3}}\right]\\
&\quad +10\log_{10}\left[\frac{0.231\cdot 10^{10}}{2}\frac{4}{9\sqrt{\pi}}\frac{\Gamma(1/3)}{\Gamma(5/6)}\left(\frac{\rho_0}{\pi}\right)^2 c_0^4\right].
\end{aligned}
\tag{2.152}
$$

The density of air, ρ_0, is set to 1.2 kg/m^3 and the speed of sound in air, c_0, is set to 340 m/s (Amiet 1975) then Eqn. (2.152) becomes

$$
\mathrm{SPL}_{1/3} = 10\log_{10}\left[\frac{L_T d}{z^2}\frac{\overline{u^2}}{U^2}M^5\frac{\hat{K}_x^3}{(1+\hat{K}_x^2)^{7/3}}\right]+181.3.
\tag{2.153}
$$

This is used in Moriarty and Migliore (2003) to estimate the noise due to atmospheric turbulence.

The sound pressure level due to atmospheric turbulence can alternatively be calculated by using Eqn. (2.137) in Eqn. (2.151) and the transfer function for lift distribution in Eqn. (2.53) or Eqn. (2.95).

2.5 Other Aeroacoustic Sources

The noise generated from an aerofoil, the so-called aero-acoustical noise, is caused by several mechanisms (Wagner et al. 1996). The main subject of this work is inflow noise, noise due to atmospheric turbulence. In this section noise due to other mechanisms (Wagner et al. 1996) will be discussed briefly.

Trailing edge noise occurs as a swishing sound in the frequency range of 500 to 1000 Hz. It is due to turbulent eddies in the boundary layer very close to the surface of the aerofoil. When these turbulent eddies pass the trailing edge they are scattered and thus the design of the trailing edge is a key factor for the amount of trailing edge noise. Further the structure of the boundary layer is important for the trailing edge noise.

Noise due to vortex shedding in a laminar boundary layer occurs at a low Reynolds number, below approximately 10^6. It is tonal of character and is caused by interaction of upstream traveling trailing edge (see above) generated acoustic waves and aerodynamic instabilities.

Tip Noise is a broadband phenomenon. It is as trailing edge noise due to scattered turbulence and is dependent on design. Tip noise is believed to be responsible for an increase of 1 to 2dB of the total sound pressure level due to aero-acoustics in parts of the frequency range.

Noise from turbulence caused by separation is of the same nature as trailing edge noise. The noise is due to scattered turbulence from the trailing edge, in this case the size of the eddies is covering a larger range. When the flow is fully separated from the leading edge, i.e. at stall, then the noise is generated from the whole aerofoil. The noise due to separation and stall is of broadband nature.

The shape of the trailing edge is causing noise as well. The design of the trailing edge is important for how much noise is produced because the trailing edge is not perfectly sharp, i.e. the trailing edge is blunt. The thickness of the trailing edge and the height of the boundary layer are key parameters to estimate the bluntness noise from the trailing edge. The thickness of the trailing edge is furthermore dependent on the shaping of the trailing edge. The bluntness noise is a narrow band and tonal phenomenon. The size of the narrow band is dependent on the shaping.

Practical issues as e.g. weathering and production tolerances cause noise as well. This means that uncontrollable factors in the operation of the turbine cause aerodynamically generated noise. This type of noise is not predictable.

2.6   Conclusions Regarding Theory

The purpose of the derivations in the previous sections is to show the details of existing theory. The theory will be applied in the analysis of data. The models presented in this chapter are dimensionless which gives confidence that the models can be used for several purposes.

The basic aerodynamics is described in the framework of potential theory. A 1-D model is derived with details. The 1-D model is based on Sears (1941) and predicts transfer functions for the fluctuations of lift distribution at any point on a flat plate and for the fluctuations of the lift on the plate. The gust responsible for the pressure and lift fluctuations on the aerofoil is vertical and has a wave component in the direction of mean flow. The transfer function for the lift fluctuations gives the Sears function, $S(\kappa)$, which is a basic result in unsteady aerodynamics.

A 2-D model, Goldstein and Atassi (1976) and Atassi (1984), is presented which predicts the transfer function for the lift fluctuations for a flat plate that can be bend in a parabolic fashion and placed at an angle of attack (AOA) to the mean flow. The two parameters, camber (the plate is bend)

and AOA, give a mean lift. Thus the 2-D model is able to predict the lift fluctuations at aerodynamically conditions that are similar to the conditions that an aerofoil experiences in a real flow. The gust responsible for the lift fluctuations is 2-D, and it has a component in the direction of the mean flow and a component in the vertical direction.

A 3-D model, Graham (1970), is discussed which predicts the lift fluctuations for a flat plate that extends in chord wise and spanwise direction. The flat 2-D flat plate experiences a vertical gust with a wave front that can be skewed to the leading edge of the plate. A method is developed to describe the fluctuations of the lift distribution in chord wise direction.

The 1-D model by Sears (1941) and the 2-D model by Goldstein and Atassi (1976) do not account for spanwise effects of the gust, which the 3-D model by Graham (1970) does. The unsteady inflow on an aerofoil will have spanwise variations and it is therefore important to take these variations in account as the 3-D model does. The 3-D effects due to the finite length of the aerofoil and variation in spanwise variation in the thickness and width of the aerofoil are assumed to be negligible.

The energy spectrum of isotropic turbulence, von Kármán (1948), is described. The coherence of the vertical wind component, w, with a spanwise separation distance is presented, Mann et al. (1991). The statistical theory to obtain pressure and lift spectra from the turbulence energy spectra and transfer functions of lift distribution and lift is discussed. Several properties of spectra is shown as well.

The waves are in the 1-D case and in the 2-D case considered to be advected over the aerofoil. Turbulence can be regarded as consisting of waves equally distributed in all directions when it is isotropic. This implies that all waves with a given wave number, k_x, in the direction of the mean flow have to be included in the 1-D and 2-D models, when the pressure or lift is found.

An acoustical model is described and the details derived that predicts noise due to atmospheric turbulence, Amiet (1975). The model assumes that the noise is emitted as a dipole. The model uses as input a transfer function for the fluctuations of lift distribution and is based on the oscillations of a flat plate. The output of the model is the sound pressure level (SPL) in the third octave frequency band.

The lift fluctuations are sufficient for estimating sound emission in the far field at low Mach numbers as described in Howe (2003). The low frequencies will not be affected by the retarded time differences because the phase is almost identical from various positions on the chord as seen from a receiver point in the far field, and the high frequencies are not important because they are outside the scope of this thesis. The aerodynamical pressure is used in the acoustical model, because the Mach number is low.

Chapter 3

Experiments

The aim of the experiments was to obtain knowledge of aerodynamic pressure phenomena at the surface of an aerofoil. Microphones were mounted on the surface in order to obtain measurements of high frequency resolution of the pressure fluctuations at different positions at the surface of the aerofoil. Similar previous experiments has been made by Risø, DTU at lower frequency resolution by using pressure tabs to measure the mean pressure.

Only the aerodynamical pressure were measured. These are used to validate the unsteady aerodynamical models described in Chapter 2.

3.1   Setup of Experiments in Velux Wind Tunnel

The wind tunnel used to obtain the measurements analyzed below is owned by the window manufacturer, Velux, and it is located 10 km northeast of Horsens in Denmark. It is mainly used for tests of new product components, and it is rented to external users for multiple purposes. The wind tunnel is an open jet wind tunnel. The maximum wind speed of the tunnel is 40m/s and the turbulence intensity is approximately 1%. A sketch of the wind tunnel is shown in Figure 3.1. The test section of the tunnel (no. 4 and 5 in Figure 3.1) is 10.5 m long from the inlet of the jet to the outlet and 7.5 m wide. The height in the test section is 7.5 m. A detailed sketch of the test section is seen in Figures 3.6 and Figure 3.11. The vertical and horizontal profile of the jet are assumed to be constant. The conditions for measurements in Velux Wind tunnel are treated in detail in Fuglsang, Antoniou, Sørensen and Madsen (1998).

The experiments were conducted in December 2006 and in June 2007. The microphones used in both experiments are of type Sennheiser KE-4-211-
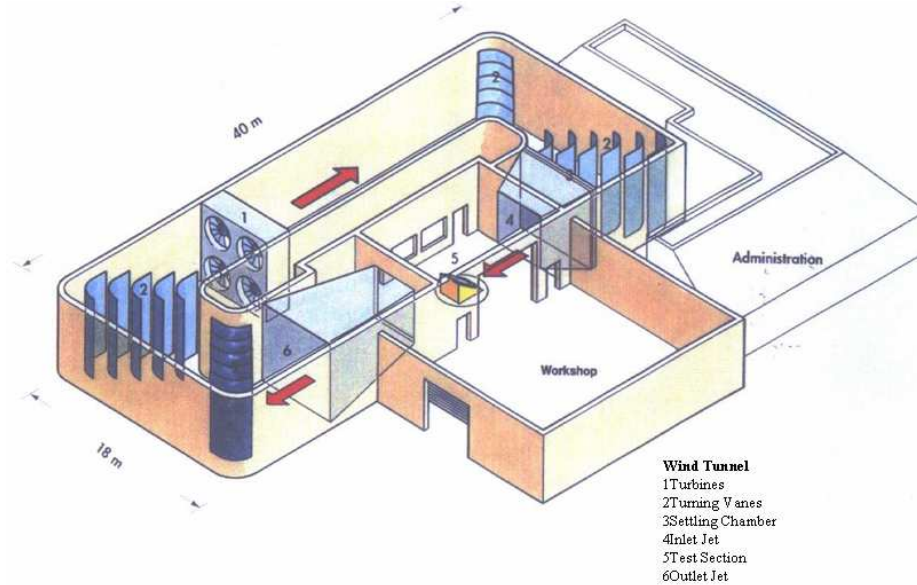
Figure 3.1: Sketch of Velux wind tunnel.

2, and they have a sampling frequency of maximum 50 kHz. The response function given by the manufacturer is constant in the range between 20Hz and 20kHz. Measurements of the pressure fluctuations at the surface of the aerofoil are also obtained with pressure tabs, and they have a sample frequency of maximum 400 Hz but most of the samples are obtained at 100 Hz.

The signal from the microphones was in Volts. The description of the microphones shows that the sensitivity is 10 mV/Pa. This is used to convert the Volt signals into pressure (Pascal). When the Volt signal is multiplied with 100 then the pressure is obtained. The properties of spectra then gives

$$S_p(f) = 100^2 S_V(f). \tag{3.1}$$

This property is used in the plots for microphones shown in this chapter. The plots are thus with $S_p(f)$ in units of Pa^2s.

The microphones were placed in a device which was mounted such that it was flush with the surface of the aerofoil. The way the microphone was mounted in the device left a chamber between the membrane of the microphone and the surface of the aerofoil. The design of the chamber is shown in Figure 3.2. The chamber caused the signal to be unreliable above a cut-off frequency, which is dependent on the dimensions of the chamber between

Figure 3.2: Sketch of the chamber attached to the aerofoil. The dimensions necessary to calculate the cut-off frequency is shown. Further the mean wind, U, is shown.

the microphone and the surface of the aerofoil. The cut-off frequency can be estimated by the theory of a Helmholtz resonator. The eigenfrequency of a Helmholtz resonator is given by Martin, Mus and Mus (2004)
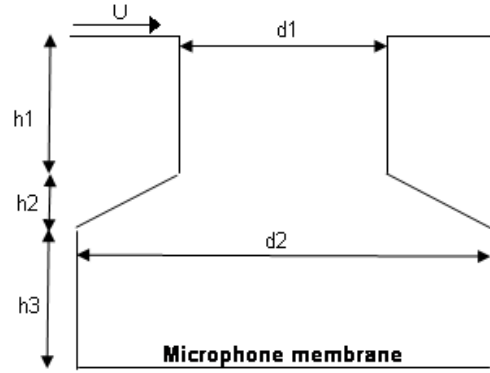
$$f_H = \frac{c_0}{2\pi} \sqrt{\frac{S_{cav}}{L'_e V_{cav}}} \tag{3.2}$$

where c_0 is the speed of sound, S_{cav} is the area of the hole of the chamber flush with surface of the aerofoil $(\pi(d_1/2)^2)$. The length of the tube in the device in which the microphone is mounted is h_1, where L'_e is the effective length of a flanged tube given by $L'_e = h_1 + 1.7 d_1/2$ (Martin et al. 2004), $d_1/2$ is the radius of the tube/hole. The volume of the chamber not including the volume of the tube is V_{cav}. Specific values of the eigenfrequency of a Helmholtz resonator in the experiments described in this Chapter are given in the end of Sections 3.1.1 and 3.1.2. The eigenfrequencies are different in the two experiments because the device in which the microphones were mounted was redesigned to increase the eigenfrequency in the second experiment. The change was made to increase the frequency range of the pressure signal.

The angles of attack, AOA's, are corrected due to the fact that the jet is deflected by the proximity of the aerofoil to the floor. The vertical distance was 1.7m and this can have an influence on the jet when the suction side is against the floor, i.e. at negative angles of attack. The drag, the lift and the C_p curve from the pressure tabs data are corrected to give a free stream angle of attack by the method of Fuglsang et al. (1998) and Gaunaa, Fuglsang, Bak and Antoniou (2004). The range of AOA's is $-5°$ to $10°$ for

x [mm]	y [mm]	Mic no.
2.0	-60.0	11
24.8	-60.0	10
75.7	70.0	4
75.7	-40.0	5
75.7	-60.0	6
75.7	-70.0	7
75.7	-120.0	8
75.7	-130.0	9
113.5	-60.0	3
448.5	-60.0	2
917.2	-60.0	1

Table 3.1: Position on the NACA0015 profile of the 11 microphones.

d_1	0.5mm
d_2	4.7mm
h_1	5mm
h_2	0.4mm
h_3	0.4mm
S_{cav}	$1.96{\cdot}10^{-7}\mathrm{m}^2$
L_e'	$5.4{\cdot}10^{-3}\mathrm{m}$
V_{cav}	$9.53{\cdot}10^{-9}\mathrm{m}^3$

Table 3.2: The dimensions of the chamber of the device in which the microphone are mounted in the experiment with a NACA0015 profile. See also Figure 3.2

the NACA0015 profile by this method in the first experiment. The range of AOA's is not symmetrical probably because of the relative wide chord (1m) in combination with the short vertical distance from the floor to the aerofoil. The NACA63415 profile in the second experiment is by experience known to have a range of AOA of -20° to 10° in which the measurements are valid (Fuglsang et al. 1998).

The zero lift AOA is for NACA0015 0° because this profile is symmetrical, and for the asymmetrical NACA63415 it is approximately −1.5° (Abbott and von Doenhoff 1959).

The section of an aerofoil used in both experiments has a span of 1.90m and is mounted on a plate in each end, see the picture in Figure 3.3. The assumption is made that the measurement of pressure by pressure tabs and microphones is not affected by the flow around and the flow induced by the end plates.

The coordinate system through out this chapter is defined with the x-axis in chordwise direction with zero at the leading edge and positive in the direction towards the trailing edge. The y-axis is in spanwise direction and is zero at midspan. The z-axis is depicting the thickness and is positive towards the suction side of the aerofoil.

3.1.1 Setup of Experiment 1: NACA0015

In this experiment 11 microphones were placed on the suction side (the upper side) on an aerofoil with a NACA0015 profile. The dimensions of the
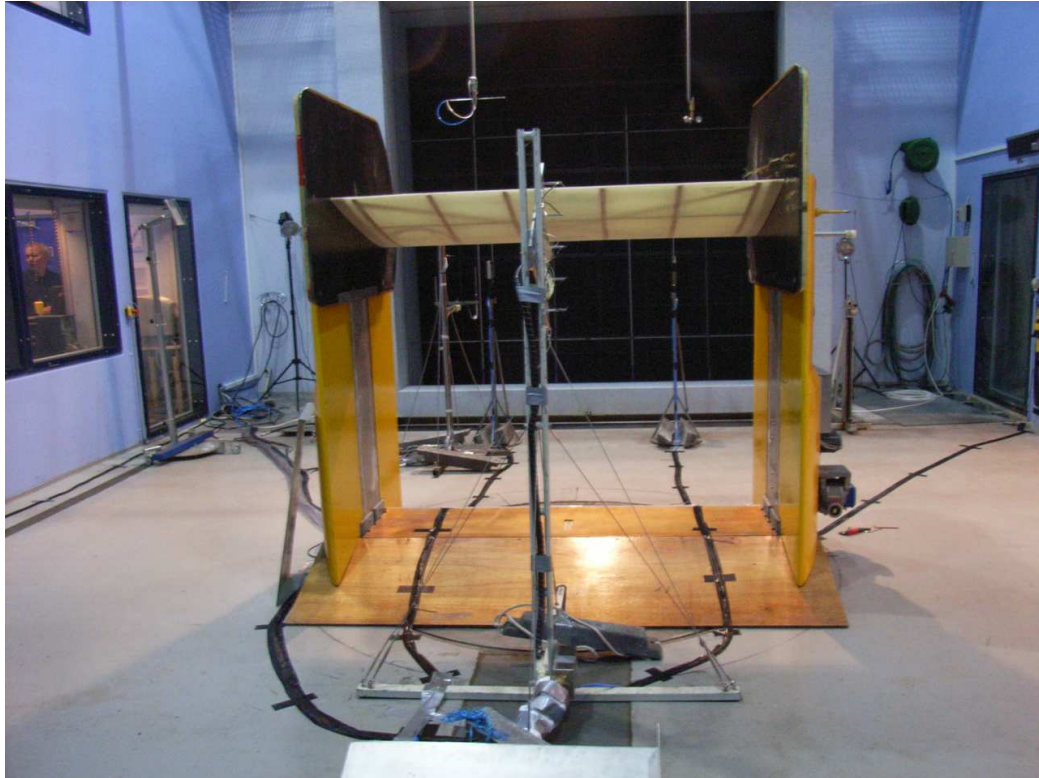
Figure 3.3: Picture of the stand in which the aerofoils were mounted. The picture is taken downstream of the aerofoil. The stand was identical in both experiments.
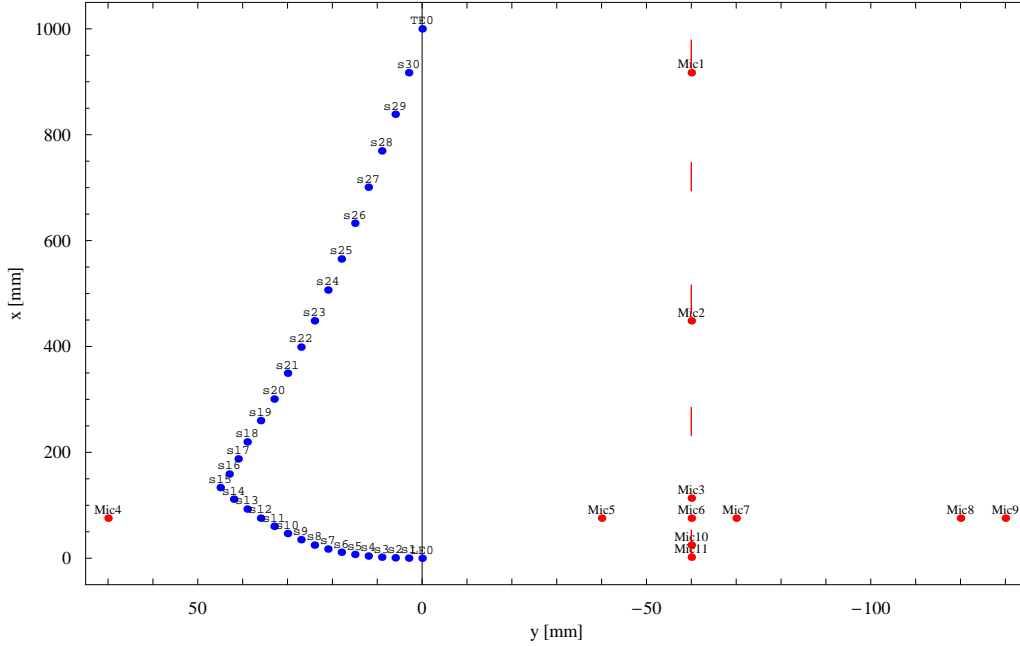
Figure 3.4: Position of microphones and pressure tabs relative to midspan of the aerofoil in the experiment with a NACA0015 profile. Blue dots are pressure tabs, and red dots are microphones. The microphone number refers to Table 3.1. The red, dashed line is the section shown in Figure 3.5.

aerofoil are a span of 1.90 m and a chord length of 1.00 m. This gives a Reynolds number of maximum $2.7 \cdot 10^6$ at 40 m/s. The NACA0015 profile with the above mentioned dimensions will have a lift curve that increases less due to separation at an AOA of approximately 12° at a mean flow speed of 25m/s (Abbott and von Doenhoff 1959). Further maximum lift occurs at an AOA of approximately 16° at 25m/s (Abbott and von Doenhoff 1959). One microphone was placed on the wall for reference, see Figure 3.6. The locations of the 11 microphones are sketched in Table 3.1 and Figures 3.4 and 3.5. The microphones were placed on the upper side (suction side) of the profile. The measurements of the microphones were mostly sampled at a frequency of 50 kHz in timeseries of 10 seconds. Run 3 was sampled at 5 kHz in timeseries of 120 seconds. The positions of the microphones were chosen to match the positions of microphones in a similar study by Mish and Devenport (2006). Because of the limited number of microphones in our campaign not all of the positions in Mish and Devenport (2006) are chosen.

The setup of instruments in the wind tunnel is given in Figure 3.6. The Figure shows the position of the reference microphone after Run 1 and the

x	y	z	no.	x	y	z	no.	x	y	z	no.
917.2	3.0	-15.6	p30	838.7	6.0	-27.1	p29	769.5	9.0	-36.5	p28
700.8	12.0	-45.0	p27	632.8	15.0	-52.9	p26	565.3	18.0	-60.0	p25
506.7	21.0	-65.2	p24	448.5	24.0	-69.4	p23	398.8	27.0	-72.3	p22
349.5	30.0	-74.2	p21	300.7	33.0	-74.8	p20	260.0	36.0	-74.4	p19
219.7	39.0	-72.9	p18	187.7	41.0	-70.6	p17	159.0	43.0	-67.7	p16
133.5	45.0	-64.6	p15	111.5	42.0	-60.8	p14	92.8	39.0	-56.9	p13
75.7	36.0	-52.7	p12	60.3	33.0	-48.1	p11	46.7	30.0	-43.1	p10
35.0	27.0	-37.9	p9	24.8	24.0	-32.5	p8	17.3	21.0	-27.5	p7
11.3	18.0	-22.5	p6	7.2	15.0	-18.1	p5	4.1	12.0	-13.8	p4
2.0	9.0	-9.6	p3	0.8	6.0	-6.0	p2	0.2	3.0	-3.1	p1
0.0	0.0	0.0	LE0	0.2	3.0	3.1	s1	0.8	6.0	6.0	s2
2.0	9.0	9.6	s3	4.1	12.0	13.8	s4	7.2	15.0	18.1	s5
11.3	18.0	22.5	s6	17.3	21.0	27.5	s7	24.8	24.0	32.5	s8
35.0	27.0	37.9	s9	46.7	30.0	43.1	s10	60.3	33.0	48.1	s11
75.7	36.0	52.7	s12	92.8	39.0	56.9	s13	111.5	42.0	60.8	s14
133.5	45.0	64.6	s15	159.0	43.0	67.7	s16	187.7	41.0	70.6	s17
219.7	39.0	72.9	s18	260.0	36.0	74.4	s19	300.7	33.0	74.8	s20
349.5	30.0	74.2	s21	398.8	27.0	72.3	s22	448.5	24.0	69.4	s23
506.7	21.0	65.2	s24	565.3	18.0	60.0	s25	632.8	15.0	52.9	s26
700.8	12.0	45.0	s27	769.5	9.0	36.5	s28	838.7	6.0	27.1	s29
917.2	3.0	15.6	s30	1000.0	0.0	00.	TE0				

Table 3.3: Positions of pressure tabs. Note the z-position denotes whether the instrument is on the pressure side (negative z) or on the suction side (positive z). All measures are mm. The x-coordinates are from the leading edge. See also Figure 3.4.
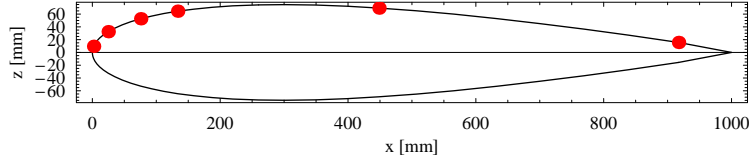
Figure 3.5: Sketch of the NACA0015 profile. The red dots are the positions of microphones. The positions of microphones are at the dashed line shown in Figure 3.4

approximate position of the reference microphone at Run 1 in the initial configuration.

The mean pressure were obtained by measurements with a known measurement technique, where 62 pressure tabs were placed on the profile as well. 30 were placed on the suction side and 30 on the pressure side. Furthermore, one was placed at the leading edge and one on the trailing edge. The positions of the pressure tabs can be seen in Figure 3.4 and Table 3.3. In the figure only the positions on the suction side and at the edges are shown. The pressure tabs on the pressure side are placed symmetrically in identical x- and z-positions (see Table 3.3). The pressure tabs measurements are generally sampled with a frequency of 100 Hz in time series of 30 seconds. Run 3 was sampled at 400 Hz in time series of $\sim$116 seconds. A triple wired hotwire was used as well, and the sample frequency is 10 kHz, except in Run 3 in which it was 5 kHz. The position of the hotwire stand is seen in Figure 3.6, and the instrumentation of the hotwire stand is seen in Figure 3.8.

The background noise was measured with a microphone during all runs. The characteristics of the runs are given in Table 3.4. The first run was primarily at different angle of attack and constant wind speed (25 m/s), and secondarily at different wind speed and an angle of attack of $-6.6°$, see Table 3.4. It was discovered that a bolt was not tightened at the first run, the bolt was then fixed. At the second run the microphone measuring the background was moved to obtain information on how the background pressure level was changing spatially in the test section. The measurements were at different wind speeds at three different angle of attacks, see Table 3.4. The angles are slightly different because they are free stream corrected. In the third run long time series (120 seconds) were obtained. The measurements were obtained at 25.4 m/s at different angles of attack, see Table 3.4.

The cut-off frequency of the device used in this experiment is by Eqn. (3.2) 3.4 kHz. The dimensions of the chamber according Figure 3.2 are given in Table 3.2.
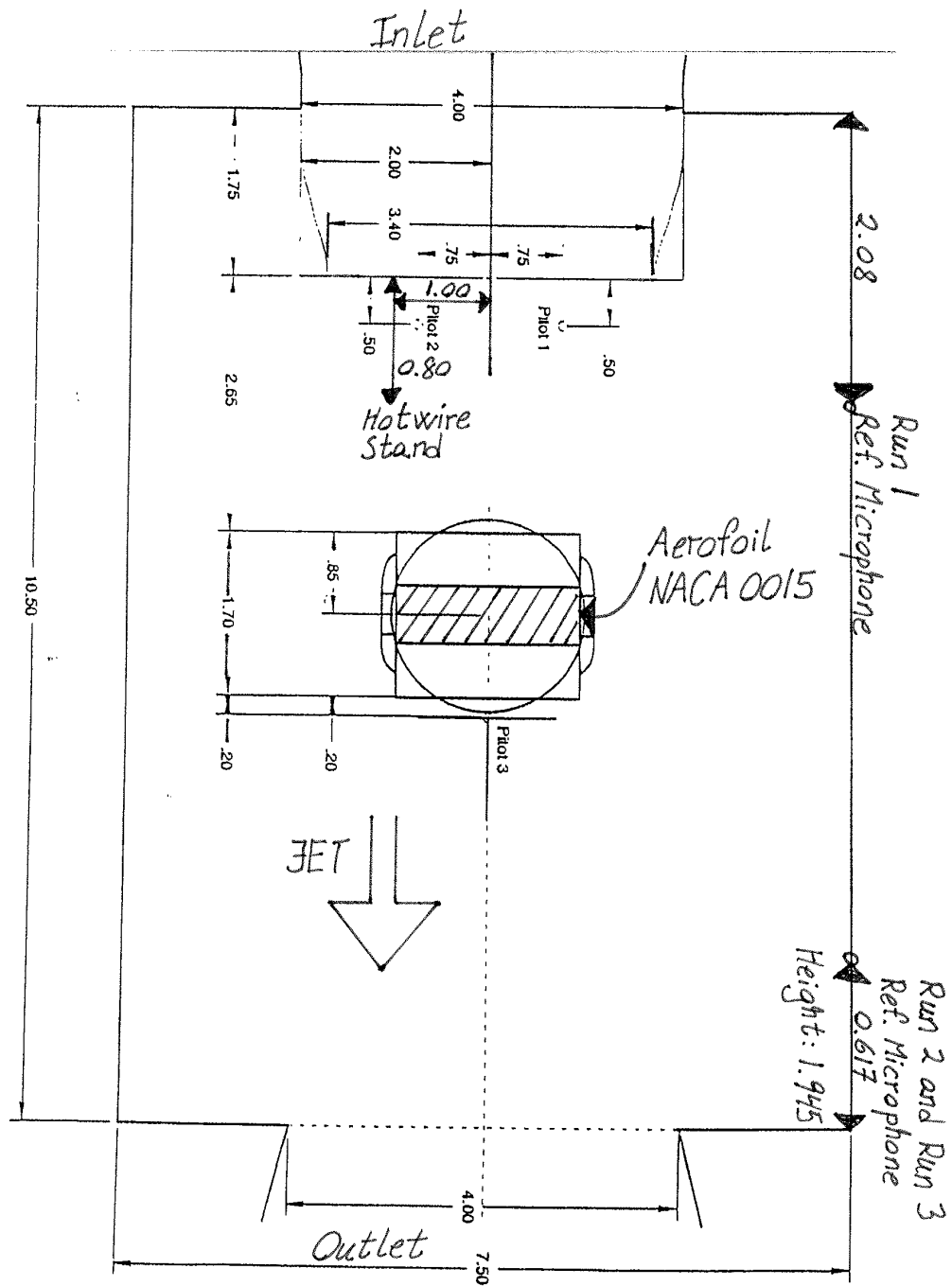
Figure 3.6: Location of instruments and aerofoil in Velux wind tunnel in the experiment with a NACA0015 profile. All measures are in meters. See also Figure 3.8 for a detailed description of the hotwire stand.
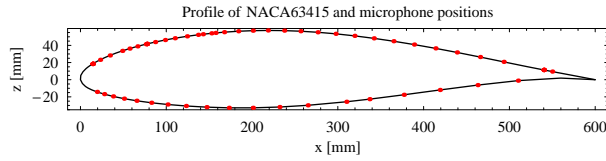
Figure 3.7: The shape of the NACA63415 profile. The positions of microphones are shown by the red dots.

Figure 3.8: Detailed diagram of the instrumentation of the hotwire stand. The jet is into the paper plane.
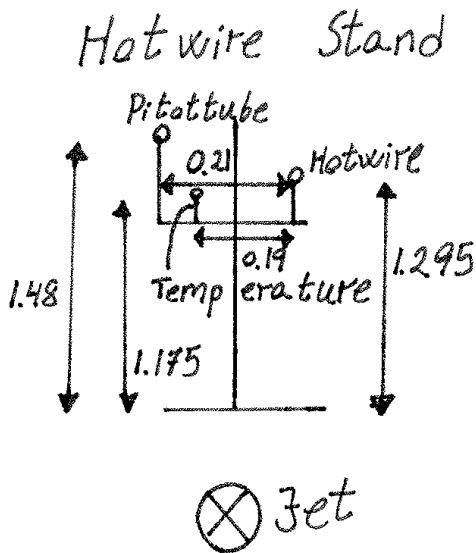
d_1	1.5mm
d_2	4.7mm
h_1	1.5mm
h_2	0.4mm
h_3	0.4mm
S_{cav}	$1.77 \cdot 10^{-6} \mathrm{m}^2$
L'_e	$2.78 \cdot 10^{-3} \mathrm{m}$
V_{cav}	$1.02 \cdot 10^{-8} \mathrm{m}^3$

Table 3.5: The dimensions of the chamber of the device in which the microphones are mounted in experiment 2 with a NACA63415 profile. See also Figure 3.2

Leg	Run 1		Run 2		Run 3	
	α_{cor} [°]	U [m/s]	α_{cor} [°]	U [m/s]	α_{cor} [°]	U [m/s]
1	-6.6	15	-5.8	15	-6.5	25.4
2	-6.6	21	-5.9	20	-3.2	25.4
3	-6.6	25	-6.3	25	-1.3	25.4
4	-3.3	25	-6.5	30	0.2	25.4
5	0.1	25	-6.6	35	1.9	25.4
6	3.3	25	-6.7	40	3.5	25.4
7	4.7	25	6.3	15	5.2	25.4
8	5.9	25	6.3	20	6.7	25.4
9	7.1	25	6.2	25	8.3	25.4
10	8.6	25	6.2	30	9.9	25.4
11	9.8	25	6.0	35	12.2	25.4
12	11.2	25	5.8	40	14.3	25.4
13			-0.2	15	16.7	25.4
14			-0.3	20	20.9	25.4
15			-0.4	25	24.7	25.4
16			-0.5	30	27.4	25.4
17			-0.7	35	30.0	25.4
18			-0.8	40		

Table 3.4: Characteristics of the experiment at Velux with NACA0015 profile. U is mean wind speed and α_{cor} is the estimated free-stream corrected angle of attack.

3.1.2   Setup of Experiment 2: NACA63415

Here 3 runs with data from microphones of the type Sennheiser KE-4-211-2 were obtained on a NACA63415 profile, see Figure 3.7. The three runs investigate the influence of different angles of attack (AOA) at a sampling frequency of 50kHz in 10s. The last of these was conducted with vortex generators mounted 0.03m from the leading edge in all span. Run 1 was sampled at a mean wind speed of 40 m/s and Run 2 and 3 at 30 m/s, see Table 3.8.

The aerofoil on which the microphones were mounted is a NACA63415 profile with a chord length of 0.6m and a span of 2m. This gives a Reynolds number of maximum $1.6 \cdot 10^6$ at 40 m/s, and zero lift is at an AOA of $-1.5°$. The lift curve increases less due to separation at an AOA of approximately 11° and attains a maximum lift at an AOA of approximately 15° at 30 m/s for the dimensions of the profile mentioned above (Abbott and von Doenhoff 1959). The profile of the aerofoil is shown in Figure 3.7. The microphones
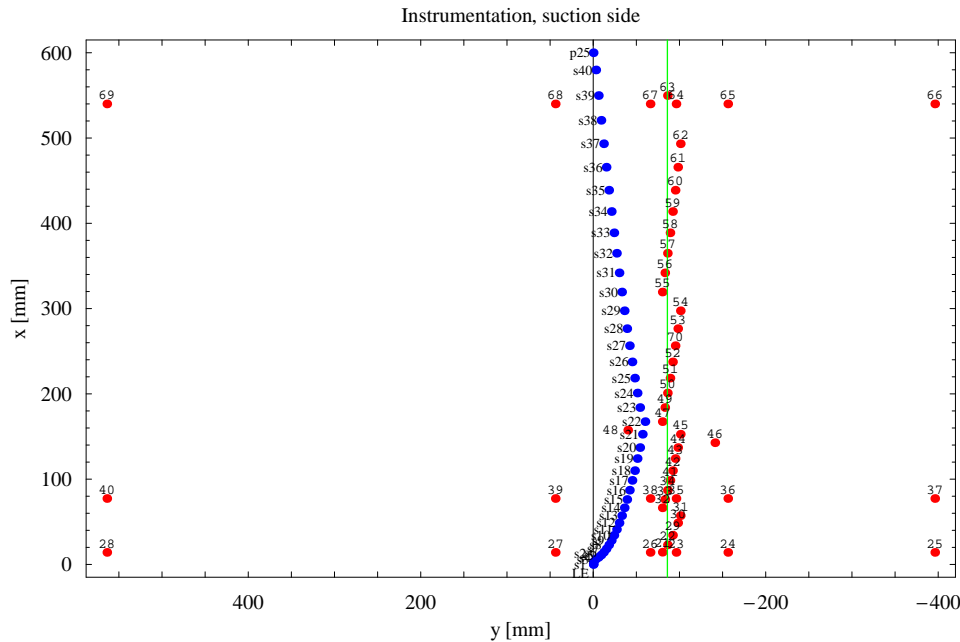
Figure 3.9: Positions of microphones and pressure tabs on suction side on the NACA63415 profile. Blue dots are pressure tabs, and red dots are microphones. The microphones on the green line are used in Section 4.2.2.

were placed in order to give both chordwise and spanwise information and were placed on both suction and pressure sides of the profile. The positions of the microphones on both sides can be seen in Table 3.7 and in Figures 3.9 and 3.10 which are a view of the aerofoil above the profile. The spanwise positions in Figures 3.9 and 3.10 are from the midpoint of the aerofoil and are positive to the right relative to the inflow. 69 microphones were placed on the aerofoil, and one microphone to obtain information about the general background level in the tunnel was placed on the wall (reference microphone), see Figure 3.11. Microphones no. 27 and no. 35 are malfunctioning, see Figure 3.9 and Table 3.7. In total, 66 pressure tabs were used as in the experiment with a NACA0015 profile. The positions of the pressure tabs are shown in Table 3.6 and in Figures 3.9 and 3.10.

The cut-off frequency of the microphone spectra is above 10 kHz in this experiment. The estimate of the cut-off frequency given by Eqn. (3.2) for the devices used in these measurements gives a frequency of 13.6 kHz by use of the dimensions given in Table 3.5. This estimate of the cutoff frequency is close to the observed frequency.

x	y	z	no.	x	y	z	no.	x	y	z	no.
600.0	0.0	0.0	p25	579.8	-3.0	3.8	s40	549.8	-6.0	9.5	s39
520.8	-9.0	15.2	s38	493.3	-12.0	20.8	s37	465.8	-15.0	26.4	s36
438.8	-18.0	31.8	s35	413.8	-21.0	36.5	s34	388.9	-24.0	41.0	s33
364.9	-27.0	44.9	s32	341.9	-30.0	48.2	s31	319.4	-33.0	51.1	s30
297.5	-36.0	53.5	s29	276.5	-39.0	55.3	s28	256.5	-42.0	56.5	s27
237.5	-45.0	57.2	s26	218.5	-48.0	57.4	s25	201.0	-51.0	57.2	s24
184.0	-54.0	56.5	s23	167.5	-60.0	55.4	s22	152.7	-57.0	54.1	s21
137.0	-54.0	52.3	s20	124.2	-51.0	50.6	s19	110.0	-48.0	48.3	s18
98.6	-45.0	46.2	s17	87.1	-42.0	43.9	s16	76.2	-39.0	41.4	s15
66.4	-36.0	38.9	s14	57.2	-33.0	36.3	s13	48.7	-30.0	33.6	s12
41.1	-27.0	30.9	s11	34.3	-24.0	28.3	s10	28.2	-21.0	25.7	s9
22.9	-18.0	23.2	s8	18.3	-15.0	20.8	s7	14.4	-12.0	18.5	s6
11.1	-9.0	16.4	s5	8.5	-6.0	14.6	s4	6.5	-3.0	12.9	s3
2.9	0.0	9.3	s2	0.3	0.0	5.0	s1	0.0	0.0	0.0	LE
2.3	0.0	-4.4	p1	5.6	0.0	-7.9	p2	8.7	-3.0	-9.7	p3
13.1	-6.0	-11.8	p4	19.3	-9.0	-14.2	p5	27.6	-12.0	-16.8	p6
38.0	-15.0	-19.4	p7	50.7	-18.0	-22.1	p8	65.4	-21.0	-24.6	p9
82.6	-24.0	-26.9	p10	101.6	-27.0	-28.9	p11	123.0	-30.0	-30.6	p12
147.0	-33.0	-32.0	p13	173.0	-36.0	-32.8	p14	201.0	-30.0	-32.8	p15
232.0	-27.0	-31.9	p16	265.0	-24.0	-29.9	p17	309.9	-21.0	-25.7	p18
336.9	-18.0	-22.7	p19	376.9	-15.0	-17.6	p20	418.9	-12.0	-12.0	p21
462.9	-9.0	-6.3	p22	510.0	-6.0	-1.1	p23	560.0	-3.0	1.9	p24

Table 3.6: Positions of pressure tabs on the NACA63415 profile. Note the z-position denotes whether the instrument is on the pressure side (negative z) or on the suction side (positive z). All measures are mm.

x	y	z	no.	x	y	z	Mic.no.	x	y	z	Mic.no.
549.8	-86.0	9.5	63	493.3	-101.0	20.8	62	465.8	-98.0	26.4	61
438.8	-95.0	31.8	60	413.8	-92.0	36.5	59	388.9	-89.0	41.0	58
364.9	-86.0	44.8	57	341.9	-83.0	48.2	56	319.4	-80.0	51.1	55
297.5	-101.0	53.5	54	276.5	-98.0	55.3	53	256.5	-95.0	56.5	70
237.5	-92.0	57.2	52	218.5	-89.0	57.4	51	201.0	-86.0	57.2	50
184.0	-83.0	56.5	49	167.5	-80.0	55.4	47	152.7	-101.0	54.1	45
137.0	-98.0	52.3	44	124.2	-95.0	50.6	43	110.0	-92.0	48.3	42
98.6	-89.0	46.2	41	87.1	-86.0	43.9	34	76.2	-83.0	41.4	33
66.4	-80.0	38.9	32	57.2	-101.0	36.3	31	48.7	-98.0	33.6	30
34.3	-92.0	28.3	29	22.9	-86.0	23.2	22	14.4	-80.0	18.5	21
14.1	-96.0	18.4	23	14.1	-156.0	18.4	24	14.1	-396.0	18.4	25
14.1	-66.0	18.4	26	14.1	44.0	18.4	27	14.1	564.0	18.4	28
77.3	-96.0	41.7	35	77.3	-156.0	41.7	36	77.3	-396.0	41.7	37
77.3	-66.0	41.7	38	77.3	44.0	41.7	39	77.3	564.0	41.7	40
540.0	-96.0	11.4	64	540.0	-156.0	11.4	65	540.0	-396.0	11.4	66
540.0	-66.0	11.4	67	540.0	44.0	11.4	68	540.0	564.0	11.4	69
157.5	-40.0	54.6	48	142.7	-141.0	53.0	46	19.3	-80.0	-14.2	2
27.6	-83.0	-16.8	3	38.0	-86.0	-19.4	4	50.7	-89.0	-22.1	5
65.4	-92.0	-24.6	6	82.6	-95.0	-26.9	7	101.6	-98.0	-28.9	8
123.0	-101.0	-30.6	9	147.0	-80.0	-32.0	10	173.0	-83.0	-32.8	11
201.0	-86.0	-32.8	12	232.0	-89.0	-31.9	13	265.0	-92.0	-29.9	14
309.9	-95.0	-25.7	15	336.9	-98.0	-22.7	16	376.9	-101.0	-17.6	17
418.9	-80.0	-12.0	18	462.9	-83.0	-6.3	19	510.0	-86.0	-1.1	20

Table 3.7: Positions of microphones on the NACA63415 profile. Note the z-position denotes whether the instrument is on the pressure side (negative z) or on the suction side (positive z). All measures are mm.
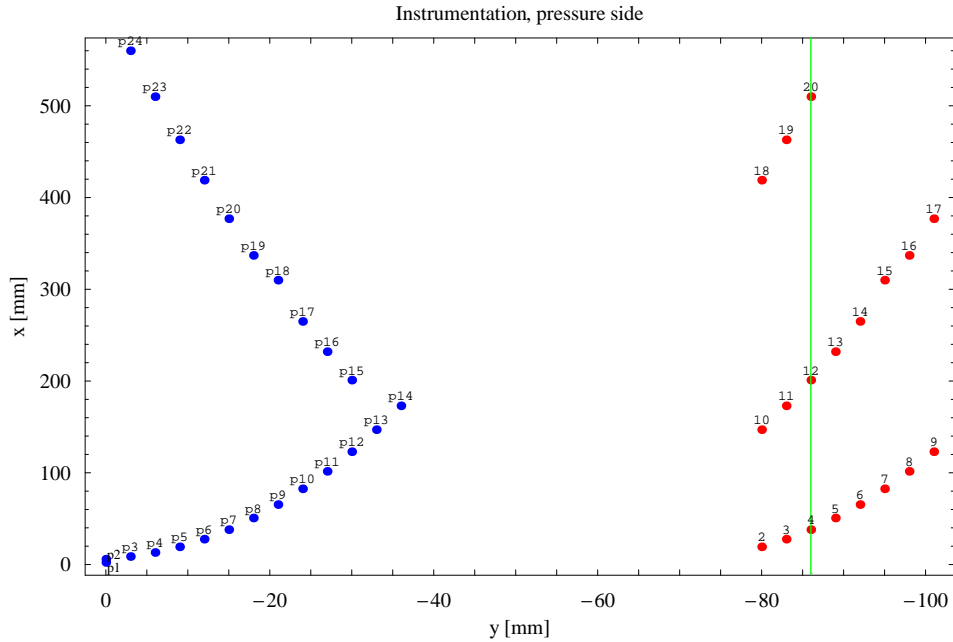
Figure 3.10: Positions of microphones and pressure tabs on pressure side seen from above (suction side) on the NACA63415 profile. Blue dots are pressure tabs, and red dots are microphones. The microphones on the green line are used in Section 4.2.2.

3.2 Results

The data for hotwire, microphone, 5-hole pitot tube, and pressure tabs measurements for the experiments carried out in Velux with a NACA0015 and a NACA63415 profile will be discussed below.

3.2.1 Experiment 1: NACA0015

Hotwire Data

By inspection of the calibrated data, it was discovered that the instrument might not have been aligned well enough with the free stream. The mean of the two velocity components supposed to be perpendicular to the direction of the free stream ($\langle V \rangle$, $\langle W \rangle$, where $\langle \rangle$ denotes mean) was not 0. Therefore the data in each timeseries were rotated, such that $\langle V \rangle = \langle W \rangle = 0$. The
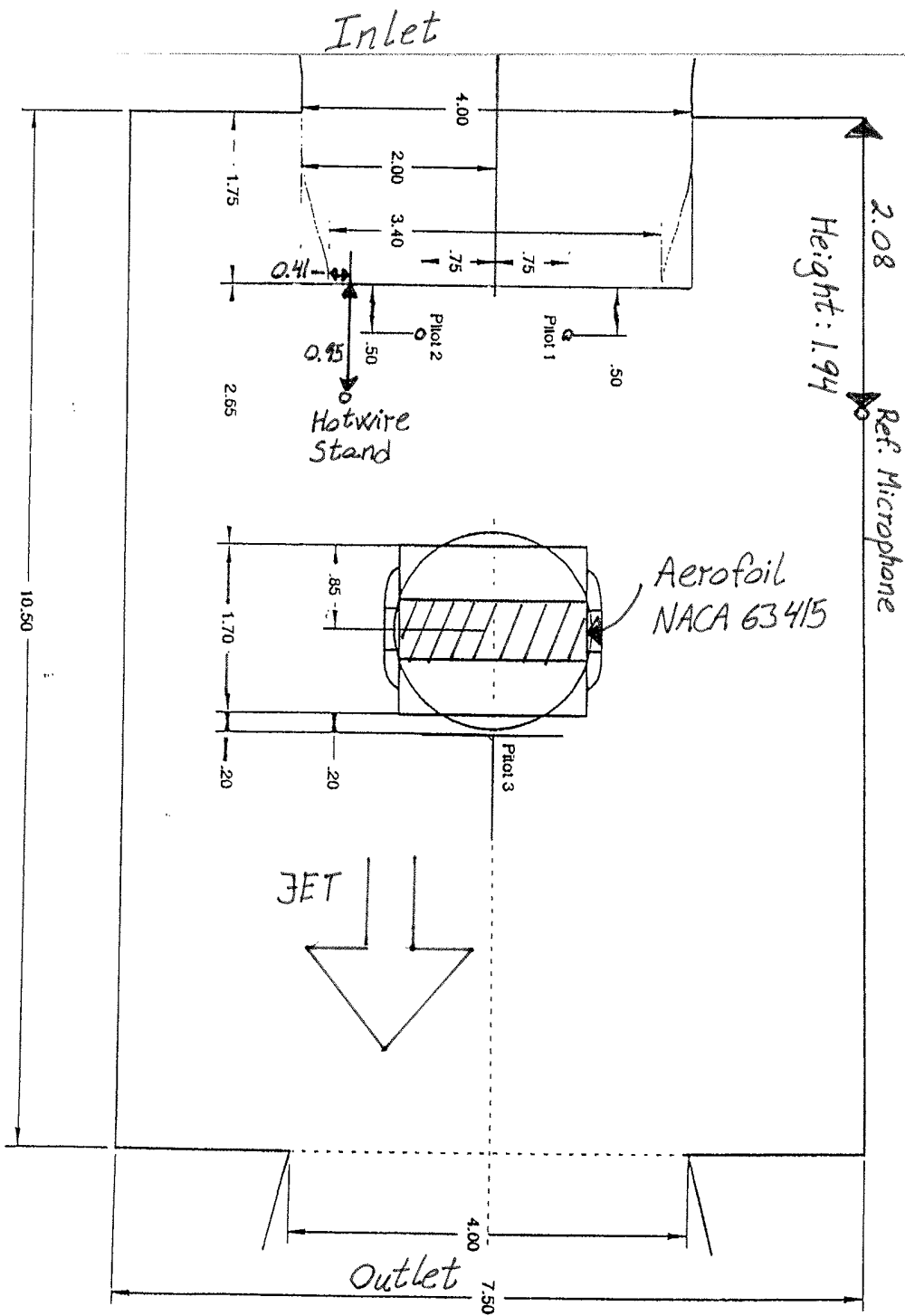
Figure 3.11: Location of instruments and aerofoil in the experiment with a NACA63415 profile. All measures are in meters. See also Figure 3.8 for a detailed description of the hotwire stand.

Leg	Run 1		Run 2		Run 3	
	α_{cor} [°]	U [m/s]	α_{cor} [°]	U [m/s]	α_{cor} [°]	U [m/s]
1	-10.6	40	-3.3	30	-3.4	30
2	-8.9	40	-1.6	30	-0.1	30
3	-7.3	40	0.1	30	3.3	30
4	-5.7	40	1.8	30	6.7	30
5	-3.9	40	3.4	30	10.2	30
6	-2.3	40	5.0	30	13.8	30
7	-0.6	40	6.8	30	15.9	30
8	1.0	40	8.5	30		
9	2.6	40	10.2	30		
10	4.3	40	12.0	30		
11	5.9	40	13.8	30		
12	7.6	40	16.0	30		
13	9.2	40				
14	11.0	40				
15	13.0	40				

Table 3.8: Characteristics of experiments at the experiment for a NACA63415 profile. U is mean wind speed and α_{cor} is the free-stream corrected angle of attack estimated.

transformation is given by

$$R = \begin{bmatrix} \frac{U}{|\overline{U}|} & \frac{V}{|\overline{U}|} & \frac{W}{|\overline{U}|} \\ \frac{-V}{|\boldsymbol{n}\times\overline{U}|} & \frac{-U}{|\boldsymbol{n}\times\overline{U}|} & 0 \\ \frac{-UW}{|\overline{U}||\boldsymbol{n}\times\overline{U}|} & \frac{-VW}{|\overline{U}||\boldsymbol{n}\times\overline{U}|} & \frac{|\boldsymbol{n}\times\overline{U}|}{|\overline{U}|} \end{bmatrix} \begin{bmatrix} U(t) \\ V(t) \\ W(t) \end{bmatrix} \tag{3.3}$$

according to Nielsen (1998). $\overline{U} = \{U, V, W\}$ in Eqn. (3.3) is the mean velocities of the timeseries. The normal vector $\boldsymbol{n} = \{0, 0, 1\}$ points in the vertical direction, thus assuming that the hotwire device is perfectly vertical. The vector $\{U(t), V(t), W(t)\}$ is the single datapoint in the timeseries at the time of measurement, t.

The angle of rotation of the alignment at each measurement is shown in Table 3.9. Isotropic turbulence in the inertial subrange is characterized by Mann (1994a)

$$\frac{4}{3}S_U(k) = S_V(k) = S_W(k) \tag{3.4}$$

The above criterium is plotted in Figure 3.12 for two selected samples. If the plots are on top of each other the turbulence is perfectly isotropic in the

Leg	Run 1	Run 2	Run 3
1	1.33	1.18	0.85
2	1.01	0.86	1.15
3	0.88	1.42	1.33
4	0.84	1.24	1.45
5	1.10	1.32	1.56
6	0.95	1.57	1.55
7	0.78	1.26	1.64
8	0.93	1.48	1.63
9	0.95	1.62	1.64
10	0.92	1.60	1.67
11	1.24	1.46	1.74
12	0.98	2.01	1.75
13		1.98	1.75
14		2.30	1.83
15		2.21	2.00
16		2.03	1.99
17		2.04	2.10
18		2.85	

Table 3.9: Angle of rotation [°] of hotwire data.

inertial subrange (Mann 1994a). The spectra seem not to be in the inertial subrange except at the highest frequencies, where the $\frac{4}{3}$ ratio of $S_U(k)$ seems to be satisfied. The lines for the spectra of the three velocity components $(\frac{4}{3}S_U(k)$, $S_V(k)$, $S_W(k))$ in Figure 3.12 are almost on top of each other for wave numbers above approximately 100. The turbulence seem in general not to be isotropic in all scales.

The turbulence intensity, $I = \frac{\sqrt{\sigma_{var}^2}}{U}$, in Table 3.10 shows, that the turbulence is not perfectly isotropic. It is seen in Table 3.10 that the velocity fluctuations in the direction of the mean wind, $\frac{\sqrt{\sigma_U^2}}{U}$, has lower values in most cases than the two other velocity components. It is common in atmospheric flow that the turbulence intensity in the direction of the mean wind have a higher value than the turbulence intensity in the other two directions (Mann 1994b). Thus the turbulence intensity in Table 3.10 cannot be compared to atmospheric conditions.

Test of isotropic turb. at angle 9.8 at Run 1

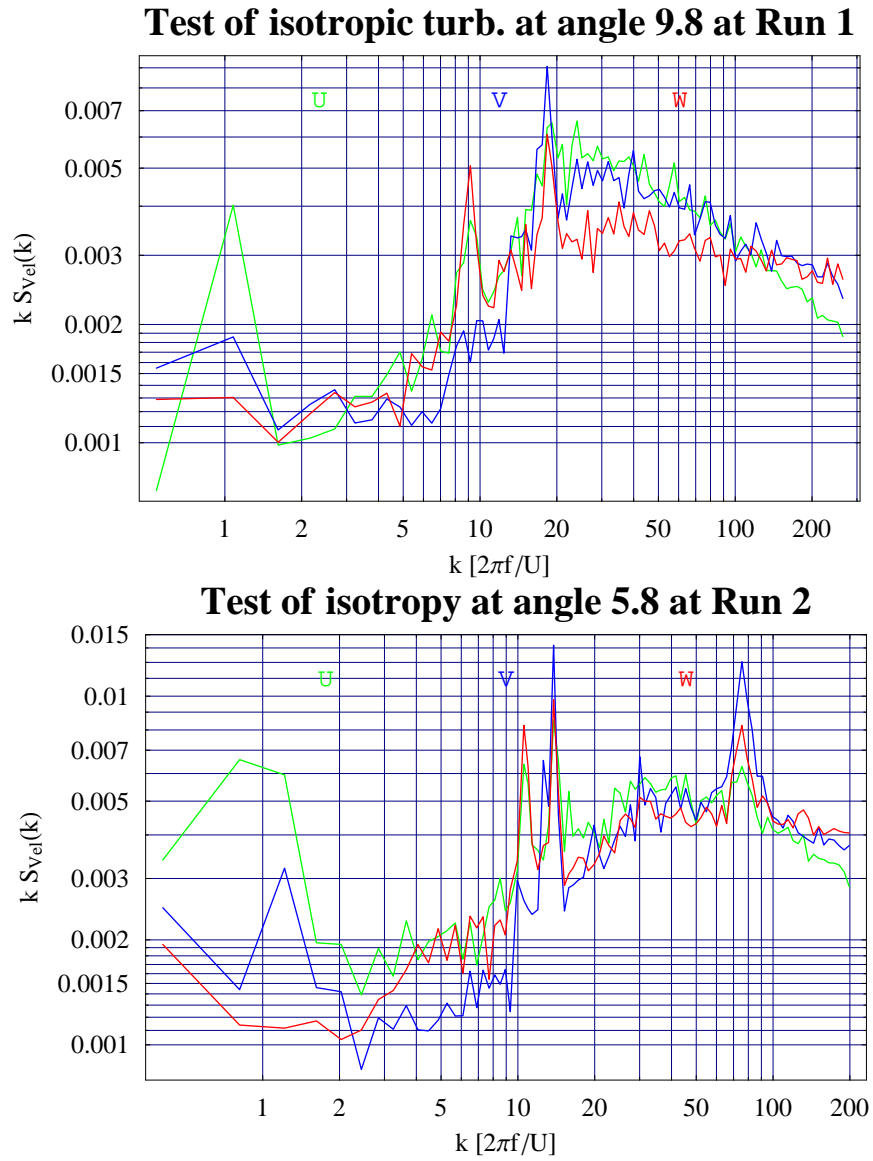**Test of isotropy at angle 5.8 at Run 2**

Figure 3.12: Spectra of velocity components at isotropic scaling according to Eqn. (3.4). The top plot is for a mean flow of 25.4m/s at Run 1, Leg 11 and the bottom plot is for 40m/s at Run 2, Leg 12.

Leg	Run 1			Run 2			Run 3		
	$\frac{\sqrt{\sigma_U^2}}{U}$	$\frac{\sqrt{\sigma_V^2}}{U}$	$\frac{\sqrt{\sigma_W^2}}{U}$	$\frac{\sqrt{\sigma_U^2}}{U}$	$\frac{\sqrt{\sigma_V^2}}{U}$	$\frac{\sqrt{\sigma_W^2}}{U}$	$\frac{\sqrt{\sigma_U^2}}{U}$	$\frac{\sqrt{\sigma_V^2}}{U}$	$\frac{\sqrt{\sigma_W^2}}{U}$
1	0.007	0.010	0.010	0.007	0.012	0.011	0.007	0.008	0.007
2	0.008	0.010	0.010	0.009	0.011	0.010	0.007	0.009	0.007
3	0.010	0.011	0.010	0.011	0.010	0.010	0.006	0.009	0.007
4	0.010	0.011	0.010	0.009	0.014	0.013	0.006	0.009	0.007
5	0.010	0.012	0.011	0.008	0.016	0.013	0.006	0.009	0.007
6	0.008	0.012	0.011	0.010	0.020	0.016	0.005	0.008	0.007
7	0.008	0.010	0.010	0.008	0.010	0.012	0.005	0.008	0.007
8	0.008	0.011	0.012	0.008	0.011	0.012	0.005	0.008	0.007
9	0.008	0.010	0.011	0.009	0.012	0.012	0.005	0.008	0.007
10	0.007	0.010	0.011	0.009	0.017	0.015	0.005	0.008	0.007
11	0.008	0.012	0.012	0.008	0.016	0.014	0.004	0.008	0.007
12	0.007	0.010	0.010	0.010	0.024	0.019	0.005	0.008	0.007
13				0.007	0.008	0.010	0.005	0.008	0.007
14				0.008	0.011	0.012	0.005	0.008	0.007
15				0.010	0.012	0.012	0.005	0.008	0.007
16				0.009	0.017	0.016	0.005	0.008	0.007
17				0.009	0.017	0.016	0.005	0.008	0.007
18				0.011	0.022	0.021			

Table 3.10: Turbulence intensity of hotwire data.

Microphone Data

The background microphones were used to get a general picture of the pressure fluctuations in the tunnel that were not influenced by aerodynamics. Figure 3.13 shows some peaks in the spectra that are not of aerodynamical origin. This is confirmed because the spectra from the background microphone are independent of AOA. The peaks are thus related to the characteristics of the wind tunnel. These peaks will also be present in the pressure spectra for the microphones located on the aerofoil, and the peaks should therefore be ignored in the spectra from those microphones. Acoustical phenomena in the wind tunnel such as fan tones, room resonance, edge tones and etc. are not considered because the aim of the pressure data is to obtain information of the aerodynamical pressure and not acoustical pressure. The tunnel is unfortunately not anechoic. The background microphone can only be used qualitatively because the signal depends on position in space.

Eqn. (2.103) is employed to compare the spectra at different mean velocities. The Eqn. (2.103) is derived under the conditions of an inviscid flow
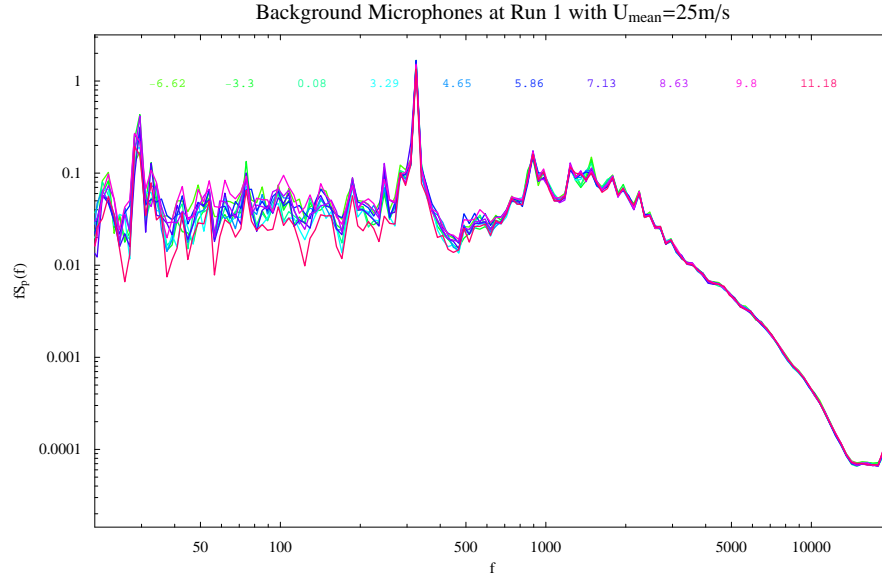
Figure 3.13: Pressure spectra of background microphone at Run 1 of the legs 3 to 17 according to Table 3.4

field, hence viscous effects are ignored. Thus, pressure spectra, $S_P(f)$, at different mean velocities normalized with U^4/c^4 should be on top of each other, when plotted against fc/U. The chord length is as previously denoted c.

The measurements in run 2 are for different mean velocities. Thus they are suitable to investigate the dependence of the pressure fluctuations on Reynolds number of different AOA's. The slope of the spectra in Figures 3.14 to 3.16 is in the range of reduced frequency (fc/U) of 2 to 20 nearly constant. The figures show the scaled spectra at three different AOA's at three positions on the aerofoil. Figures 3.14 and 3.15 are close to the leading edge and Figure 3.16 is at mid-chord. The flow is independent of Reynolds number when the scaled spectra at different mean velocities collapse when plotted as function of reduced frequency. It is seen that the pressure fluctuations are independent of Reynolds number for an AOA of -6.31° in Figures 3.14 and 3.15. The microphones are in this case on the pressure side of the aerofoil and thus do not experience a high speed up as can also be seen in Figure 2.3. The third microphone (Mic 2) near midchord in Figure 3.16 for an AOA of -6.31° shows a dependence on Reynolds number which is caused by transition from laminar to turbulent flow in the boundary layer of the aerofoil. The flow is dependent on Reynolds number for the AOA's -0.46° and 6.13° for all three microphones. The Reynolds dependence is not as pronounced for
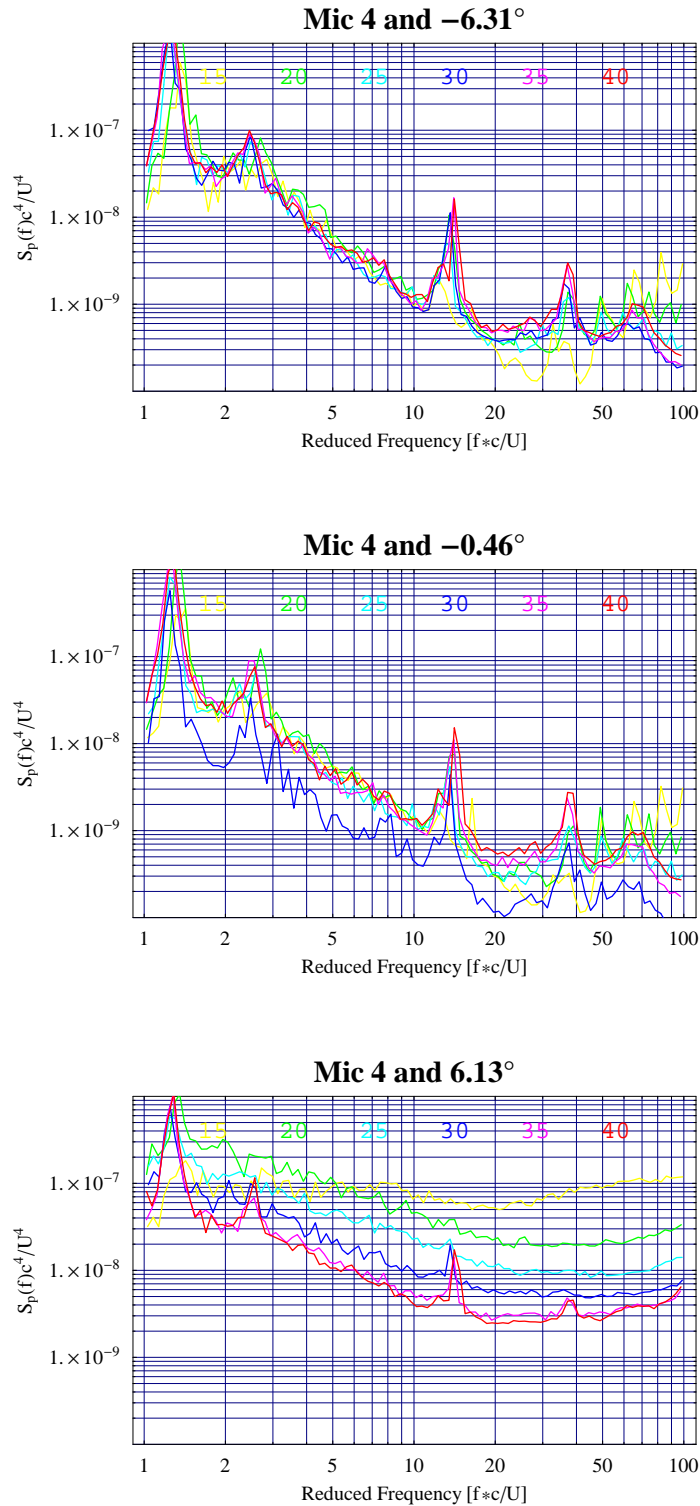
Figure 3.14: Scaling according to Eqn. (2.103) at microphone 4 (7.6% chord). The colours in the plot indicate the wind speed given in the top of the plot. The top plot is Leg 1 to 6 in Table 3.4. Leg 13 to 18 is the mid plot, and the bottom plot is Leg 7 to 12. The AOA given for each plot is a mean because the AOA is changing with wind speed according to the discussion in Section 3.1
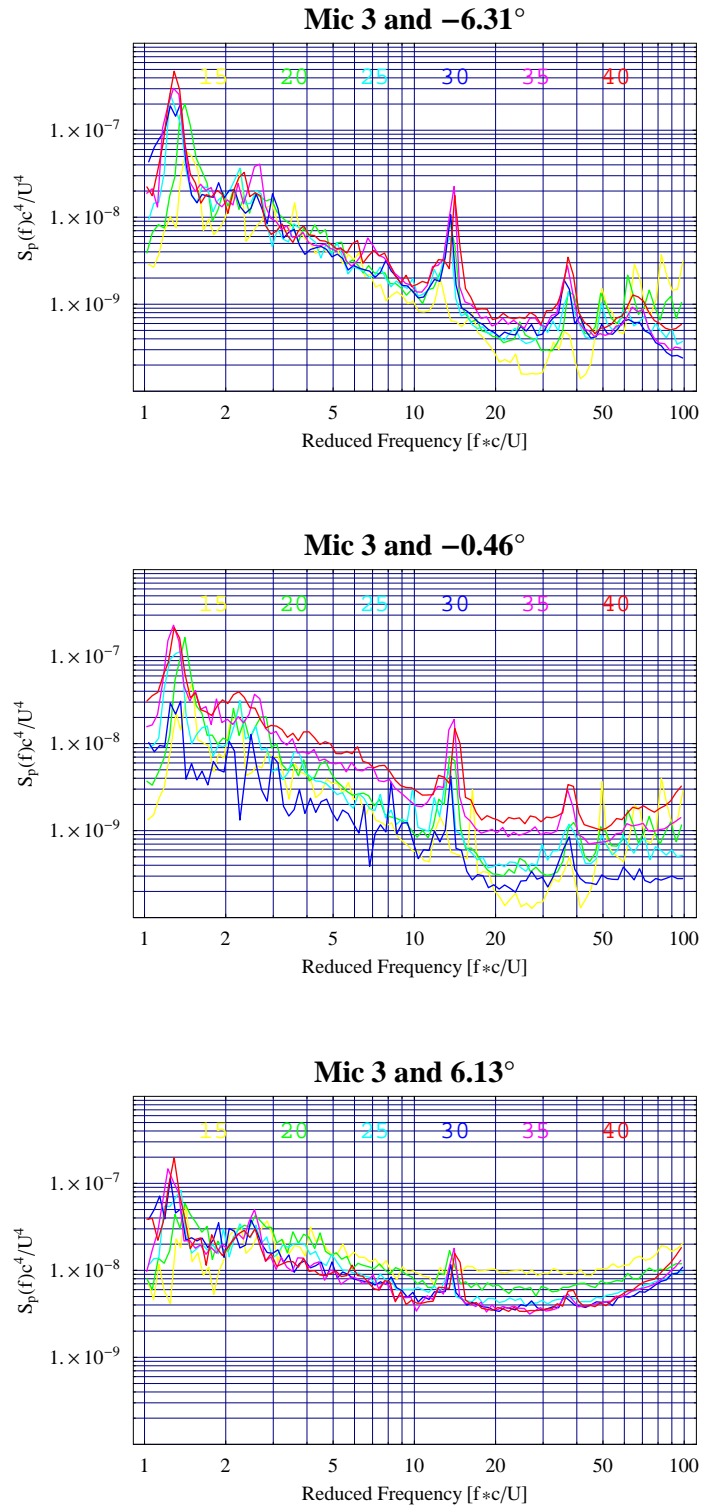
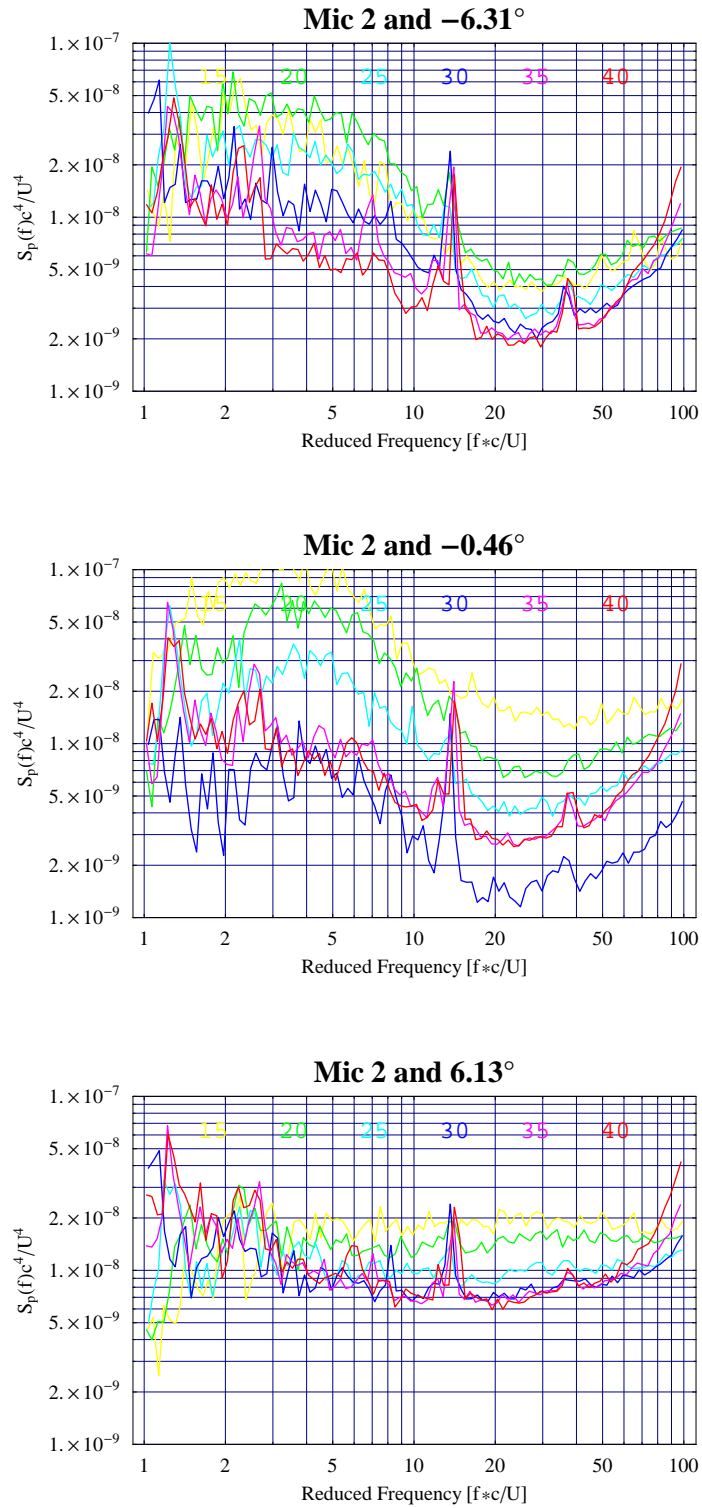Figure 3.15: Same as for Figure 3.14 for microphone 3 (11.4% chord).

Figure 3.16: Same as for Figure 3.14 for microphone 2 (44.9% chord).

the microphone closest to the leading edge at an AOA 0.46° as for other five cases, though.

The pressure fluctuations are from theory seen to have the highest amplitude at the leading edge and decrease towards the trailing edge. This is indicated in Figures 3.14 to 3.16 as well, although a transition from laminar to turbulent flow has occurred. This suggests that it is reasonable to use the pressure fluctuations obtained by microphones to estimate the lift fluctuations at low AOA's.

Figure 3.17 shows the pressure spectra without scaling for similar positions as Figures 3.14 to 3.16.

Pressure Tabs Data

The pressure hole data are used to estimate corrected AOA's from the mean values of these pressure data. The pressure hole data are by experience reliable in the mean values to estimate AOA's (Gaunaa et al. 2004). The values of estimated corrected AOA's are seen in Table 3.4.

5-Hole Pitot Tube Data

The data are used to estimate mean wind speed data. The tubes attached to the pitot tubes were quite long and this means that the highest frequency that can be resolved is below 10Hz. The pressure data are converted into velocities by Bernoulli's theorem (Eqn. (2.11)). Figure 3.18 shows a comparison of hot wire data against velocities calculated from the 5-hole pitot tubes. It shows that velocity spectra of the 5-hole pitot tube are diverging from the hot wire at around 3Hz and are below the hot wire spectra for higher frequencies.

The mean velocities in Table 3.4 are from the 5-hole pitot tube data. The mean velocities obtained from the 5-hole pitot tube data are believed to be reliable because they have similar values as a cup anemometer installed in the wind tunnel.

3.2.2   Experiment 2: NACA63415

In this experiment with a NACA 63415 profile no hotwire or 5-hole pitot tube data are available. Thus only pressure data from microphones and pressure tabs will be discussed below.
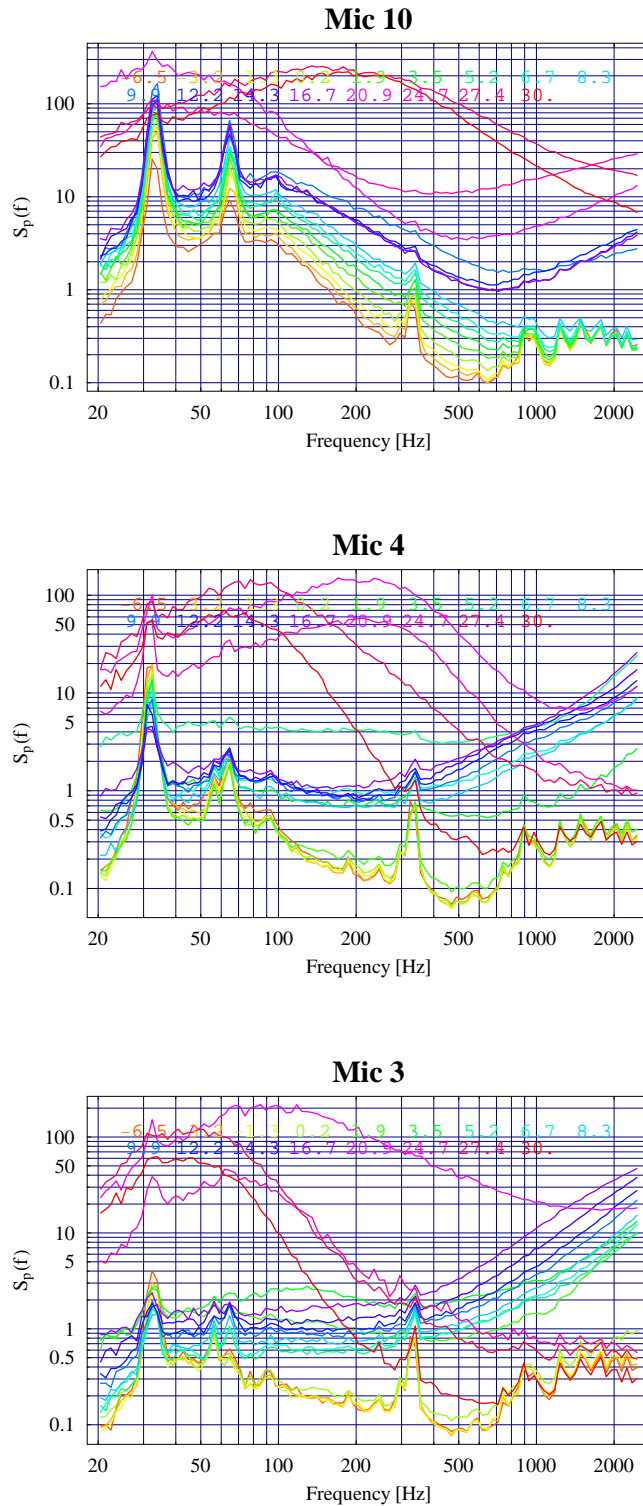
Mic 10

Mic 4

Mic 3

Figure 3.17: Spectra of pressure for different AOA's at three different microphones. Microphone 10 is at 2.5% chord, microphone 4 is at 7.6% chord, and microphone 3 is at 11.4% chord. The colours indicate AOA as given in the top of each plot.
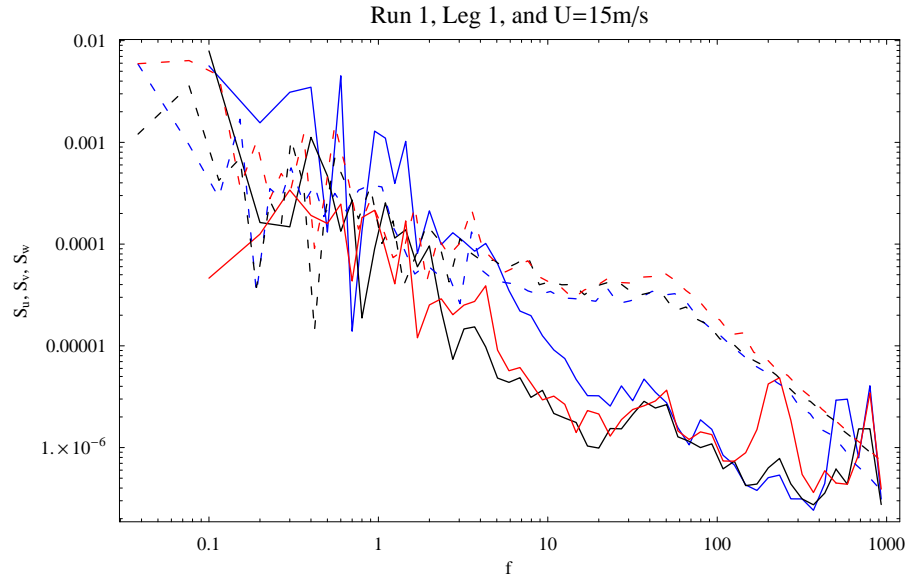
Figure 3.18: Comparison of velocity spectra from 5-hole pitot tube and hotwire. The dashed lines are hot wire data and full lines are calculated 5-hole pitot tube data. Blue is u, red is v, and black is w in both cases.

Microphone Data

The transition and separation is also recognizable when the standard deviation, σ_p, of the pressure is plotted as function of chordwise position and AOA, see Figure 3.19. The standard deviation is found according to Eqn. (2.107) because the information of transition is found in the frequency range of 100 Hz to 5 kHz. Outside this frequency range the spectral information contains a lot of noise that is believed to be due to the wind tunnel in the lower frequencies and the mounting of the microphones in the higher frequencies. The plot in Figure 3.19 is to be understood qualitatively because peak values indicate either transition or turbulent transition depending on AOA and chordwise position. The lesson learned from spectra of pressure (both scaled and ordinary) in the experiment with a NACA0015 profile is that σ_p will increase as transition is reached because high frequencies contain nearly as much energy as low frequencies. Then σ_p decreases a little when looking both in the direction of constant AOA and increasing chordwise position and vice versa because low frequencies now contain less energy than at laminar flow. Turbulent transition occurs when the standard deviation again is increasing in both directions because the energy level at this stage is much higher in all frequencies than at laminar flow.

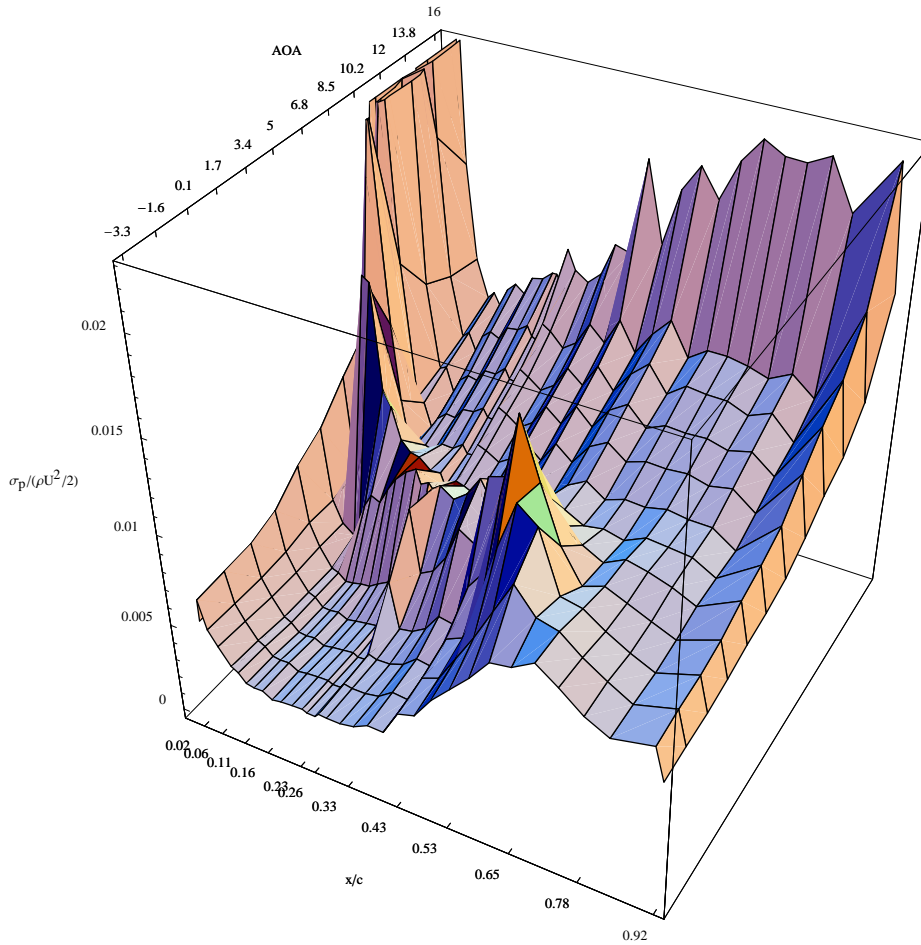Figure 3.19 shows the standard deviation for Run 3 in Table 3.8. The

Figure 3.19: The standard deviation, σ_p, of the pressure normalized with the dynamic pressure. AOA is the angle of attack and x/c is the normalized chordwise position. The angles are given in Table 3.8 for Run 2. The chordwise positions is for the microphones in Figure 3.9 with a spanwise position between 50mm and 100mm, see also Table 3.7.

"mountain ridge" at low AOA's show the transition position as function of AOA and position. Turbulent transition is not as recognizable but is present at the highest AOA and starts at 33.5 % chord. This is also seen in Figure 3.20, where the highest AOA contains most energy in all frequencies compared to lower AOA's. Likewise as discussed above the transition is recognized as well in Figure 3.20. Transition is present at AOA 3.4° and 5.0° and turbulent transition is present at 16.0° , which is also in agreement
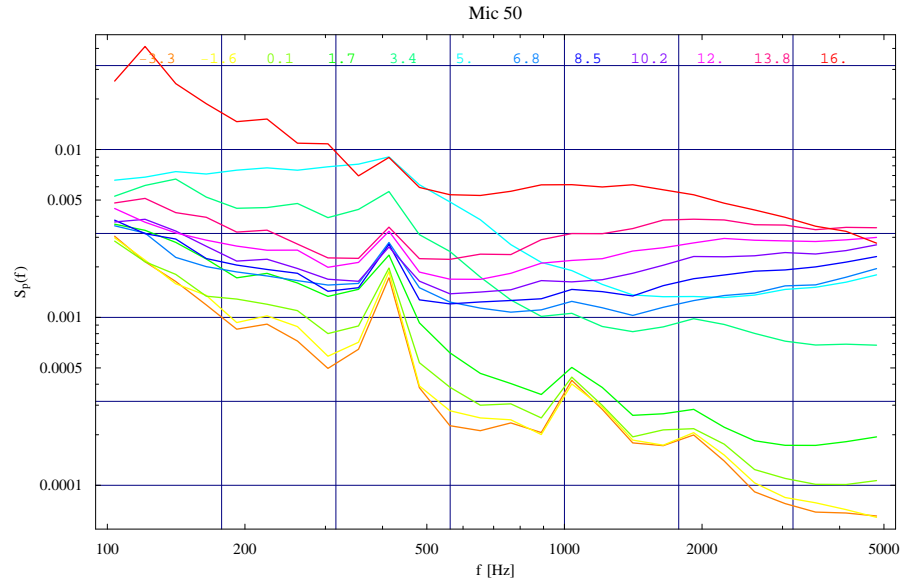
Figure 3.20: Spectra of pressure for different AOA's at microphone 50 (33.5% chord). Colours indicate AOA as given in top of plot.

with Figure 3.19.

Pressure Tabs Data

The pressure data from pressure tabs are used for estimating AOA's. The arguments for this are the same as at page 78. The estimated corrected AOA's are seen in Table 3.8.

3.3   Data from Bridge Deck Simulation

These data are described in Larose (1997), Larose and Mann (1998), and Larose (2003). The pressure data are obtained from pressure tabs on a section model of the bridge build over the Great Belt in Denmark between Zealand and Funen. They are placed on both the upper and lower side of the section model. The pressure data are used to calculate the admittance and coherence of the lift fluctuations due to atmospheric turbulence. The turbulence is generated by three different grids and the flow was measured with hotwire anemometry.

Pressure tabs were mounted on the surface of the bridge model to measure the surface pressure. The pressure tabs were mounted in different strips or sections of the bridge model and had at least 32 pressure tabs in each strip.
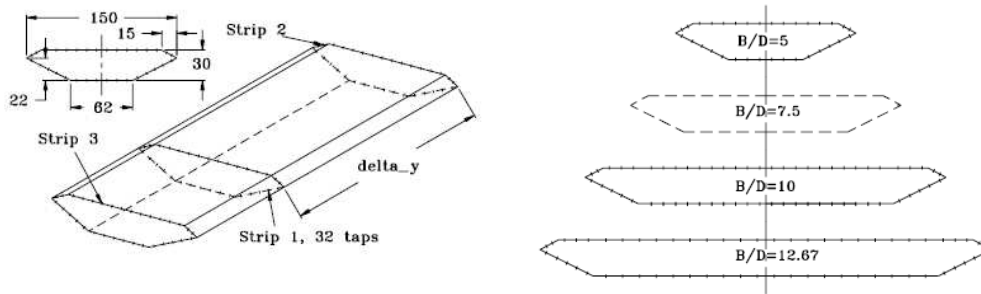
Figure 3.21: Sketch of the model of a bridge deck which is used in Larose (1997) on the left. The different sections that are tested are on the right. The sketches are the Figures 3 and 4 on p. 54 in Larose (1997).

The frequency response was trusted up to 100 Hz, Larose (1997).

The lift fluctuations are obtained by discrete numerical integration (summation) because the pressure is known at discrete positions only. The numerical integration which is used to find the lift in Larose (1997) is similar to Eqn. (4.12).

The Reynolds number of the experiment was between $2.3 \cdot 10^5$ and $5.7 \cdot 10^5$ with a mean flow speed of 15m/s and width of the section, B, between 0.15m and 0.38m, see Figure 3.21. The quantity, B/D, is used in Larose and Mann (1998), see Figure 3.21, where D is the thickness of the bridge section and given to be 0.03m. The section was 2.55m long. The turbulence length scale, L, common for all three components was obtained from hotwire data. The length scale of the w-component of the turbulence was obtained from L as $\mathcal{L}_w = 0.561L$ according to Eqn. (20), p. 107 in Larose (1997), see also Table 8 in Larose (1997), p. 107.

The data described in this Section are included in this thesis because they are used to validate the theory by Graham (1970) on yet another data set in another application.

3.4   Conclusions Regarding Experiments

Two experiments conducted in a wind tunnel are described. The experiments were on a NACA0015 profile and a NACA63415 profile. The first profile is symmetric and has no camber and the other has camber.

Surface pressure data from two systems were obtained, by microphones and by pressure tabs in both experiments. The data from microphones are

suitable for analyzing lift fluctuations and lift distribution fluctuations. The data from pressure tabs is not suitable for fluctuations of pressure but give reliable mean pressures. The mean pressure is used to estimate the angle of attack to mean flow of the profile. The positioning of microphones and pressure tabs are illustrated for both experiments.

The measurements by microphones can be used to investigate the positions of transition and turbulent transition of the flow over the chosen aerofoils in the angle of attack and chord wise position space. They capture the fluctuations in a way that they are trusted to give reliable information in the frequency domain when Fourier analyzed.

Data of the flow were obtained by a 5-hole pitot tube and a triple wired hot wire. The data from the 5-hole pitot tube is suitable to describe the mean flow. The hot wire data are used to obtain information of the turbulence in flow. The turbulence intensity is between 1 and 2% and the turbulence is close to be isotropic. The hotwire and the 5-hole pitot tube are both placed upstream of the profile.

The data from the two wind tunnels experiments are of a quality such they can be used for further analysis. The pressure spectra from microphones show peaks that are ignored because they are characteristic for the wind tunnel.

Data from a bridge deck simulation is shortly described. They are pressure and turbulence data and are given in Larose (1997), Larose and Mann (1998), and Larose (2003).

Chapter 4

Comparison of Models and Experiments

This chapter discusses the properties of the models and their numerical treatment. Further the models are tested against data. The statistical measures are pressure spectrum at a point, the lift spectrum, and the sound pressure level (SPL). The models are introduced in Chapter 2. The data are introduced in Chapter 3.

The assumptions and adjustments made to the models in order to obtain the statistical measures and the assumptions about the data will be discussed. The data used to calculate spectra of pressure and lift are based on measurements obtained from microphones.

4.1 Numerical Treatments

The models have certain limitations. They are defined for all wave numbers but they may not give reasonable results outside a certain range of wave numbers and they have to be treated with care when integrated to obtain spectra. Data are obtained at discrete points in a limited time interval. This gives rise to considerations on how to treat data. These issues are discussed in this section.

Spectra of pressure or lift fluctuations are obtained differently for models and data. Spectra from models are obtained in the wave number regime, and spectra from data are obtained in the frequency regime. The property, Eqn. (2.98), is used in order to compare the two regimes. The plots in the sections for pressure and lift fluctuations are given with two vertical lines at 10Hz and 20Hz shown cyan and magenta, respectively. The reason for this is that the frequency response of the microphones has a lower limit of 10 Hz.
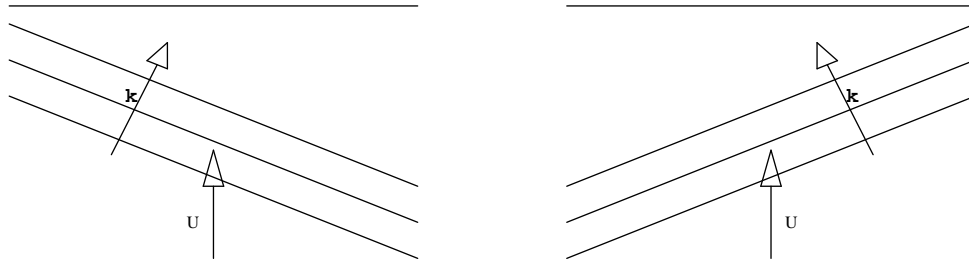
Figure 4.1: Illustration of a skewed gust and its mirror image. The figure on the left shows a gust with given chordwise wave number and spanwise wave number. The figure on the right shows a gust with the identical wave number in the chordwise direction but the spanwise wave number is of opposite sign. The chord wise wave number is given and the spanwise is defined positive at the left plot and negative at the right plot. The plots illustrates the gust given in Eqn. (4.1).

Further the microphone frequency response is constant between 20 Hz and 20 kHz.

4.1.1   Numerical Treatment of Models

Some assumptions must be made in order to find the spectra of lift and pressure as well to estimate the SPL. Some of the assumptions are similar for all three models and some are individual. Furthermore some numerical issues have to be solved. Some of these are common to all three models and some are individual as well.

Double-sided turbulence spectra imply that the transfer function models are assumed symmetric in the wave number space for the models that are expressed in two variables. The energy spectrum of the turbulence is symmetric in either wave number and this implies that if the transfer functions are symmetric in either wave number then the integrand in Eqns. (2.96) or (2.97) is symmetric as well and the integration are over 0 to ∞. The transfer function models do not give numerically reasonable results when one of the wave numbers or both are negative. The numerical condition that is used for the transfer functions of lift distribution and lift can be expressed in mathematical terms by

$$|g((x,)k_x, k_2)| = |g((x,)k_x, -k_2)| \tag{4.1}$$

where $g((x,)k_x, k_2)$ is any of the transfer functions in two variable wave numbers for either lift distribution (pressure spectra and SPL) or lift (lift spec-
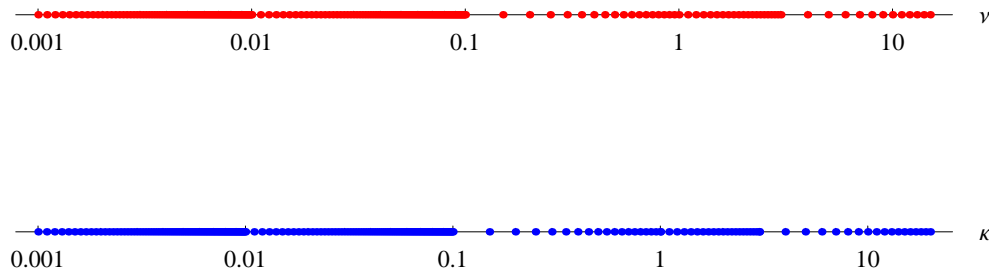
Figure 4.2: The resolution of points used to interpolate the model of lift and lift distribution by Graham (1970). The red dots are the normalized spanwise wave number. The blue dots are the normalized chordwise wave number. The resolution for the lift distribution is identical to the resolution for the lift coefficient. The values of the lift distribution have been inspected at values of ν where the numerical value of the lift distribution diverges.

tra). The wave number, k_2, is either k_z or k_y dependent on whether it is the 2-D model by Atassi (1984) (Subsection 2.1.3) or the 3-D model by Graham (1970) (Subsection 2.1.4), respectively. The symmetric property in Eqn. (4.1) is seen to be reasonable in Figure 4.1 because the absolute value of the transfer function is not changed when the wave front is symmetric in the direction of mean flow. The symmetric condition in Eqn. (4.1) is used in the expressions for spectra given in Sections 4.2, 4.3, 4.4, and 4.5. This assumption had to be made because the energy spectrum of the turbulence is double sided and the transfer functions are numerical valid for positive wave numbers only.

The integrations in Sections 4.2, 4.3, 4.4, and 4.5 are done numerically. The software used to do the numerical integration is not able to integrate the models to ∞ in order to get spectra. This issue has been solved by making a coordinate transformation such that the integration is over 0 to 1 and at the same time truncate the integration at an upper limit which is close to 1. The upper limit is dependent on the numerical behavior of the model at high values of the wave number over which the model is integrated. The 1-D model by Sears (1941) (Subsection 2.1.2) and the 2-D model are defined and give reasonable results for any choice of positive wave numbers.
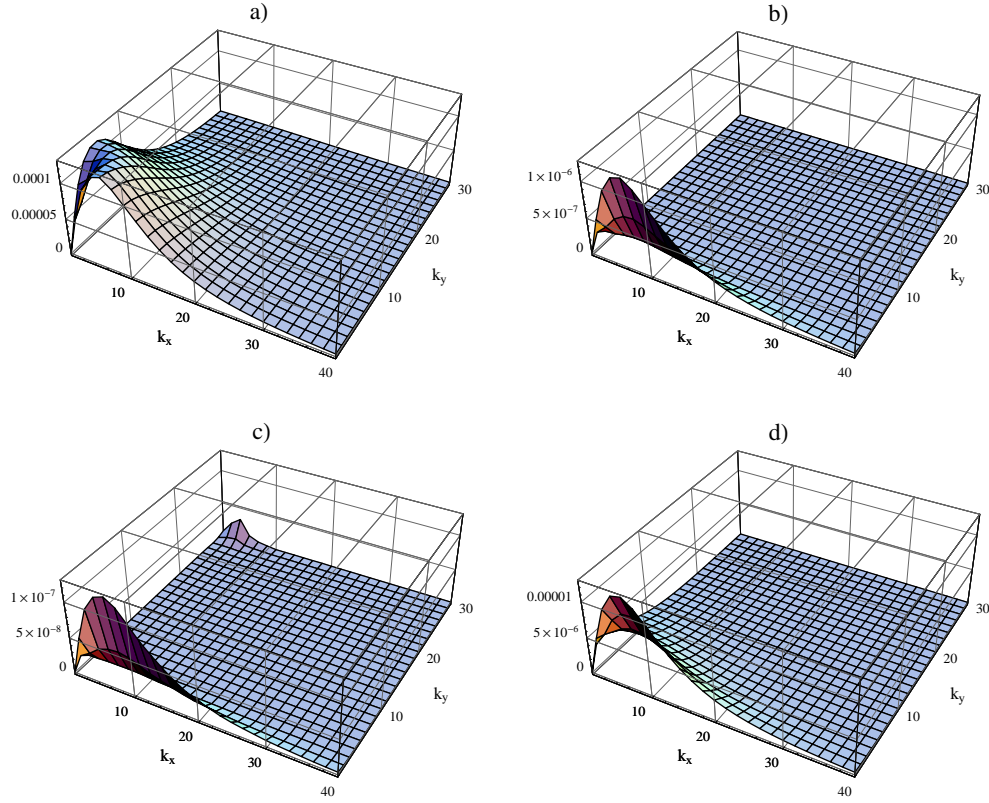
Figure 4.3: The integrand of the pressure spectrum and lift spectrum of the 3-D model by Graham (1970). The integrand of the pressure spectrum for the 3-D model given by Eqn. (2.96) is shown in a), b), and c) for $x/c - c/2$ equal to -.49, .01, and 0.41, respectively. The integrand of the lift spectrum for the 3-D model given by Eqn. (2.97) is shown in d).

The coordinate transformation used is given by

$$k_y = \frac{y_t}{1 - y_t}, \ y_t \in [0; 1[, \ k_y \in [0; \infty[\qquad (4.2)$$

where k_y is the spanwise wave number. This coordinate transformation has a Jacobian that is given by

$$dk_y = \frac{dy_t}{(1 - y_t)^2}. \qquad (4.3)$$

The upper limit of the integration is determined by the highest spanwise wave number at which the model converges to zero numerically. The upper

limit of integration for the coordinate transformation is thus given as

$$y_{t,up} = \frac{k_{y,up}}{1 + k_{y,up}} \qquad (4.4)$$

where the subscript $_{up}$ denotes the upper limit.

The upper limit for the 2-D model is introduced because the software used to do the numerical integration is not able to handle ∞ as the upper limit for this model. The upper limit of the integration is chosen as $y_t = 0.999$ which corresponds to a $k_y = 999$.

The upper limit for the 3-D model is determined by the validity of the numerics as the spanwise wave number, k_y, is increased.

Numerical considerations has been made to the calculation of transfer functions for the lift distribution (Eqn. (2.95)) and the lift (Eqn. (2.83)) for the 3-D model. Values for the 3-D model are found by approximating the solution in Chebychev series. This approximation has shown to be less good at high dimensionless spanwise wave numbers. The accuracy of the values of lift and lift distribution increase as higher the number, N, becomes at which the Chebychev series are truncated but the computational time increases as well. The Chebychev series are truncated at a N at which the time of computation is reasonable and the accuracy has converged on the fourth digit of the value of lift or lift distribution.

The 3-D model is numerically valid in a limited interval of wave numbers, only. Further the 3-D model is computationally slow. This has the consequence that the 3-D model is computed at the single points given in the mesh in Figure 4.2. The values of the model in the mesh are then interpolated linearly in order to perform the numerical integration. The mesh is chosen in order to have the finest resolution where the value of the model is largest. The value of the model is largest at low wave numbers of both k_x and k_y, consequently the resolution has to be fine at low wave numbers. The value of the model is decreasing as one of the wave numbers is kept constant and the other is increased. This is seen in Figures 4.3 and 4.4.

The computation of fluctuations of the lift is less time consuming than the calculation of the lift distribution. The lift is truncated at $N = 90$, the value of the lift is calculated and the absolute squared value is found. This calculation of the lift is carried out at the discrete points shown in Figure 4.2. These discrete values of the absolute squared of the lift fluctuations are then interpolated linearly.

The lift distribution is also calculated at the discrete values of wave numbers shown in Figure 4.2. The chord wise positions, x, of the calculations are discrete as well and the calculations are at 50 positions. The positions are regularly spaced with a distance, Δx, of 0.02 starting at $x = -.49$ and ending
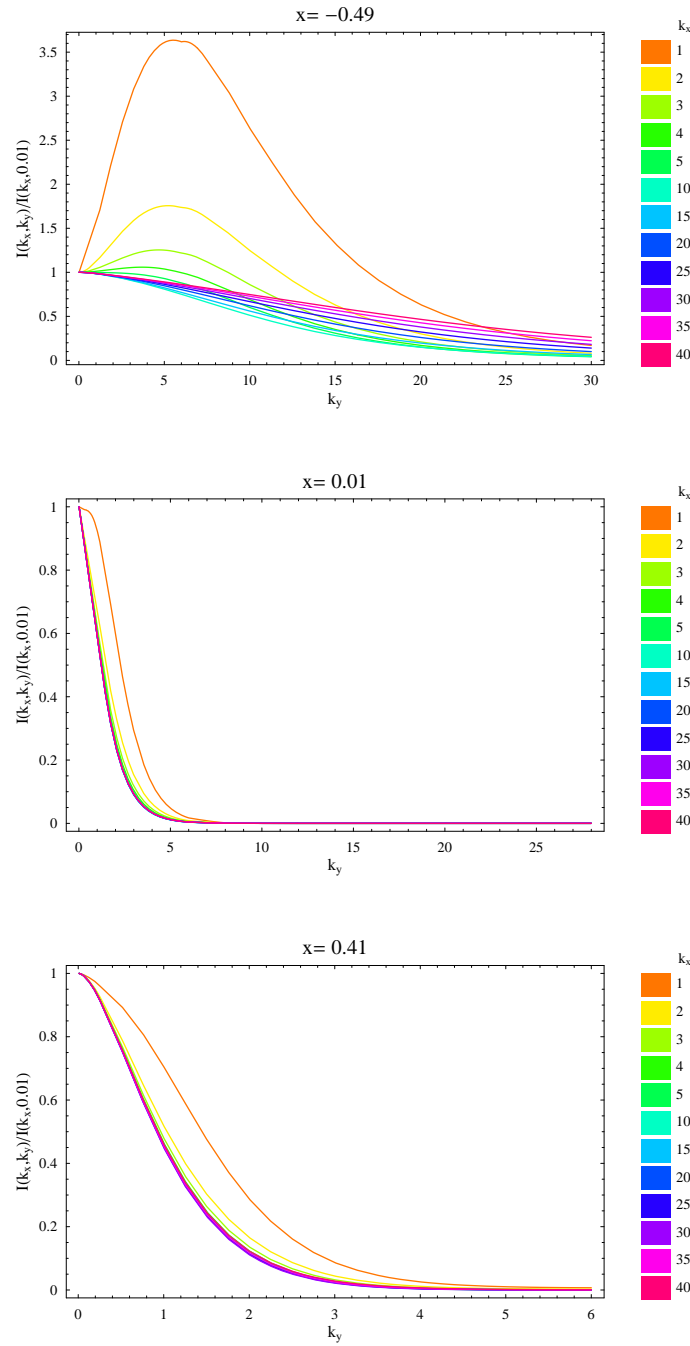
Figure 4.4: The integrand of the pressure spectrum at given chord wise wave number as function of spanwise wave number. The integrand of the pressure spectrum given by Eqn. (2.96) for the 3-D model by Graham (1970) is shown for $x/c - c/2$ equal to -.49, .01, and 0.41, respectively. The values are normalized with the value of the integrand at $k_y = 0.01$.
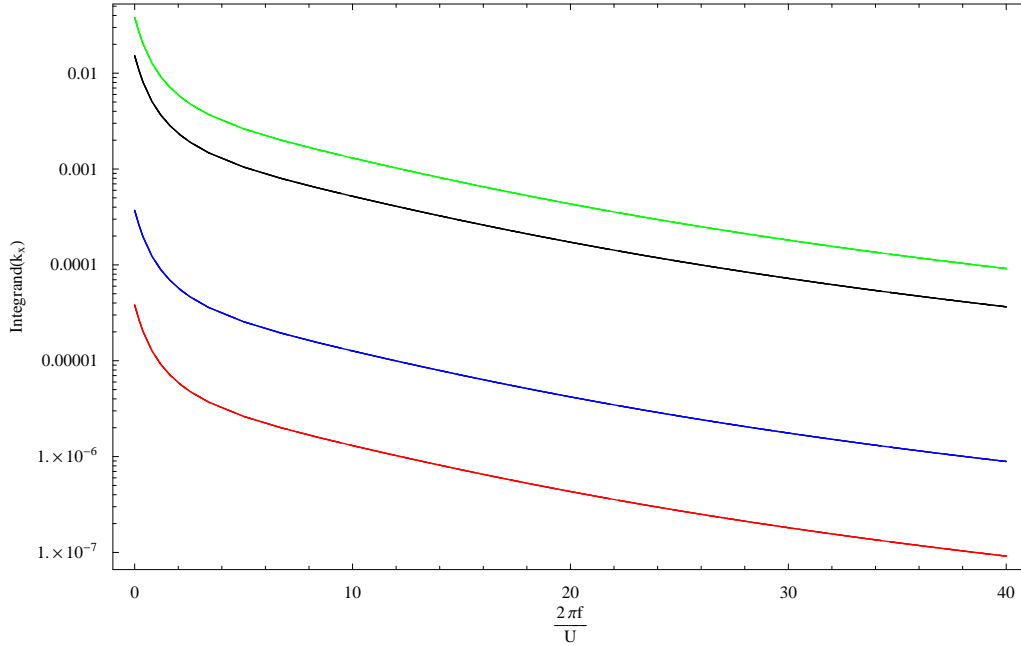
Figure 4.5: The integrand of the lift spectrum and pressure spectrum of the 1-D model given by Eqn. (2.97) and Eqn. (2.96), respectively. The black line is the integrand of Eqn. (2.97) for the 1-D model by Sears (1941). The green, blue, and red line are the integrand of Eqn. (2.96). The green line is at $x/c - c/2 = -0.49$, the blue line is at $x/c - c/2 = 0.01$, and the red line is at $x/c - c/2 = 0.41$.

at $x = 0.49$ where the leading edge is at $x = -0.50$ and the trailing edge at $x = 0.50$. The truncation of the Chebychev series is at two values of N. The truncation is at $N = 20$ for values of $\kappa \in [0, 3]$ and $\nu \in [0, 1]$ and outside this region the truncation is at $N = 64$. The values of N are chosen like this because the values of the lift distribution converge rapidly for $\kappa \in [0, 3]$ and $\nu \in [0, 1]$ and converge slower outside that region. The absolute square of the lift distribution is inspected for discrete κ as function of ν at all x. The value of the lift distribution is set equal to zero if it diverges at a value of ν. The diverging is at a different ν depending of the position, x, chord wise. Figure 4.4 shows the integrand at discrete values of κ at three chordwise positions. It is seen in the figure that the lift distribution is truncated at different values of ν depending on the chordwise position. The value of the integrand in Figure 4.4 diverges for higher values of ν.

The numerics does not converge close to the trailing edge, see Figures 4.3a) to c) and Figure 4.4. It is clearly seen in Figure 4.3c) that the value

of the integrand increases at high spanwise wave numbers. This increase is a numerical and not physical feature because the value of the lift distribution fluctuations converges to zero at high wave numbers. This is probably due to the approximation to series of Chebychev polynomials and the estimation of the Chebychev coefficients. The model further has to be truncated at some N. The higher N is chosen the longer the computation time. Further the accuracy of the model is becoming independent of the choice of N and is not improved at high wave numbers in both directions. The range of spanwise wave numbers used to calculate the pressure spectra and SPL is becoming smaller at a certain point of the chord because the integrand has to be truncated at some spanwise wavenumber.

The integrand for the lift spectrum for the 3-D model is seen in Figure 4.3d). It is seen to behave nicely in the grid of Figure 4.2. The value of the transfer function outside the shown grid blows up and this is not believed to be physical because the higher the wave number becomes in any direction the less impact it will have on the lift (the lift fluctuations are becoming very small). This implies that the aerofoil can not feel and respond to the disturbance of the turbulence, and thus the lift fluctuations and the lift distribution goes to an absolute value of zero.

The transfer function for the lift distribution of the 1-D model in Eqn. (2.45) has to be truncated at $n = N$ where N is finite. An explicit expression can not be found for the infinite sum thus the sum has to be truncated. Figure 4.5 shows Eqn. (2.96) in which Eqn. (2.45) is truncated with N equal to 5, 10, 64, and 128. The lines are on top of each other and no difference is seen so the sum in Eqn. (2.45) could be truncated at $N = 5$ but $N = 10$ is chosen for the calculations of the pressure spectra in Eqn. (2.96) and the SPL in Eqn. (2.153). It is also seen in Figure 4.5 that the value of the integrand is decreasing from leading edge (green line) to trailing edge (red line), and the integrand is furthermore converging. The black line in Figure 4.5 shows the integrand of the lift for the 1-D model in Eqn. (2.97) and this converges as well as the integrand for the pressure spectra.

The integrand for the 2-D model is seen in Figure 4.6, where the integrand for three different AOA's for both the NACA0015 and NACA63415 profile is shown. It is seen that the integrand changes both when the AOA is changed and the camber is fixed and when the camber is changed and the AOA is fixed.

The interval of chord wise wave numbers used in the figures of Sections 4.2, 4.3, 4.4, and 4.5 are chosen because of the numerical limitations of the 3-D model. This interval is chosen in order to be able to compare the three models with each other and to be able to compare the models with data.

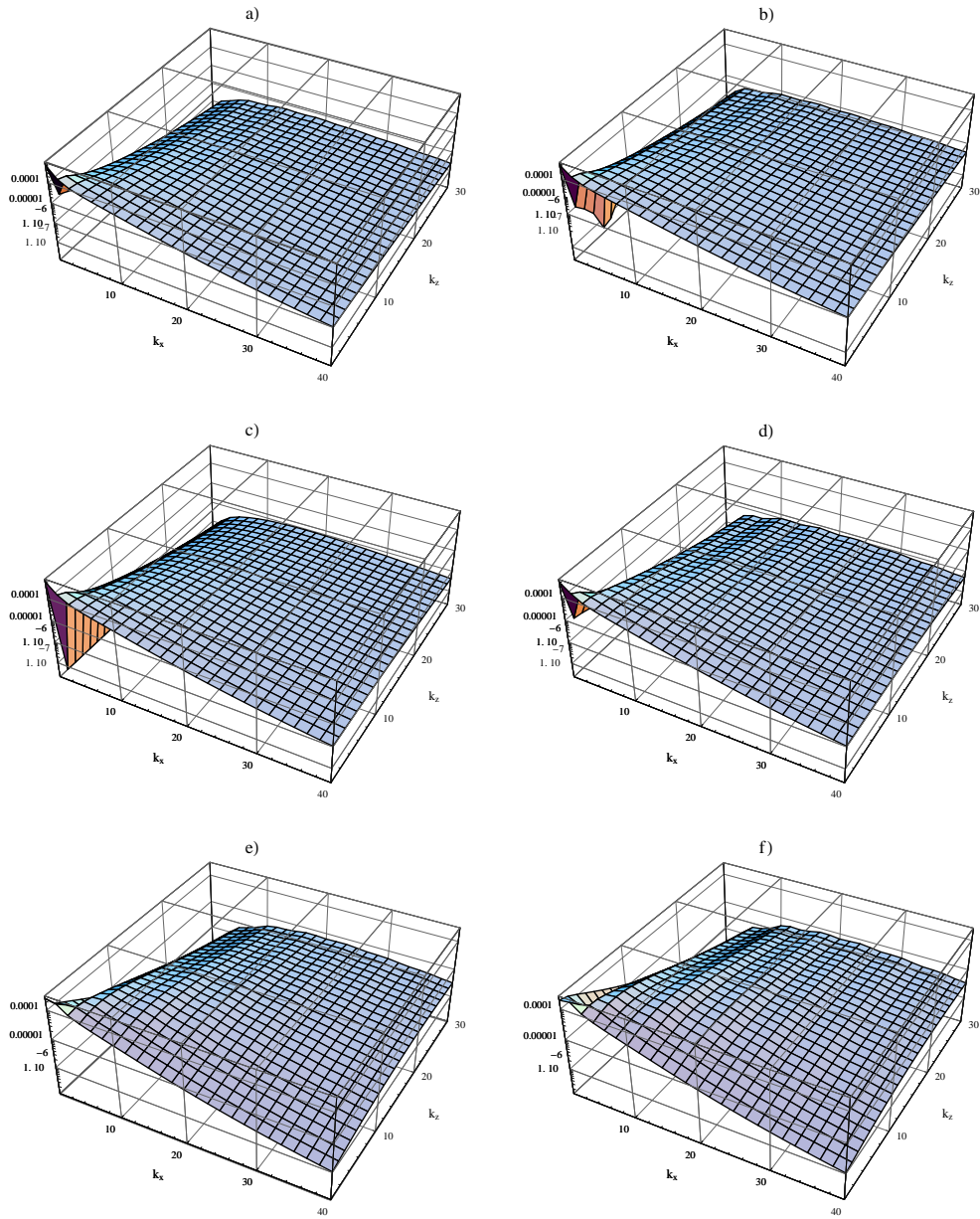The transfer functions are dimensionless. Thus the integrations of models

Figure 4.6: The integrand of the lift spectrum given in Eqn. (2.97) for the 2-D model by Atassi (1984), see also Subsection 4.3.1. The left column is for camber corresponding to the NACA0015 profile. The right column is for camber corresponding to the NACA63415 profile. The rows are for AOA's equal to -3.15°, 0.19°, and 9.88°, respectively from top to bottom.

	Run 1		Run 2		Run 4	
Leg	$\mathcal{L}$ [m]	ϵ	$\mathcal{L}$ [m]	ϵ	$\mathcal{L}$ [m]	ϵ
1	0.055	0.021	0.054	0.017	0.024	1.456
2	0.058	0.044	0.057	0.044	0.03	1.646
3	0.061	0.065	0.082	0.056	0.03	1.778
4	0.064	0.068	0.079	0.064	0.029	1.822
5	0.061	0.083	0.077	0.068	0.03	1.899
6	0.06	0.077	0.072	0.098	0.031	1.876
7	0.066	0.053	0.054	0.008	0.028	1.981
8	0.06	0.061	0.057	0.035	0.031	1.275
9	0.065	0.058	0.08	0.069	0.027	1.871
10	0.065	0.047	0.069	0.091	0.027	1.935
11	0.059	0.081	0.069	0.091	0.024	1.838
12	0.064	0.059	0.073	0.106	0.03	1.436
13			0.054	0.007	0.027	1.912
14			0.057	0.035	0.023	2.01
15			0.086	0.067	0.023	1.94
16			0.079⋄	0.067⋄	0.022	2.095
17			0.075	0.089	0.018	2.21
18			0.072∗	0.114∗		

Table 4.1: Estimates of $\mathcal{L}$ and ϵ from the NACA0015 experiment.

in Sections 4.2, 4.3, 4.4, and 4.5 give the dimensions of velocity squared and have to be multiplied with the function, $A^2(\rho, U, c)$. The function is recalled from Eqn. (2.52) as

$$A(U, c) = \frac{1}{2}\rho c U$$

where ρ is the density of air, c is the chord length and U is the mean wind speed. The function is called the amplification factor.

4.1.2   Model Parameters from Data

The data has to be used as input in the models in order to obtain pressure spectra and lift spectra. This has to be done to estimate a realistic energy spectrum for the turbulence and to find the amplification factor.

The data obtained from a triple wired hotwire are used to estimate the length scale, $\mathcal{L}$, and the mean kinetic energy dissipation, ϵ. The two parameters are estimated by fitting to the spectra of the three turbulence components, u, v, w, see Table 4.1. The curves are fitted by the least squares

method and $\mathcal{L}$ and ϵ are unique for a single leg. The hotwire is believed to give reliable results for the turbulence, but the calibration of the instrument was not good enough to be used for the mean wind speed. Hotwire data were obtained only in the experiment with the NACA0015 profile. The estimates for $\mathcal{L}$ and ϵ from the NACA0015 experiment is used for the NACA63415 experiment as well. The flow conditions and turbulence generation are believed to be similar in the two experiments so it is satisfactorily to use estimates of $\mathcal{L}$ and ϵ at similar mean wind speeds for the NACA63415 experiment. The estimate of the two parameters in Run 1 for the NACA63415 profile are taken from Run 2, Leg 18 in the experiment with a NACA0015 profile and the values are shown with a $*$ in Table 4.1. Similarly $\mathcal{L}$ and ϵ in Run 2 and Run 3 for the NACA63415 profile are taken from Run 2, Leg 16 in NACA0014 experiment and the values are shown with a $\diamond$ in Table 4.1.

The data from the 5-hole pitot tube is used to estimate the mean wind speed. The mean wind was measured with a cup anemometer as well. The data from the 5-hole pitot tube are very similar to those of the cup anemometer. The mean wind speeds estimated from the 5-hole pitot tube data is used to find the correct amplification factor. The function, $A^2(\rho, c, U)$, is multiplied with the spectra of the pressure and lift spectra.

The corrected AOA's are found from the pressure data obtained by the pressure tubes. The mean pressure of the data from the pressure tubes are known to be reliable and have been used for estimating corrected AOA's several times with reliable results as discussed previously.

The spectra of pressure and lift from the pressure data obtained by microphones have peaks at certain frequencies (wave numbers). The peaks are at different wave numbers because $k_x = \frac{f}{U}$ and the data are not obtained at same mean wind speed at all runs. Furthermore the peaks are ignored when spectra from data and models are compared because the peaks coincide with the peaks in the pressure spectra obtained by the background microphone, see Figure 3.13. Thus the peaks in spectra of pressure and lift are considered not to be of aerodynamical origin but to be due to the wind tunnel.

4.2 Pressure

This section discusses the fluctuating pressure, p. The pressure spectra will be found in order to compare data and models. It is a simple task to find the pressure spectra from data and it is done as in Chapter 3.
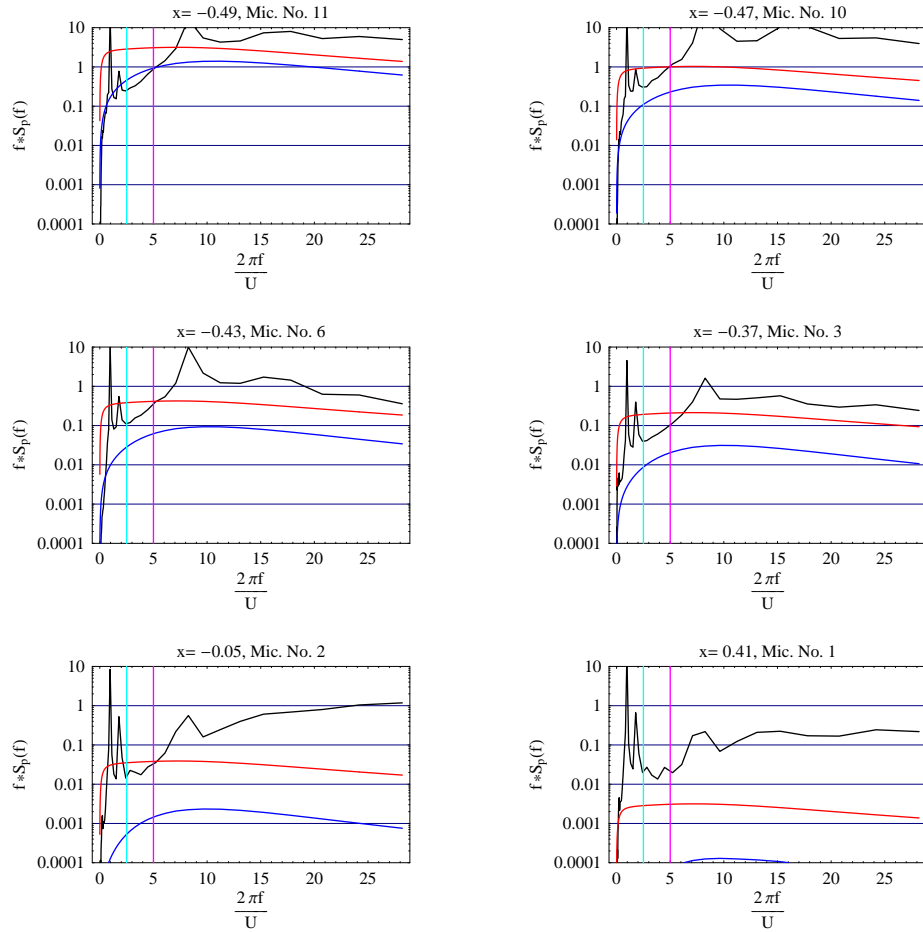
Figure 4.7: Comparison of pressure spectra from data and models at run 3, leg 4 for the NACA0015 profile(see Table 3.4). The pressure spectra, $fS_p(f)$, are plotted against wave number. The data are black, the 1-D model is shown in red and the 3-D model is shown in blue. The data are obtained at a mean wind speed of 25 m/s.

4.2.1   Estimation of Pressure Spectra from Models

The models that are able to predict the fluctuating pressure at a given point of the aerofoil are the 1-D model by Sears (1941) (Eqn. (2.45)) and the 3-D model by Graham (1970) (Eqn. (2.91)). The turbulence is assumed to be isotropic which is a valid assumption according to Chapter 3. The data from the hot wire are used to estimate the length scale, $\mathcal{L}$, and the mean kinetic energy dissipation, ϵ. These two parameters are used in the spectrum given by Eqn. (2.114) (von Kármán 1948).

The pressure spectrum when the 1-D model is chosen is by Eqn. (2.96) given as

$$S_{p,1D}(x, k_x) = A^2(\rho, c, U)\Phi_{ww}(k_x)\left| g\left(x, \frac{k_x c}{2}\right)\right|^2 \tag{4.5}$$

where $\Phi_{ww}(k_x)$ is given by Eqn. (2.114).

Likewise the pressure spectrum when the 3-D model is used becomes

$$S_{p,3D}(x, k_x) = 2A^2(\rho, c, U)\int_0^\infty \Phi_{ww}(k_x, k_y)\left| g\left(x, \frac{k_x c}{2}, \frac{k_y c}{2}\right)\right|^2 dk_y \tag{4.6}$$

where $\Phi_{ww}(k_x, k_y)$ is given by Eqn. (2.113).

It is seen from Eqns. (4.5) and (4.6) that the spectra calculated by Eqn. (4.6) give a lower value than the spectra calculated by Eqn. (4.5). The reason for this is that $\left| g\left(x, \frac{k_x c}{2}, 0\right)\right| > \left| g\left(x, \frac{k_x c}{2}, \frac{k_y c}{2}\right)\right|$ for any $k_y > 0$. Thus the pressure spectra of the 1-D model will be above the pressure spectra of the 3-D model when the spectra are plotted as function of k_x.

4.2.2   Comparison of Models and Data

The pressure spectra for models and data are compared in Figures 4.7 to 4.9. The property in Eqn. (2.98) is used in order to compare the wave number regime with the frequency regime. The plots show the data, the 1-D model and the 3-D model for a selection of microphones. The data are chosen for cases at an effective AOA of 0°.

The microphones chosen for the NACA0015 profile in Figure 4.7 are the ones along the dashed line in Figure 3.5 and are shown from the leading edge to the trailing edge from the top left corner to the lower right corner, respectively. The plots show that the data are approximately 1-2 decades higher than for the 1-D model in general. The data from microphones near the leading edge ($\frac{x}{c} - \frac{c}{2} = -0.49$ to $\frac{x}{c} - \frac{c}{2} = -0.39$, see also Table 3.1) follow the features of the 1-D model quite well though with an amplitude of
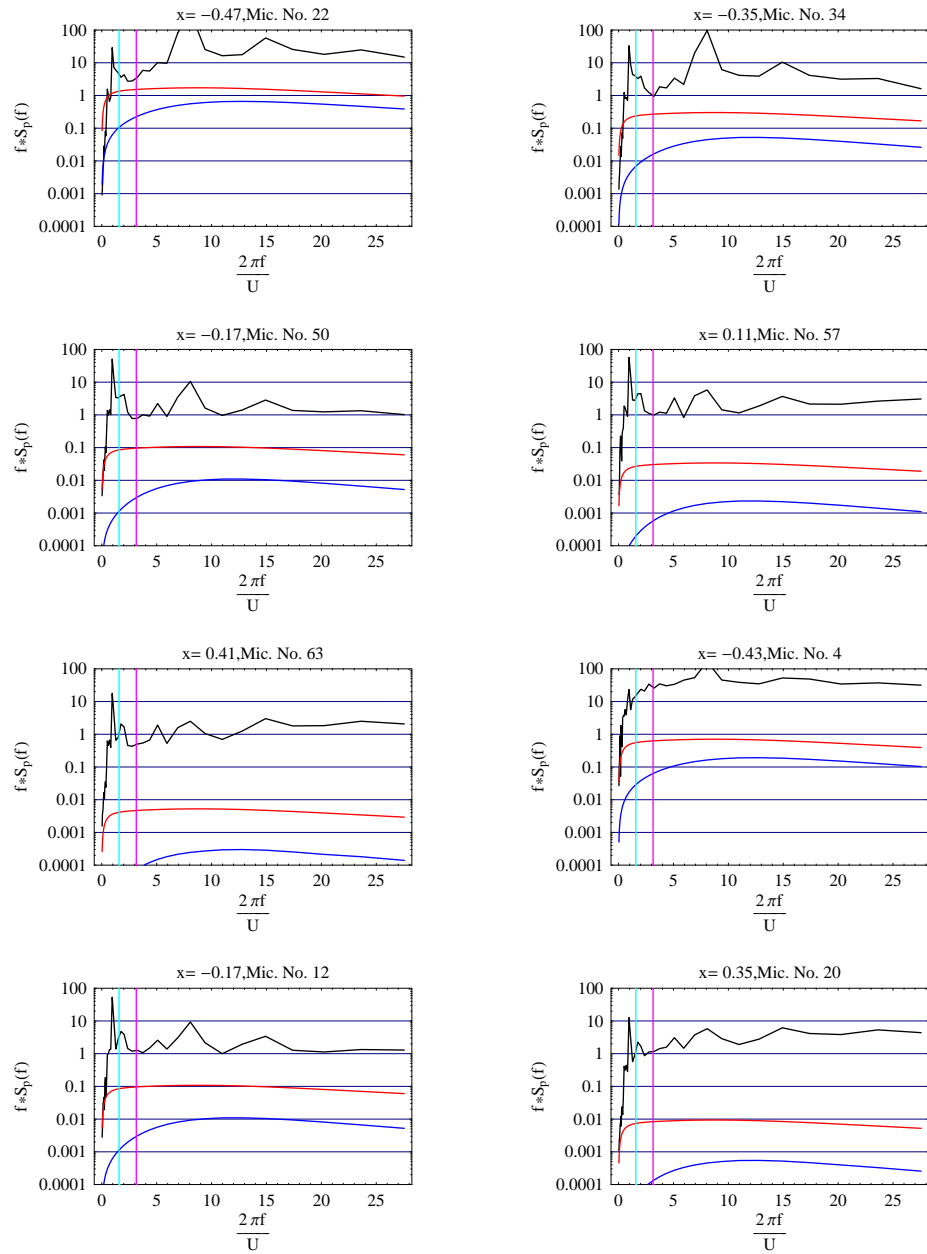
Figure 4.8: Comparison of pressure spectra from data and models at run 1, leg 5 for the NACA63415 profile (see Table 3.8). The pressure spectra, $fS_p(f)$, are plotted against wave number. The data are black, the 1-D model is red and the 3-D model is blue. The data are obtained at a mean wind speed of 40 m/s.

approximately 1 decade. The microphones 2 and 1, which are close to mid-chord and the trailing edge, respectively, show a greater difference from the 1-D model than the microphones close to the leading edge. This might be because the flow may not be considered inviscid downstream of microphone 3.

The Figures 4.8 and 4.9 show the comparison of models and data obtained from the NACA63415 profile. The data are at zero lift conditions, and the data in Figure 4.9 are tripped. The microphones shown in the figures are placed at the green line in Figures 3.9 and 3.10, and they are all placed 86mm from mid-span to the right of the incoming flow. The order of microphones are from leading edge towards trailing edge by moving from top left to the right and from top to bottom in the plots. The first five microphones are on the suction side. The three last microphones in the plots are on the pressure side. The difference between data and the 1-D model is approximately 1-2 decades at the suction side from the leading edge to about mid-chord. This is the case at a mean wind speed of both 30 m/s and 40 m/s. The difference is larger after mid-chord and is increasing to about 2 decades close to the trailing edge at microphone 63. The difference between data and models are larger on the suction side than on the pressure side. The difference at the suction side near leading edge is approximately 1.5 decade and increases to more than 2 decades near trailing edge in both Figure 4.8 and Figure 4.9.

It is seen that the pressure fluctuations decrease in magnitude from the leading edge to trailing edge in the data from the three runs shown in this section. This is as expected from theory (Figure 2.7). The difference between models and data increases from mid-chord to trailing edge. The aerofoils used, NACA0015 and NACA63415, have different properties but they show equal magnitude of difference between data and models. The difference increases slightly with increasing mean wind speed (increasing Reynolds number). Tripping seems not to affect the pressure because the difference between models and data are similar in Figures 4.8 and 4.9. It is seen in Figures 4.7 to 4.9 that the pressure difference between data and the 1-D model is systematically around 1 decade from the leading edge to about mid-chord for both the NACA0015 profile and the NACA63415 profile. The difference between data and the 1-D model increases from about mid-chord to trailing edge to more than 2 decades.

Reasons for the pressure fluctuations from data to be systematically higher than the 1-D model and thereby the 3-D model are given below in Section 4.3.3.
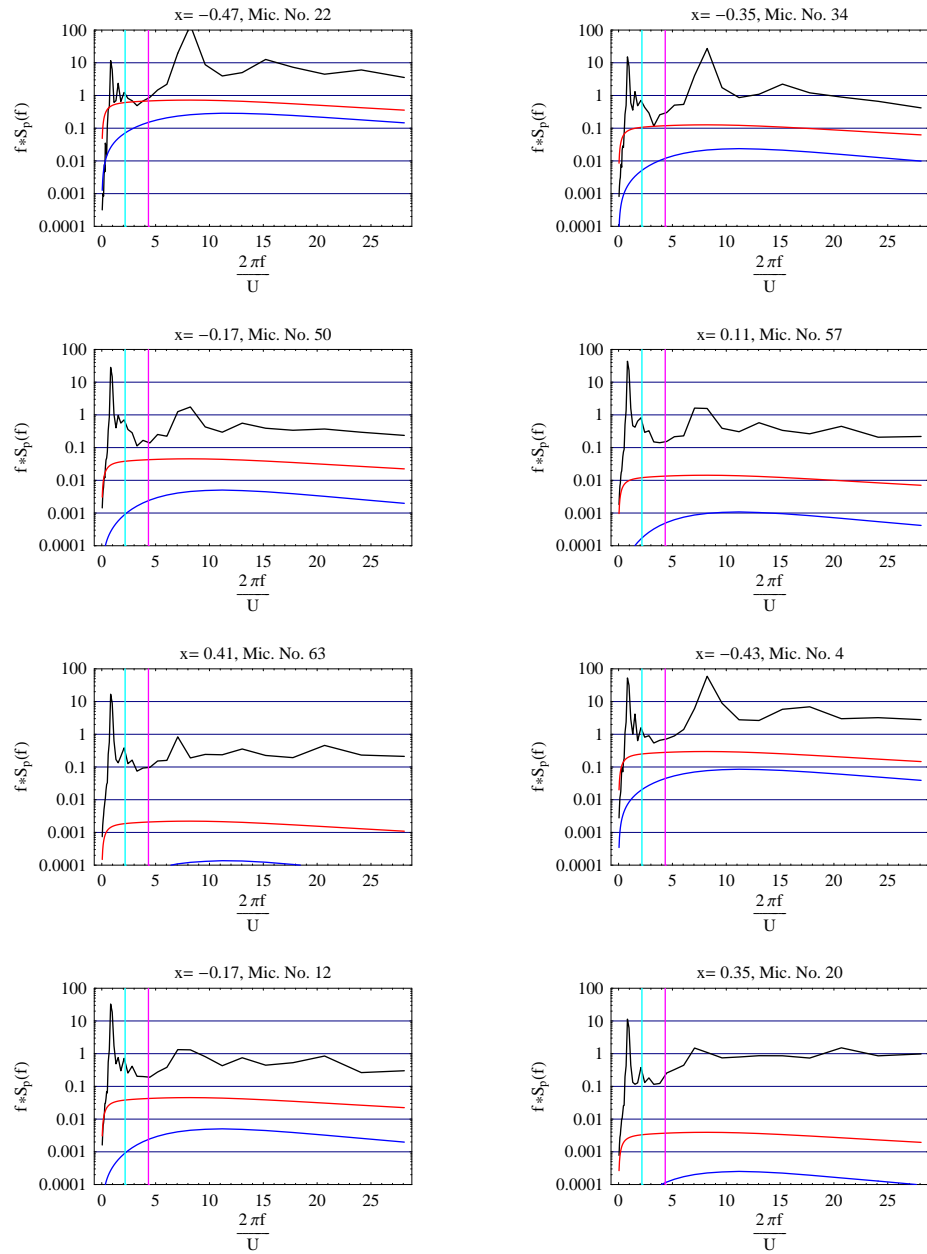
Figure 4.9: Comparison of pressure spectra from data and models at run 3, leg 1 for the NACA63415 profile (see Table 3.8). The pressure spectra, $fS_p(f)$, are plotted against wave number. The data are black, the 1-D model is red and the 3-D model is blue. The data are obtained at a mean wind speed of 30 m/s.
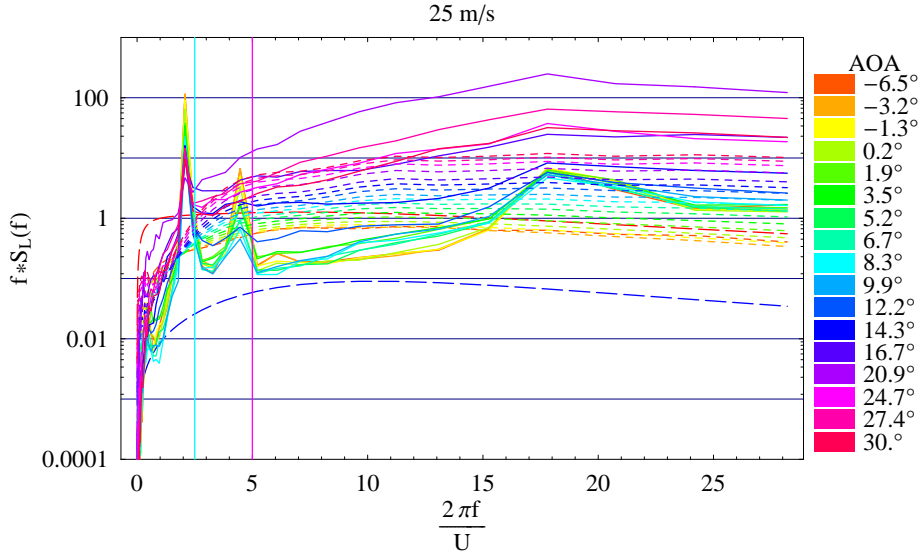
Figure 4.10: Comparison of lift spectra from data and models at run 3 for the NACA0015 profile. The colour legend is for data (full line) and the 2-D model (short dashed line). The long dashed lines represent the 1-D model (red) and 3-D model (blue). The lift spectra, $fS_L(f)$ are plotted against wave number.

4.3 Fluctuating Lift

The fluctuating lift, L', will be discussed in this section in terms of its spectrum. The issue is to investigate which model fits data best. The models have to be treated differently. The data are discrete so assumptions have to be made in order to estimate L' from these.

4.3.1 Estimation of Lift Spectra from Models

The symmetry mentioned in Section 4.1 is used to estimate the transfer functions of L' for the models. The spectrum of the lift, $S_L(k_x)$, for the models is estimated by Eqn. (2.97). The turbulence and the parameters are as for the pressure. The lift fluctuations from the 1-D model by Sears (1941) are described by Eqn. (2.49). The lift spectrum for the 1-D model is then found as

$$S_{L,1D}(k_x) = A^2(\rho, c, U)\Phi_{ww}(k_x)\left|g\left(\frac{k_xc}{2}\right)\right|^2 \tag{4.7}$$

because the spanwise wavenumbers are assumed to be coherent.

Similarly the 3-D model from Graham (1970) and given by Eqn. (2.83) is implemented into Eqn. (2.97) to give

$$S_{L,3D}(k_x) = 2A^2(\rho, c, U) \int_0^\infty \Phi_{ww}(k_x, k_y) \left| g\left(\frac{k_x c}{2}, \frac{k_y c}{2}\right) \right|^2 dk_y, \qquad (4.8)$$

where the numerical assumptions and methods discussed in Subsection 4.1.1 are utilized. The lift spectra calculated by Eqn. (4.7) will be above the lift spectra by Eqn. (4.8) by use of similar arguments as in Section 4.2.

The 2-D model described by Goldstein and Atassi (1976), Atassi (1984) and Eqn. (2.66) has to be treated in a slightly different way, because it is affected by two velocity components, u and w. The lift spectrum takes into account the contributions from both of these components. It becomes

$$S_{L,2D}(k_x, \beta_A, m) = 2A^2(\rho, c, U) \int_0^\infty n_i \Phi_{ij}(k_x, k_z) n_j \left| g\left(\frac{k_x c}{2}, \frac{k_z c}{2}, \beta_A, m\right) \right|^2 dk_z$$

$$\mathbf{n} = \frac{\{k_x, 0, k_z\}}{\sqrt{k_x^2 + k_z^2}} \qquad (4.9)$$

where the transfer function for the lift is a function of the AOA, $\beta_A = \frac{AOA\pi}{180}$, and the second order coefficient, m, of a parabolic fit to the mean line of the profile.

4.3.2   Estimation of Lift Spectra from Data

Data have to be treated differently for the two aerofoils used in the experiments mentioned in Chapter 3.

The data on the NACA 0015 profile are obtained on the suction side only from microphones. This means that the flat plate assumption of the pressure difference over the aerofoil

$$\Delta p'(x, t) = -2p'(x, t) \qquad (4.10)$$

as mentioned in Chapter 2 has to be made. Then L' can be estimated by using a trapezoidal method to numerically integrate as

$$L'(t) = \sum_i^{N-1} [\Delta p'(x_i, t) n_z(x_i) + \Delta p'(x_{i+1}, t) n_z(x_{i+1})] \times |s(x_{i+1}) - s(x_i)|$$

$$(4.11)$$

where $n_z(x_i)$ is the vertical component of the normal vector at the surface of the profile at the chordwise position, x, for the ith microphone. Likewise $s(x_i)$
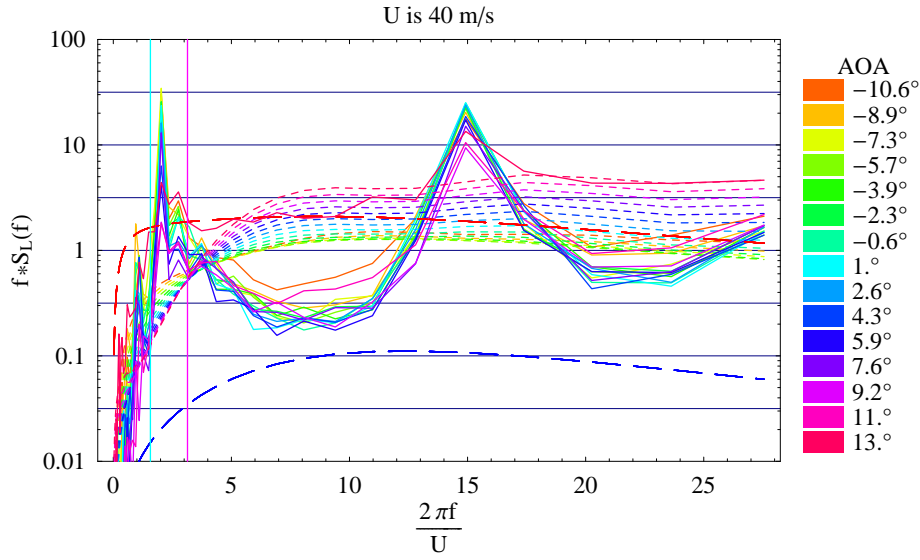
Figure 4.11: Comparison of lift spectra from data and models at run 1 for the experiment with a NACA63415 profile. The colour legend is for data (full line) and the 2-D model (short dashed line). The long dashed lines represent the 1-D model (red) and 3-D model (blue). The lift spectra, $fS_L(f)$, are plotted against wave number.

is the distance from the leading edge to the the position of the ith microphone along the surface of the aerofoil. N is the number of microphones used to estimate L'; N is 6 for the NACA 0015 profile, see Figure 3.5. The integration is by Eqn. (4.11) not over the entire chord but only between 0.2% to 91.7% chord.The remaining parts are abandoned. This method introduces an error in the lift that may not be seen in the spectrum of the lift, because the abandoned part may not give extra information in the frequency domain. The lift force is by definition the normal force component to the chord line. That is the reason for using n_z only.

The data from the NACA 63415 profile are obtained from microphones on both suction and pressure side, see Figure 3.7. L' is in this case estimated

as

$$
\begin{aligned}
L'(t) \;=\; & \sum_{i}^{N-1} \Big\{ \, [p'(x_i, z_i, t)n_z(x_i, z_i) + p'(x_{i+1}, z_{i+1}, t)n_z(x_{i+1}, z_{i+1}))] \\
& \times |s(x_{i+1}, z_{i+1}) - s(x_i, z_i)| \Big\} \\
+ \;& [p'(x_1, z_1, t)n_z(x_1, z_1) + p'(x_N, z_N, t)n_z(x_N, z_N)] \\
& \times |s(x_N, z_N) - s(x_1, z_1)|.
\end{aligned} \tag{4.12}
$$

The last term is to close the path integral. The number of microphones used (N) is 49 in this experiment. Eqn. (4.12) integrates over the entire profile with a relatively high number of points. The estimate in this case is thus believed to be more accurate than Eqn. (4.11) for the experiment with the NACA0015 profile. The microphones are in Eqn. (4.12) assumed to be on a line but they are placed on different spanwise positions (Figures 3.9 and 3.10 and Table 3.7). The microphones are believed to be close enough that the error is minimized and the assumption of the microphones being on a line is valid. The assumptions are based on that the frequencies investigated in this thesis are in the low frequency domain such that the phase is not likely shifted much for the small distances in question. The microphones were not placed in a straight line of experimental reasons, because it could have lead to more uncertainties originating from the holes for the microphones.

4.3.3   Comparison of Models and Data

The lift spectrum is seen for run 3 of the experiment with a NACA0015 profile in Figure 4.10. It is seen that the data are on top of each other until separation occurs at 12°. The lift spectrum increases after the AOA where separation occurs. The fact that data are not affected by change in AOA below separation is not expected. The 2-D model which is shown with short dashed lines predicts that the AOA could have an influence. The data are above the 1-D model (long red dashed line) at a frequency ~ 50Hz. The data is assumed to be between the 1-D model and the 3-D model (long blue dashed line). This is assumed because the turbulence used together with the 3-D model is isotropic and the turbulence used with the 1-D model can be regarded as completely anisotropic, and the data are obtained under near isotropic conditions, see Table 3.10. This assumption might be valid because the turbulence will be coherent along the aerofoil if it is anisotropic, as is the case in Eqn. (4.7). Spanwise effects are included in Eqn. (4.8). It then seems reasonable to assume that the lift fluctuations obtained from data would be in between Eqns. (4.7) and (4.8).
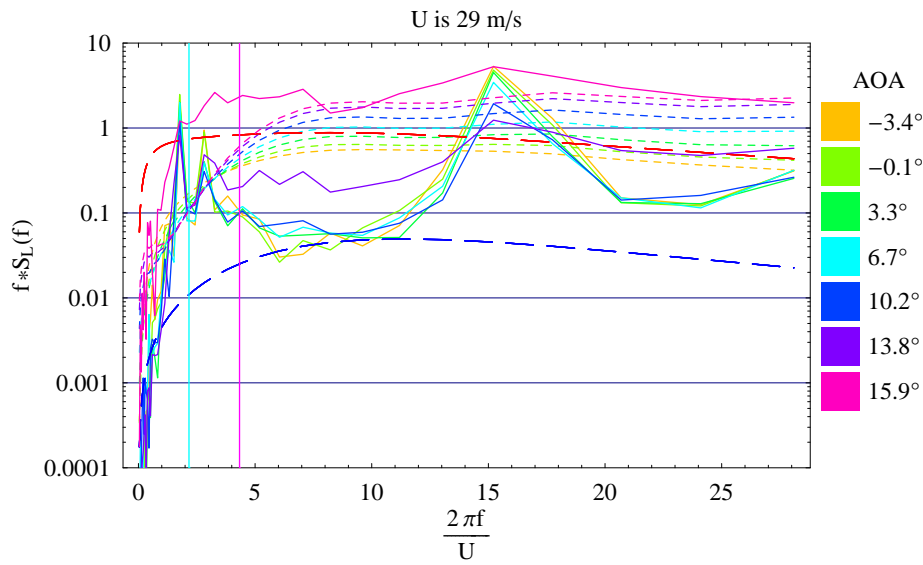
Figure 4.12: Comparison of lift spectra from data and models at run 3 for the experiment with a NACA63415 profile. The colour legend is for data (full line) and the 2-D model (short dashed line). The long dashed lines represent the 1-D model (red) and 3-D model (blue). The lift spectra, $fS_L(f)$, are plotted against wave number.

The lift spectra from the experiments with the NACA63415 profile are shown in Figures 4.11 and 4.12. The data show also for the NACA63415 profile that no effect of AOA is present below the separation angle being in this case 11°. The data fall between the 1-D model and the 3-D model in most of the frequency interval. The case which is tripped, Figure 4.12, is well in between models.

The figures 4.10 to 4.12 show the lift spectrum for the three models and for the data. It is seen that no effect of AOA is present in the data below the AOA where separation occurs, see Chapter 3. All data below separation are more or less on top of each other. This is surprising because the 2-D model predicts a difference.

The separation is seen in data from both experiments, but no effect of AOA is seen in data, surprisingly. Errors because of low spatial resolution are expected at high frequencies especially on the NACA0015 profile because few points are used to calculate the lift. This low spatial resolution causes high frequencies not to be captured well. The error because of the low spatial resolution is expected to increase with increasing wave number (frequency)

because high frequencies require high resolution to be captured well. The systematic error in pressure seem to be eliminated in the lift because the lift spectra is between the 1-D model and the 3-D model or are just above the 1-D model. The reason for the elimination of the error may be that the background noise is filtered out when integrated. The assumed origin of the background noise is discussed in Section 4.2.2. The phases of the pressure which is causing higher values in the pressure spectra might be statistically independent over the aerofoil such that they are canceled out. This canceling effect is then decreasing the integrated pressure, the lift. Other incoherent sources of noise of aerodynamical or acoustical origin in the measurements will also partly average out in the lift signal. The lift spectrum increases above the angle of separation which is expected to be due to increasing generation of aerodynamical turbulence.

The figures 4.10 to 4.12 show that the data are in between the 1D-model by Sears (1941) and the 3-D model by Graham (1970). The tripped case in Figure 4.12 shows that data are well in between the models for the frequency range, which gives confidence that a real wind turbine will do so too. A real wind turbine will do so because it is exposed for weathering which will cause a boundary layer similar to tripping.

The lift fluctuations from data were expected to be closer to the 3-D model because spanwise effects of the vertical gust are included. An explanation that this is not the case is the quality of the pressure data obtained by microphones. The wind tunnel in which the experiments are carried out is not anechoic, and this might have caused the pressure data to be systematically higher and also that the lift fluctuations are not as low as the 3-D model predicts. Furthermore aerodynamically phenomena as transition from laminar to turbulent flow in the boundary layer of the aerofoils might have increased the pressure fluctuations systematically and the lift fluctuations to a lesser degree.

The model by Graham (1970) is by the arguments above regarded as the model which predicts the lift fluctuations most reliably.

4.4   Sound Pressure Level

The SPL estimated from the 1-D model by Sears (1941), the 3-D model by Graham (1970), and the original model by Amiet (1975) are compared in this Section. This comparison is carried out in order to investigate how other models for the lift distribution will estimate the SPL in the acoustic model. The comparison is made for the turbulence parameters in Table 4.1 for the experiments in Chapter 3. A comparison is also made for turbulence

parameters representative of a wind turbine. Further the dipole structure of the acoustic model is investigated.

The SPL is estimated by the model by Amiet (1975). This model is described in Section 2.4 and is used at different stages dependent on which model for the lift distribution is used. The 1-D model and the 3-D model are implemented into Eqns. (2.135) and (2.151). The lift distribution used in Amiet (1975) is given by Eqns. (2.142) and (2.143) which gives an estimate of the SPL given by Eqn. (2.153).

Figure 4.13 compare the models at three different flow conditions. The mean velocity is in Figure 4.13 from top to bottom 25m/s, 15m/s, and 30 m/s, respectively. The 1-D model and the 3-D model have SPL's that is below the model for the lift fluctuations by Adamczyk (1974) and used by Amiet (1975).

Because the lift spectra for data are in between the 1-D model by Sears (1941) and the 3-D model by Graham (1970) ($kS_{L,1D}(k) > fS_{L,Data}(f) > kS_{L,3D}(k)$) then it is assumed that this also will be the case for the SPL from data. It has not been possible to estimate the SPL from data, because that requires a larger number of microphones to get a good measure of the cross spectra of the pressure.

The model for the SPL given by Eqn. (2.153) is not able to estimate the SPL at an arbitrary point in space but is constrained to any point vertical (z-direction) of the mid point (mid chord) of the aerofoil. The model given by Eqn. (2.153) is simplified such that only points in z-direction of the mid chord of the aerofoil can be estimated. The 1-D model and the 3-D model are not constrained and are thus able to estimate the SPL in any point in space. The behavior of the SPL in a spanwise section in a circle of 10m radius around the aerofoil is shown in Figure 4.14. The dipole is modified by the mean flow and the modification is greater the higher the frequency becomes. A perfect dipole is depicted in Figure 4.14 by a thick black line. The modification of the dipole is greater downstream than upstream.

The parameters of a wind turbine are found by using empirical laws for the wind profile near the surface in the atmosphere and for the energy dissipation. The wind speed at hub height, $U(z)$, is set to 8m/s which is a reasonable value for an operational wind turbine. The hub height is set to $z = 67$m, which corresponds to a Vestas V80 wind turbine. The logarithmic wind profile is used to estimate the friction velocity, u_*. The logarithmic wind profile is valid for neutral atmospheric conditions and is given as

$$U(z) = \frac{u_*}{\kappa_K} \ln \frac{z}{z_0, R} \tag{4.13}$$

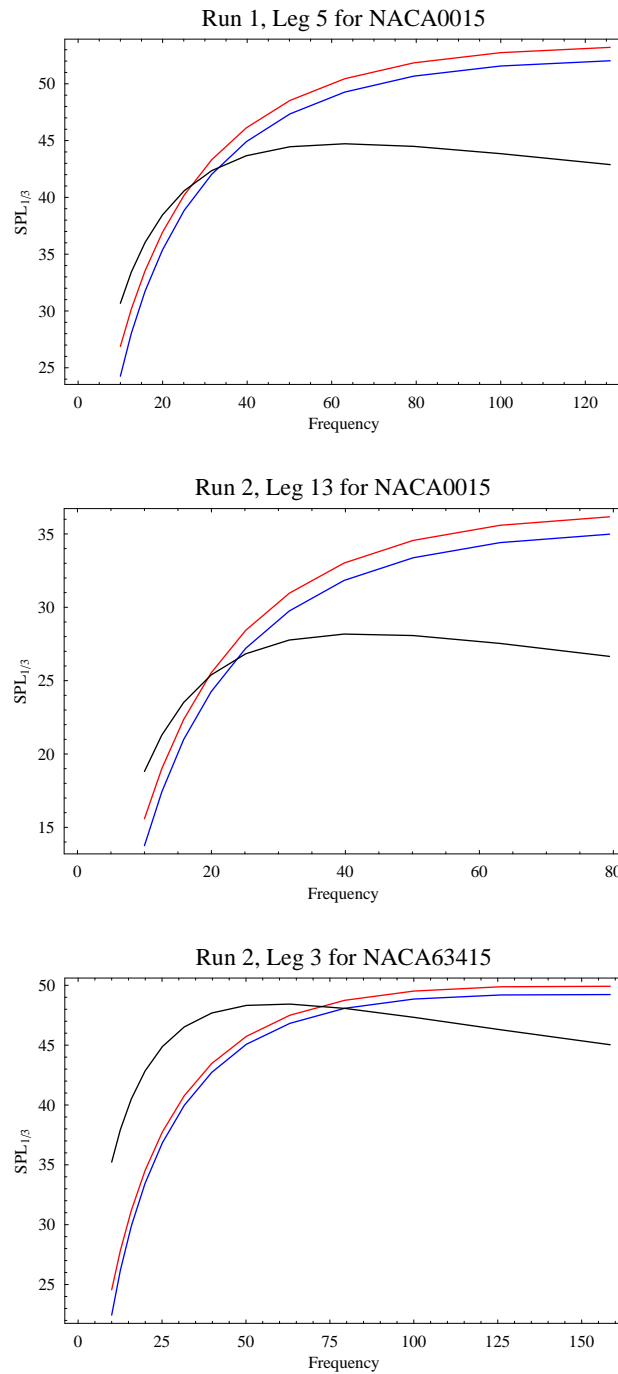where z is the height, κ_K is the von Kármán constant which is $\kappa_K = 0.4$,

Figure 4.13: Plot of the $\mathrm{SPL}_{1/3}$ at the one third octave frequencies. The 1-D model is represent by red, 1-D model is blue, and the original model (Eqn. (2.153)) is black. The turbulence parameters, $\mathcal{L}$ and ϵ, and the mean wind speed, U, are taken at runs and legs given in the plot label, see Tables 4.1, 3.4, and 3.8. The legs are chosen as close to zero mean lift conditions as possible.
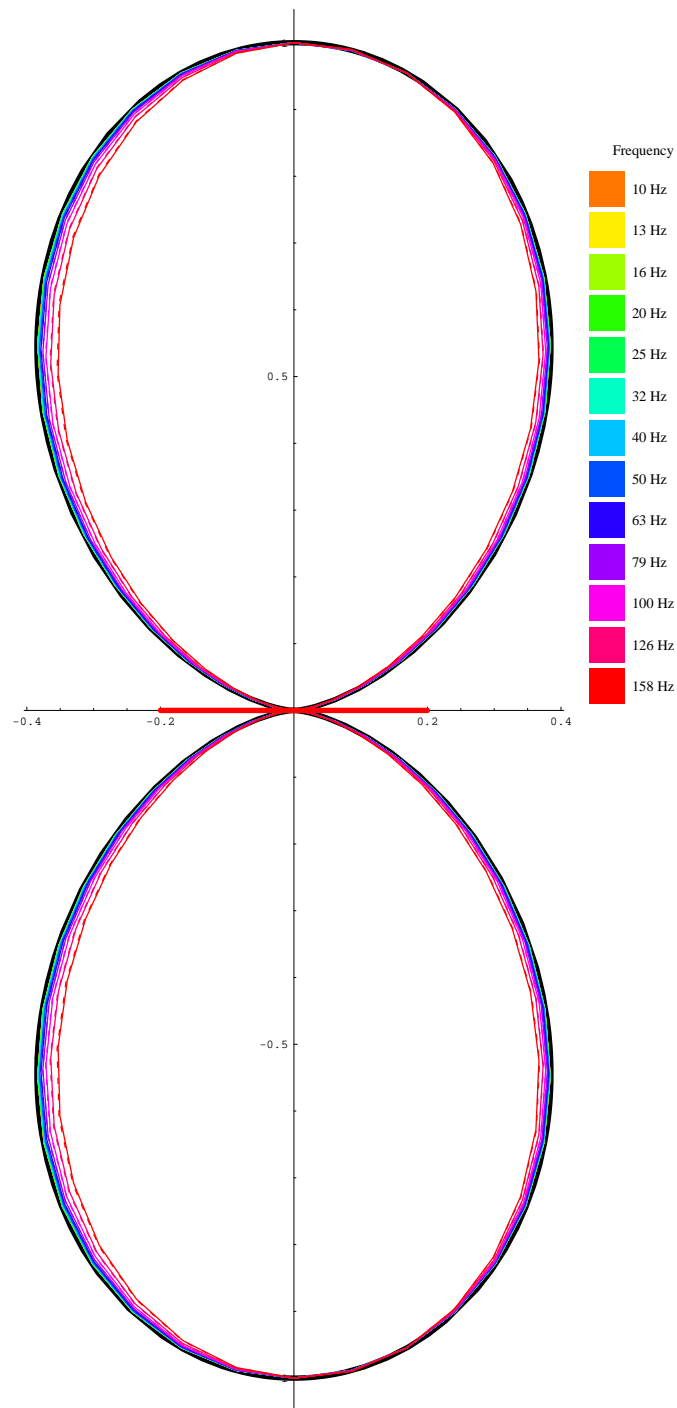
Figure 4.14: Polar plot of the SPL chordwise and vertical of an flat aerofoil. The SPL is normalized with the value vertical of mid chord. The values at the axes are the fraction of the SPL at the position to the value vertical of mid chord. The SPL is calculated in a circle 10m from mid chord around the aerofoil at a given spanwise section. The black line is a perfect dipole. The colours in the legend are at different frequencies. The thick red line at the origin is the orientation of the aerofoil.

and $z_{0,R}$ is the roughness length which is set to 0.05m. This value of the roughness length is representative of grass land. The energy dissipation is estimated by the empirical law

$$\epsilon = \frac{u_*^3}{\kappa_K z} \qquad (4.14)$$

and the characteristic length scale of the turbulence, L, is set to be equal to the hub height. The standard deviation of the wind speed, σ_u, is found by (Panofsky and Dutton 1984)

$$\sigma_u = 2.4 u_* \qquad (4.15)$$

and the relative wind speed a wind turbine blade reacts on, U_{wt} is set to 80m/s which is a typical tip speed of a wind turbine. The turbulence intensity of the wind at the blade is then

$$I_{wt} = \frac{\sigma_u}{U_{wt}}. \qquad (4.16)$$

When these parameters are estimated then Eqns. (2.153), (2.135), and (2.151) can be utilized. Figure 4.15 shows the SPL for a wind turbine with parameters as given above. The 1-D model and the 3-D model have lower SPL than the original model by Amiet (1975) at frequencies below $\sim$25Hz and have higher SPL otherwise. This is similar properties as seen in Figure 4.13.

4.5   Bridge Deck Simulation

The data obtained from a model of a bridge deck are introduced in Chapter 3. The data are analyzed and compared with the approximation of Graham (1970) by Mugridge (1971) in Larose (1997). The data are in this section compared with the 3-D model by Graham (1970) which is physically based whereas Mugridge (1971) is a mathematical approximation of the physics in Graham (1970). The admittance and the co-coherence is compared with data.

The admittance is given by

$$A_d(k_x) = \frac{1}{4\pi^2 A^2(\rho, c, U)} \frac{S_L(k_x)}{\Phi_{ww}(k_x)} \qquad (4.17)$$

where $S_L(k_x)$ is given by Eqns. (2.97) and (2.83) and normalized and non-dimensionalized with $4\pi^2 A^2(\rho, c, U)$. This quantity is normalized with the
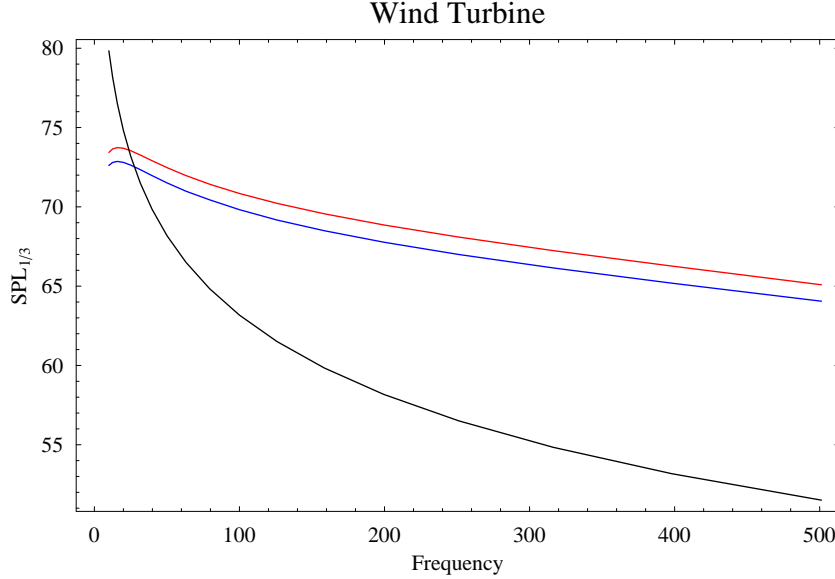
Figure 4.15: Plot of the $\mathrm{SPL}_{1/3}$ at the one third octave frequencies. The 1-D model is represented by red, 3-D model is blue, and the original model (Eqn. (2.153)) is black. The turbulence parameters, $\mathcal{L}$ and ϵ, and the mean wind speed, U, are calculated for representative conditions for a wind turbine.

vertical energy spectrum given by Eqn. (2.114). It describes how large a fraction of the turbulent energy is used to generate lift fluctuations.

The comparison of Eqn. (4.17) against data is seen in Figure 4.16. Eight different conditions of turbulence and width of bridge deck are plotted. The 3-D model is systematically below the data whereas the approximation by Mugridge (1971) is over predicting the data at small wave numbers and under predicting for large wave numbers. The 3-D model is expected to be lower than the data from Figures 4.10 to 4.12.

The cross spectrum between sections of the profile separated by a distance Δy is given by

$$\chi_{LL}(k_x, \Delta y) = 2A^2(\rho, c, U) \int_0^\infty \Phi_{ww}(k_x, k_y)|g(k_x B/2, k_y B/2)|^2 \cos(k_y \Delta y) dk_y$$
(4.18)

where $g(k_x B/2, k_y B/2)$ is given by Eqn. (2.83) and B is the width of the section of the bridge (chord length). The imaginary part vanishes in the cross spectrum of the lift fluctuations because it is an uneven function in k_y. Then the co-coherence is found as the fraction of the absolute value of the cross spectrum of the lift fluctuations at two sections separated with Δy over the
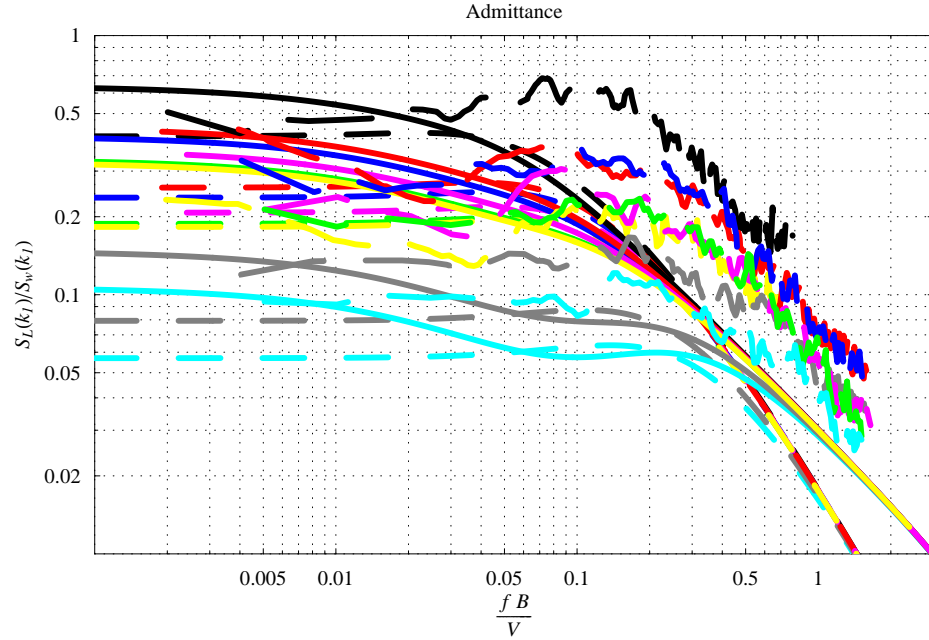
Figure 4.16: Comparison of the lift admittance from data from Larose (1997) (long dashed lines) with models by Mugridge (1971) (full lines) and Graham (1970) (short dashed lines) at different width of a bridge deck and different length scales of turbulence. Eight different setups are plotted. The red line indicates: L=0.43m, B=0.30m, $\mathcal{L}_w$/B=0.80, Magenta: L =0.43m, B=0.38m, $\mathcal{L}_w$/B=0.63, Black: L=0.39m, B=0.15m, $\mathcal{L}_w$/B=1.50, Blue: L=0.39m, B=0.30m, $\mathcal{L}_w$/B=0.73, Green: L=0.39m, B=0.38m, $\mathcal{L}_w$/B=0.58, Yellow: L=.15m, B=.15m, $\mathcal{L}_w$/B=0.57, Gray: L =0.15m, B=0.30m, $\mathcal{L}_w$/B=0.29, and Cyan: L=.15m, B=.38m, $\mathcal{L}_w$/B=0.23, where L is the length scale in Eqn. (2.111) common to the three velocity components, B is the width of the bridge deck, $\mathcal{L}_w$ is the length scale of the w-component defined as $\mathcal{L}_w = 0.561L$ according to Eqn. (20), p. 107 in Larose (1997), see also Table 8 in Larose (1997), p. 107. This plot can be compared to the figure in Larose (1997), p. 115.

auto spectrum of the lift fluctuations

$$coh_{LL}^{1/2}(k_x) = \frac{|\chi_{LL}(k_x, \Delta y)|}{S_L(k_x)}. \tag{4.19}$$

This gives a measure of the correlation of the lift fluctuations at two strips normalized with the auto spectrum. The co-coherence for the vertical component of the wind is given by Eqn. (2.117).

The co-coherence is seen in Figure 4.17. The figure shows the co-coherence

of the lift at six different separation distances at two different turbulence conditions. The co-coherence of the w-component is also shown. It is seen that at low separation distances, Δy of 0.03 and 0.06, the data are close to $coh_w^{1/2}(k_x)$. The 3-D model by Graham (1970) describes the data quite well at separation distances, Δy, of 0.13, 0.16, 0.24, and 0.30. The model predicts the difference between the two setups and is in the vicinity of data for large separation distances.

The reality as represented by the data does not respond instantly as the physics in the 3-D model predicts. The co-coherence gives a picture of how the pressure difference in spanwise direction is equalized. For the two low separation distances the co-coherence of lift data is closer to the co-coherence of the w-component. This indicates that the pressure differences on the bridge deck are not equalized instantly but needs a longer distance to react.

The physical 3-D model captures the features seen in the data, although the model under predicts the admittance systematically. The co-coherence of the lift is well predicted for large separation distances.

4.6   Conclusions Regarding Analysis

Data have in this Section been analyzed and compared to models. The data fall between the 1-D model by Sears (1941) and the 3-D model by Graham (1970) when looking at the lift spectra. These two models seem to underestimate the data systematically when looking at the pressure spectra.

The pressure data from the microphones are not useful below a frequency of 10 Hz because of the dimension of the microphone. The 3-D model gives numerically reasonable values in the interval $\kappa \equiv \frac{k_x c}{2} \in [0; 20]$ and $\nu \equiv \frac{k_y c}{2} \in [0; 15]$. This gives an upper limit for the frequencies that can be compared. This upper limit is dependent on the mean wind speed.

The pressure spectra of the data are underestimated by the models. This may be due to the properties of the wind tunnel. The *wind tunnel is not anechoic* and thus the background noise is suspected to be seen in the pressure data. The models are systematically around one decade below the data and further the pressure spectra of data and models have the same behavior.

The spectra of the lift fluctuations derived from the data are in between the spectra of the lift fluctuations by the 1-D model and the 3-D model. This result gives reason to believe that the systematic error in the pressure spectra is due to the background noise of aerodynamical and maybe acoustical origin. This background noise seems to be filtered out when the lift fluctuations are estimated.
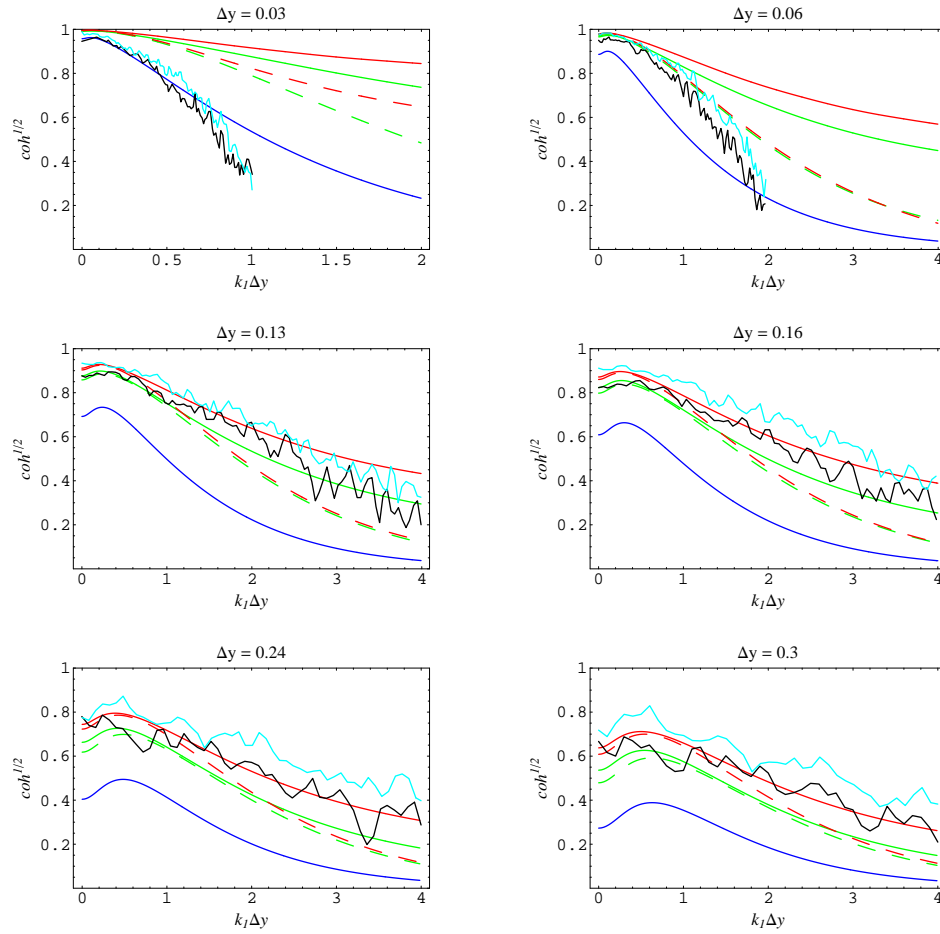
Figure 4.17: The square root of the coherence (co-coherence) of the lift at different spanwise separation distances and two different conditions of turbulence. Data from Larose (1997) (cyan and black lines) is compared with models by Mugridge (1971) (dashed lines) and Graham (1970) (full lines) . Red and cyan are for $\mathcal{L}_w/\text{B}= 0.73$, green and black are for $\mathcal{L}_w/\text{B}= 1.50$, see also Table 8 in Larose (1997), p. 107. The co-coherence of the vertical wind component, w, is shown with a blue line. This plot can be compared to the figures in Larose (1997), pp. 117 and 118.

There are reasons to believe that the SPL from data would fall in between the SPL's from the 1-D model and 3-D model. The reason for this statement is, that the lift fluctuations from data are in between models and because the lift distribution is integrated over the aerofoil to obtain an estimate of

the SPL. The acoustic model have dipole like structure but the dipole is squeezed. The squeezing is dependent on frequency, the higher frequency the more squeezing.

The 3-D model is able to predict reasonable the co-coherence of the lift fluctuations from the pressure data of a bridge deck simulation. The 3-D model systematically under predicts the admittance of the bridge deck simulation data.

Chapter 5

Conclusion

Three different models for predicting the fluctuating lift on an aerofoil have been described. These models of lift have been tested against data. The lift distribution is presented for the 1-D model and is developed for the 3-D model. These two models of lift distribution are tested against pressure data. They are also used to predict SPL.

Data are obtained for two different aerofoils. Profiles of a NACA0015 and a NACA63415 are used to obtain pressure data at the surface of aerofoil. Surface pressure obtained by microphones is tested against models for the lift distribution which in this case are the 1-D model and the 3-D model. The surface pressure data by microphones are integrated numerically to obtain the fluctuating lift. These derived data are tested against models for lift in this case all three models.

The surface pressure are also obtained by pressure holes and these data are able to describe mean pressures at chord wise positions reliably. The pressure hole data are therefore used to get angles of attack of which the mean flow impinges the aerofoil.

The mean wind speeds are obtained from 5-hole pitot tube data and these data are only obtained at the experiment with NACA0015. The data from the 5-hole pitot tube are used in similar conditions for the experiment with a NACA63415 profile. The mean wind speed data are used to get the magnitude of the lift and the lift distribution fluctuations from models in the further analysis.

Data from a triple wired hot wire are used to get information of the turbulence. The turbulence is close to be isotropic. The turbulence data are used to estimate the length scale of the turbulence and the energy dissipation of the turbulence.

The comparison of data and models seems to be similar for the two aerofoils. The conclusion is that the models predict the different aerofoils equally.

It is assumed reasonable that the lift fluctuations from data are in between the 1-D model and the 3-D model because the former model by Sears (1941) does not include spanwise effects from the turbulence, but the latter model by Graham (1970) does. The lift fluctuations from data were expected to be closer to the 3-D model because spanwise effects of the vertical gust are included. An explanation that this is not the case is the quality of the pressure data obtained by microphones. The calculated lift from data are similar for different angle of attacks and thus the 2-D model is not able to describe the data. Further the difference between pressure spectra of models and data is systematic which highly probably is because of background noise of aerodynamical and acoustical origin in the wind tunnel. The models of the lift indicate that noise from a wind turbine due to atmospheric turbulence may be the most dominant according to the acoustical model by Amiet (1975). The lift spectra and pressure spectra suggest that sound pressure level of data will be between sound pressure level based on the 1-D model and sound pressure level based on the 3-D model. The acoustical model may need more work to be validated. It was not possible to test the acoustical model by the measurements presented in this work.

The sound pressure level of data are not found because the spatial resolution of surface pressure by microphones on the aerofoils did not allow this.

The aerodynamical model by Graham (1970) is compared to pressure data obtained from a model of a bridge section (Larose 1997). This comparison shows that the model by Graham (1970) describes well the spanwise variations in terms of the co-coherence of the lift. This is expected because the aerodynamical model includes spanwise as well as chordwise variations of the vertical gust.

Appendix A

Bessel Functions

Bessel functions are used in the analysis of aerofoil theory for solving various problems like integrals and exponential relations.

A.1 Bessel Functions of First Kind

Bessel functions of the first kind, $J_\nu(z)$, satisfy the differential equation (McLachlan 1955)

$$\frac{d^2 J_\nu(z_v)}{dz_v^2} + \frac{1}{z_v}\frac{d J_\nu(z_v)}{dz_v} + \left(1 - \frac{\nu^2}{z_v^2}\right) J_\nu(z_v) = 0. \qquad (A.1)$$

In the above ν is the order of the Bessel function, it can be any real number. The order will be an integer only, when n is used. Bessel functions can be defined in various ways. The original definition by Bessel is (McLachlan 1955)

$$J_\nu(z_v) = \frac{1}{2\pi}\int_0^{2\pi} \cos(\nu\theta - z_v\sin\theta)d\theta. \qquad (A.2)$$

In this text the definition

$$J_\nu(z_v) = \sum_{m=0}^{\infty} \frac{(-1)^m(\frac{z_v}{2})^{2m+\nu}}{m!\Gamma(m+\nu+1)} \qquad (A.3)$$

which has an infinite convergence radius will be used. It is easily verified that Eqn. (A.3) is a solution to Eqn. (A.1) by equating terms of equal order. A useful relation is obtained if the products $z_v^\nu J_\nu(z_v)$ and $z_v^{-\nu} J_\nu(z_v)$

are differentiated with respect to z_v.

$$d\{z_v^\nu J_\nu(z_v)\}/dz_v = d\{\sum_{m=0}^\infty \frac{(-1)^m(z_v)^{2m+2\nu}}{2^{2m+\nu}m!\Gamma(m+\nu+1)}\}/dz_v$$

$$z_v^\nu J_\nu'(z_v) + \nu z_v^{\nu-1} J_\nu(z_v) = \sum_{m=0}^\infty \frac{(2m+2\nu)(-1)^m(z_v)^{2m+2\nu-1}}{2^{2m+\nu}m!\Gamma(m+\nu+1)}$$

$$= \sum_{m=0}^\infty \frac{(-1)^m(z_v)^{2m+2\nu-1}}{2^{2m+\nu-1}m!\Gamma(m+\nu+1-1)}$$

$$= z_v^\nu J_{\nu-1}(z_v)$$

$$\Leftrightarrow J_\nu'(z_v) + \frac{\nu}{z_v}J_\nu(z_v) = J_{\nu-1}(z_v) \tag{A.4}$$

where a prime means differentiation with respect to z_v. Further the relation $\Gamma(m+\nu+1) = (m+\nu)\Gamma(m+\nu)$ is used (McLachlan 1955). $\Gamma(m)$ is the Gamma function with argument m. Similarly

$$d\{z_v^{-\nu} J_\nu(z_v)\}/dz_v = d\{\sum_{m=0}^\infty \frac{(-1)^m(z_v)^{2m}}{2^{2m+\nu}m!\Gamma(m+\nu+1)}\}/dz_v$$

$$z_v^{-\nu} J_\nu'(z_v) - \nu z_v^{-\nu-1} J_\nu(z_v) = \sum_{m=1}^\infty \frac{2m(-1)^m(z_v)^{2m-1}}{2^{2m+\nu}m!\Gamma(m+\nu+1)}, \ m = r+1$$

$$= z_v^{-\nu} \sum_{r=0}^\infty \frac{(-1)^{r+1}(z_v)^{2r+\nu+1}}{2^{2r+\nu+1}r!\Gamma(r+(\nu+1)+1)}$$

$$= -z_v^{-\nu} J_{\nu+1}(z_v)$$

$$\Leftrightarrow J_\nu'(z_v) - \frac{\nu}{z_v}J_\nu(z_v) = -J_{\nu+1}(z_v) \tag{A.5}$$

can be derived. When Eqn. (A.5) is subtracted from Eqn. (A.4) then

$$2\frac{\nu}{z_v}J_\nu(z_v) = J_{\nu-1}(z_v) + J_{\nu+1}(z_v) \tag{A.6}$$

is obtained. From Eqn. (A.3) it is easily seen that

$$J_\nu(-z_v) = (-1)^\nu J_\nu(z_v). \tag{A.7}$$

When the Bessel function of the first kind has an imaginary argument, $J_\nu(\imath z_v)$, it will satisfy

$$\frac{d^2 J_\nu(\imath z_v)}{dz_v^2} + \frac{1}{z_v}\frac{dJ_\nu(\imath z_v)}{dz_v} - \left(1 + \frac{\nu^2}{z_v^2}\right)J_\nu(\imath z_v) = 0. \tag{A.8}$$

From the definition Eqn. (A.3) it is seen, when z_v is substituted with $\imath z_v$, that

$$J_\nu(\imath z_v) = e^{\imath \pi \nu / 2} \sum_{m=0}^{\infty} \frac{\left(\frac{z_v}{2}\right)^{2m+\nu}}{m! \Gamma(m + \nu + 1)} \tag{A.9}$$

where it is seen that the series itself satisfy Eqn. (A.8) because only the series have z_v-dependence.

A.2 Bessel Functions of Second and Third Kind

The Bessel function of second for integer order, n, is defined as

$$Y_n = \left[\frac{\partial}{\partial \nu} \left\{ \cos \nu \pi J_\nu(z_v) - J_{-\nu}(z_v) \right\} \bigg/ \frac{\partial}{\partial \nu} \sin \nu \pi \right]_{\nu = n} \tag{A.10}$$

which by differentiating Eqn. (A.3) with respect to ν can be shown to be (McLachlan 1955)

$$
\begin{aligned}
Y_n(z_v) \;=\; & \frac{2}{\pi} \ln \left(\frac{z_v}{2} \right) J_n(z_v) - \frac{1}{\pi} \sum_{r=0}^{n-1} \frac{n-r-1)!}{r!} \left(\frac{2}{z_v} \right)^{n-2r} \\
& - \frac{1}{\pi} \sum_{r=0}^{\infty} \frac{(-1)^r \left(\frac{z_v}{2} \right)^{n+2r} \left[\psi(n+r+1) + \psi(r+1) \right]}{r!(n+r)!}, \; n \ge 1
\end{aligned}
\tag{A.11}
$$

where

$$\psi(m+1) = \sum_{i=1}^{\infty} \left(\frac{1}{i} - \frac{1}{m+i} \right) - \gamma, \; m > 0, \; \psi(1) = -\gamma. \tag{A.12}$$

where γ is Euler's constant. When the order is zero then

$$Y_0(z_v) = \frac{2}{\pi} \left\{ \gamma + \ln \left(\frac{z_v}{2} \right) \right\} J_0(z_v) - \frac{2}{\pi} \sum_{r=1}^{\infty} \left\{ \frac{(-1)^r \left(\frac{z_v}{2} \right)^{2r}}{(r!)^2} \sum_{i=1}^{r} \frac{1}{i} \right\} \tag{A.13}$$

The order, n, is zero or a positive integer in this thesis. The Bessel function of second kind is used to define the Hankel functions (Bessel functions of third kind) which are complex functions defined as

$$
\begin{aligned}
H_n^{(1)}(z_v) &= J_n(z_v) + \imath Y_n(z_v) \tag{A.14} \\
H_n^{(2)}(z_v) &= J_n(z_v) - \imath Y_n(z_v) \tag{A.15}
\end{aligned}
$$

where n is an integer. The Hankel function, $H_n^{(1)}(z_v)$, is used in Section 2.1.3 for orders $n = 0$ and $n = 1$.
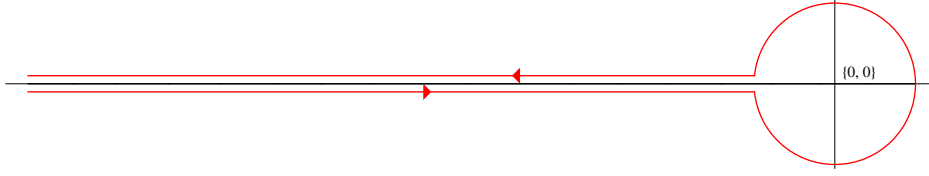
Figure A.1: The integration path is running from $-\infty$ just below the real axis to 0 and then around zero at the positive side and then to $-\infty$ just above the real axis.

A.3   Modified Bessel Functions of First Kind

The modified Bessel function of the first kind is defined from Eqn. (A.9) as

$$I_\nu(z_v) = \sum_{m=0}^{\infty} \frac{\left(\frac{z_v}{2}\right)^{2m+\nu}}{m!\Gamma(m+\nu+1)} \tag{A.16}$$

and is a real function. This can be rewritten, when the relation (Watson 1952)

$$\frac{1}{\Gamma(m+\nu+1)} = \frac{1}{2\pi\imath}\int_{-\infty}^{0+} t^{-\nu-m-1}e^t dt \tag{A.17}$$

is used, as

$$I_\nu(z_v) = \sum_{m=0}^{\infty}\left(\frac{\left(\frac{z_v}{2}\right)^{2m+\nu}}{m!}\frac{1}{2\pi\imath}\int_{-\infty}^{0+} t^{-\nu-m-1}e^t dt\right). \tag{A.18}$$

The integral in Eqn. (A.17) is a contour integral with the integration path sketched in Figure A.1. The relation in Eqn. (A.17) is valid for all values of ν. The integrand in Eqn. (A.17) is analytical except at the real axis from 0 to $-\infty$ where it has a branch cut. This allows to choose the integration path in a more convenient way, because it is in an analytical domain. This will be evident later. Because the series in Eqn. (A.3) is uniform convergent then also Eqn. (A.16) is uniform convergent. This property allows to interchange
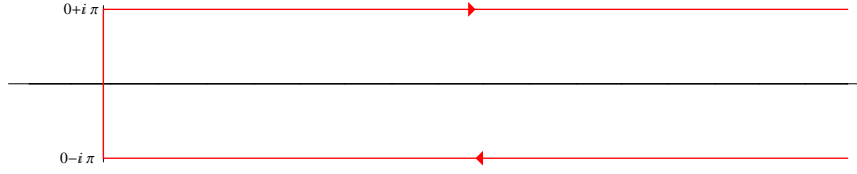
Figure A.2: The integration path with the substitution $u = e^w$ becomes from $\infty - \imath\pi$ to $-\imath\pi$, then along the imaginary axis from $-\imath\pi$ to $\imath\pi$ and from this point to $\infty + \imath\pi$.

the order of summation and integration, thus

$$
\begin{aligned}
I_\nu(z_v) &= \frac{1}{2\pi\imath} \left(\frac{z_v}{2}\right)^\nu \int_{-\infty}^{0+} \left(\sum_{m=0}^{\infty} \frac{(\frac{z_v}{2})^{2m}}{m!} t^{-\nu-m-1} e^t\right) dt \\
&= \frac{1}{2\pi\imath} \left(\frac{z_v}{2}\right)^\nu \int_{-\infty}^{0+} \left(\sum_{m=0}^{\infty} \frac{(\frac{z_v^2}{4t})^{m}}{m!} t^{-\nu-1} e^t\right) dt \\
&= \frac{1}{2\pi\imath} \left(\frac{z_v}{2}\right)^\nu \int_{-\infty}^{0+} \exp\left(\frac{z_v^2}{4t} + t\right) t^{-\nu-1} dt \\
&= \frac{1}{2\pi\imath} \left(\frac{z_v}{2}\right)^\nu \int_{-\infty}^{0+} \exp\left[\frac{z_v}{2}\left(\frac{z_v}{2t} + \frac{2t}{z_v}\right)\right] t^{-\nu-1} dt \\
&= \frac{1}{2\pi\imath} \int_{-\infty}^{0+} \exp\left[\frac{z_v}{2}\left(u + \frac{1}{u}\right)\right] u^{-\nu-1} du \qquad \text{(A.19)}
\end{aligned}
$$

where the definition

$$
e^x = \sum_{m=0}^{\infty} \frac{x^m}{m!} \qquad \text{(A.20)}
$$

is used McLachlan (1955). The substitution $u = \frac{2t}{z_v}$ is linear and does not alter the limits of the integration. The integration path is merely stretched. Furthermore $dt = \frac{z_v}{2} du$ which leads to the expression in Eqn. (A.19). The substitution $u = e^w$ alters the integration path in Figure A.1 to the integration path sketched in Figure A.2. Further when the substitution is $u = e^w$ then $du = e^w dw$. The modified Bessel function then becomes

$$
I_\nu(z_v) = \frac{1}{2\pi\imath} \int_{\infty-\imath\pi}^{\infty+\imath\pi} \exp\left(z_v \cosh w - \nu w\right) dw, \qquad \text{(A.21)}
$$

where the definition

$$
\cosh x = \frac{1}{2}\left(e^x + e^{-x}\right) \qquad \text{(A.22)}
$$

is used. This integral can be evaluated along each of the three parts to give

$$
\begin{aligned}
I_\nu(z_v) \;=\; & \frac{1}{\pi} \int_0^\pi \exp\left(z_v \cos\theta\right) \cos\nu\theta \, dw \\
& -\frac{\sin\nu\pi}{\pi} \int_0^\infty \exp\left(-z_v \cosh w - \nu w\right) dw
\end{aligned}
\tag{A.23}
$$

where the relations

$$
\sin x \;=\; -\sin(-x) \tag{A.24}
$$

$$
\cos x \;=\; \cos(-x) \tag{A.25}
$$

$$
\cos x \;=\; \frac{1}{2}\left(e^{\imath x} + e^{-\imath x}\right) \tag{A.26}
$$

$$
\sin x \;=\; \frac{1}{2\imath}\left(e^{\imath x} - e^{-\imath x}\right) \tag{A.27}
$$

$$
\cosh \imath x \;=\; \cos x \tag{A.28}
$$

$$
\int_{-x}^{x} f(x)dx \;=\; 2\int_0^x f(x)dx, \;\; f(x) \text{ is even} \tag{A.29}
$$

are used. Further is utilized that the product of two even functions is even and thus is nonzero when integrated from $-\pi$ to π and the product of an even and an uneven function is uneven and thus is 0 when integrated from $-\pi$ to π. The first term on the righthand side in Eqn. (A.23) is due to the integration along the imaginary axis, and the second term is due to the integration paths parallel to the real axis.

A.4   Modified Bessel Functions of Second Kind

The modified Bessel function of the second kind, $K_\nu(z_v)$, is defined as

$$
K_\nu(z_v) = \frac{\pi}{2} \frac{I_{-\nu}(z_v) - I_\nu(z_v)}{\sin\nu\pi}. \tag{A.30}
$$

This function is obviously also a solution to Eqn. (A.8) because it is a linear combination of modified Bessel functions of the first kind, and these are solutions to Eqn. (A.8). The reason to define a modified Bessel function of the second kind is to have a function which behaves nicely (goes to zero) at infinity but has a singularity at 0, where $I_\nu(z_v)$ is 0 at $z_v = 0$ and goes monotonically to ∞ for $z_v \rightarrow \infty$. When the order of $K_\nu(z_v)$ is an integer then it is defined as

$$
K_n(z_v) = \lim_{\nu \to n} \frac{\pi}{2} \frac{I_{-\nu}(z_v) - I_\nu(z_v)}{\sin\nu\pi}. \tag{A.31}
$$

It is defined as this because

$$
\begin{aligned}
I_{-n}(z_v) &= \sum_{m=n}^{\infty} \frac{\left(\frac{z_v}{2}\right)^{2m-n}}{m!(m-n)!}, \; r = m - n \\
&= \sum_{r=0}^{\infty} \frac{\left(\frac{z_v}{2}\right)^{2r+n}}{(r+n)!r!} \\
&= I_n(z_v)
\end{aligned} \tag{A.32}
$$

and $\sin n\pi = 0$ for n an integer. The lower limit in the summation in the first equality above is due to $\Gamma(t)$ goes to infinity when $t \leq 0$ and t is an integer, and does not contribute to the sum. The modified Bessel function of the first kind with negative order becomes, when interchanging ν with $-\nu$ in Eqn. (A.23)

$$
\begin{aligned}
I_{-\nu}(z_v) &= \frac{1}{\pi} \int_0^{\pi} \exp\left(z_v \cos \theta\right) \cos \nu\theta dw \\
&+ \frac{\sin \nu\pi}{\pi} \int_0^{\infty} \exp\left(-z_v \cosh w + \nu w\right) dw
\end{aligned} \tag{A.33}
$$

where Eqn. (A.24) and Eqn. (A.25) is utilized. This operation is legal because Eqn. (A.17) is valid for all ν. Then the modified Bessel function of the second kind becomes

$$
K_\nu(z_v) = \int_0^{\infty} \exp\left(-z_v \cosh w\right) \cosh(\nu w) dw. \tag{A.34}
$$

This representation of $K_\nu(z_v)$ is valid for all values of ν because $\cosh(\nu w)$ is continuous for all values of ν and thus satisfies Eqn. (A.31). This leads to

$$
K_0(z_v) = \int_0^{\infty} \exp\left(-z_v \cosh w\right) dw. \tag{A.35}
$$

The variable w in Eqn. (A.35) can be substituted as $t = \cosh w$ and $dw = \frac{dt}{\sqrt{t^2-1}}$, further the limits of integration changes. Thus

$$
K_0(z_v) = \int_1^{\infty} \frac{e^{-z_v t}}{\sqrt{t^2 - 1}} dt \tag{A.36}
$$

which becomes, when z_v is substituted with $\imath z_v$,

$$
K_0(\imath z_v) = \int_1^{\infty} \frac{e^{-\imath z_v t}}{\sqrt{t^2 - 1}} dt. \tag{A.37}
$$

This substitution is allowed because of the definition of $I_\nu(z_v)$ in Eqn. (A.9).

In a similar way as in Eqn. (A.4) and Eqn. (A.5) it can be shown that

$$I'_\nu(z_v) = \frac{\nu}{z_v}I_\nu(z_v) + I_{\nu+1}(z_v) \tag{A.38}$$

$$I'_{-\nu}(z_v) = \frac{\nu}{z_v}I_{-\nu}(z_v) + I_{-(\nu+1)}(z_v) \tag{A.39}$$

$$I'_\nu(z_v) = \frac{-\nu}{z_v}I_\nu(z_v) + I_{\nu-1}(z_v) \tag{A.40}$$

$$I'_{-\nu}(z_v) = \frac{-\nu}{z_v}I_{-\nu}(z_v) + I_{-(\nu-1)}(z_v). \tag{A.41}$$

Differentiating Eqn. (A.30) with respect to z_v, the following relation is obtained

$$\frac{d}{dz_v}K_\nu(z_v) = \frac{d}{dz_v}\left(\frac{\pi}{2}\frac{I_{-\nu}(z_v) - I_\nu(z_v)}{\sin\nu\pi}\right)$$

$$\Leftrightarrow K'_\nu(z_v) = \frac{\pi}{2}\frac{I'_{-\nu}(z_v) - I'_\nu(z_v)}{\sin\nu\pi}$$

$$= \frac{\nu}{z_v}\frac{\pi}{2}\frac{I_{-\nu}(z_v) - I_\nu(z_v)}{\sin\nu\pi} + \frac{\pi}{2}\frac{I_{-\nu-1}(z_v) - I_{\nu+1}(z_v)}{\sin\nu\pi}$$

$$= \frac{\nu}{z_v}K_\nu(z_v) - \frac{\pi}{2}\frac{I_{-(\nu+1)}(z_v) - I_{\nu+1}(z_v)}{\sin(\nu+1)\pi}$$

$$= \frac{\nu}{z_v}K_\nu(z_v) - K_{\nu+1}(z_v) \tag{A.42}$$

where

$$\sin(\theta \pm \phi) = \sin\theta\cos\phi \pm \cos\theta\sin\phi \tag{A.43}$$

is used. Eqn. (A.43) can be derived from $e^{\imath(\theta\pm\phi)}= e^{\imath\theta}e^{\pm\imath\phi}$ by equating the imaginary parts. Similarly $\cos(\theta \pm \phi)$ can be expanded by equating the real parts. Similarly as Eqn. (A.42)

$$K'_\nu(z_v) = -\frac{\nu}{z_v}K_\nu(z_v) - K_{\nu-1}(z_v) \tag{A.44}$$

is derived.

When $\nu = 0$ in Eqn. (A.42) then

$$K'_0(z_v) = -K_1(z_v). \tag{A.45}$$

This relation can be used when Eqn. (A.37) is differentiated with respect to $\imath z$ to give

$$\frac{dK_0(\imath z_v)}{d\imath z_v} = \int_1^\infty \frac{-te^{-\imath z_v t}}{\sqrt{t^2 - 1}}dt = -K_1(\imath z_v). \tag{A.46}$$

Further Eqn. (A.44) gives

$$\frac{dK_1(\imath z_v)}{d\imath z_v} = \int_1^\infty \frac{-t^2 e^{-\imath z_v t}}{\sqrt{t^2 - 1}} dt = -\frac{1}{\imath z_v} K_1(\imath z_v) - K_0(\imath z_v). \tag{A.47}$$

The results of Eqn. (A.37), Eqn. (A.46), and Eqn. (A.47) are used when the lift distribution for a 1-D sinusoidal gust on a flat plate is analyzed.

A.5   Generating Function for Bessel Functions

When Eqn. (A.20) is utilized then

$$\begin{aligned}
\exp\left[\frac{z_v}{2}\left(t - \frac{1}{t}\right)\right] &= \left(\sum_{r=0}^\infty \frac{\left(\frac{z_v t}{2}\right)^r}{r!}\right)\left(\sum_{m=0}^\infty \frac{\left(\frac{-z_v}{2t}\right)^m}{m!}\right) \\
&= \sum_{r=0}^\infty \left(\sum_{m=0}^\infty \frac{\left(\frac{z_v t}{2}\right)^r \left(\frac{-z_v}{2t}\right)^m}{r! m!}\right), \; n = r - m \\
&= \sum_{n=-\infty}^\infty \left(\sum_{m=0}^\infty \frac{(-1)^m \left(\frac{z_v}{2}\right)^{2m+n} t^n}{m!(n+m)!}\right) \\
\exp\left[\frac{z_v}{2}\left(t - \frac{1}{t}\right)\right] &= \sum_{n=-\infty}^\infty t^n J_n(z_v) \tag{A.48}
\end{aligned}$$

where in the last equality the definition Eqn. (A.3) is used. Note that $\Gamma(m + \nu + 1) = (m + \nu)!$ when ν is an integer (McLachlan 1955). The exponential function in Eqn. (A.48) is called the generating function for Bessel functions for obvious reasons. A substitution of $t = e^{\imath\theta}$ gives

$$e^{\imath z_v \sin\theta} = \sum_{n=-\infty}^\infty e^{\imath n\theta} J_n(z_v). \tag{A.49}$$

This relation is useful when the following

$$\begin{aligned}
J_{-n}(z_v) &= \sum_{m=n}^\infty \frac{(-1)^m \left(\frac{z_v}{2}\right)^{2m-n}}{m!(m-n)!}, \; r = m - n \\
&= \sum_{r=0}^\infty \frac{(-1)^{r+n}\left(\frac{z_v}{2}\right)^{2r+n}}{(r+n)! r!} \\
&= (-1)^n J_n(z_v) \tag{A.50}
\end{aligned}$$

and the relations Eqn. (A.24) and Eqn. (A.25) is used. Now Eqn. (A.49) becomes, when the real parts and imaginary parts are separated

$$\cos(z_v \sin \theta) + i \sin(z_v \sin \theta) = J_0(z_v) + 2 \sum_{n=1}^{\infty} J_{2n}(z_v) \cos 2n\theta$$

$$+ 2i \sum_{n=1}^{\infty} J_{2n-1}(z_v) \sin(2n-1)\theta. \, (A.51)$$

Further $\sin(\frac{\pi}{2} - \phi) = \cos \phi$ from Eqn. (A.43) then with the substitution $\theta = \frac{\pi}{2} - \phi$ Eqn. (A.51) can be rewritten as

$$e^{iz_v \cos \phi} = J_0(z_v) + 2 \sum_{n=1}^{\infty} (-1)^n J_{2n}(z_v) \cos 2n\phi$$

$$+ 2i \sum_{n=1}^{\infty} (-1)^{n+1} J_{2n-1}(z_v) \cos(2n-1)\phi$$

$$= J_0(z_v) + 2 \sum_{m=1}^{\infty} i^m J_m(z_v) \cos m\phi \qquad (A.52)$$

where Eqn. (A.43) and

$$\cos(\theta \pm \phi) = \cos \theta \cos \phi \mp \sin \theta \sin \phi \qquad (A.53)$$

is used.

A sinusoidal gust in 1-D can be described by Eqn. (A.52).

Appendix B

Auxiliary Functions

The function

$$\frac{(-1)^n}{(-x + \sqrt{x^2 - 1})^n} = \frac{(-1)^n (x + \sqrt{x^2 - 1})^n}{((-x + \sqrt{x^2 - 1})(x + \sqrt{x^2 - 1}))^n} = (x + \sqrt{x^2 - 1})^n$$

(B.1)

is used in Eqn. (2.37) to describe the stream function upstream of a cylinder. Its derivative is

$$\frac{\partial}{\partial x}\left[(x + \sqrt{x^2 - 1})^n\right] = \frac{n}{\sqrt{x^2 - 1}}(x + \sqrt{x^2 - 1})^n$$

(B.2)

and that is used to find the acceleration. When the acceleration is integrated upstream of the aerofoil to find the velocity, then following the integral is obtained. The integral can be solved by parts as

$$\int_{-\infty}^{-1} e^{\imath k(x+1)} \frac{\partial}{\partial x}\left[(x + \sqrt{x^2 - 1})^n\right] dx$$

$$= \left[e^{\imath k(x+1)}(x + \sqrt{x^2 - 1})^n\right]_{-\infty}^{-1} - \imath k \int_{-\infty}^{-1} e^{\imath k(x+1)}(x + \sqrt{x^2 - 1})^n dx$$

$$= (-1)^n - \imath k \int_{-\infty}^{-1} e^{\imath k(x+1)}(x + \sqrt{x^2 - 1})^n dx$$

(B.3)

This is used to find (2.41) as

$$
-\frac{e^{\imath\kappa}}{U}\int_{-\infty}^{-1}\sum_{n=1}^{\infty}\frac{\partial\psi_n}{\partial x}e^{\imath\kappa x}dx = -\frac{e^{\imath\kappa}}{U}\int_{-\infty}^{-1}\sum_{n=1}^{\infty}A_n e^{\imath\kappa x}\frac{\partial}{\partial x}\left[(x+\sqrt{x^2-1})^n\right]dx
$$

$$
= -\frac{e^{\imath\kappa}}{U}\int_{-\infty}^{-1}\sum_{n=1}^{\infty}e^{\imath\kappa x}2Uwe^{\imath\omega t}\left(\frac{\imath\kappa}{2n}P_{n-1}+P_n-\frac{\imath\kappa}{2n}P_{n+1}\right)\frac{\partial}{\partial x}\left[(x+\sqrt{x^2-1})^n\right]dx
$$

$$
= -2we^{\imath\omega t}\int_{-\infty}^{-1}\sum_{n=2}^{\infty}e^{\imath\kappa(x+1)}P_n\left(\frac{\imath\kappa}{2(n+1)}\frac{\partial}{\partial x}\left[(x+\sqrt{x^2-1})^{n+1}\right]\right.
$$

$$
\left.+\frac{\partial}{\partial x}\left[(x+\sqrt{x^2-1})^n\right]-\frac{\imath\kappa}{2(n-1)}\frac{\partial}{\partial x}\left[(x+\sqrt{x^2-1})^{n-1}\right]\right)dx
$$

$$
-2we^{\imath\omega t}\int_{-\infty}^{-1}e^{\imath\kappa(x+1)}\left(\frac{\imath\kappa}{2}P_0+P_1\right)\frac{\partial}{\partial x}\left[(x+\sqrt{x^2-1})^1\right]dx
$$

$$
-2we^{\imath\omega t}\int_{-\infty}^{-1}e^{\imath\kappa(x+1)}\frac{\imath\kappa}{4}P_1\frac{\partial}{\partial x}\left[(x+\sqrt{x^2-1})^2\right]dx
$$

$$
= -2we^{\imath\omega t}\sum_{n=2}^{\infty}P_n\left(\int_{-\infty}^{-1}e^{\imath\kappa(x+1)}\left[1+\frac{\imath\kappa}{n}\sqrt{x^2-1}\right]\frac{\partial}{\partial x}\left[(x+\sqrt{x^2-1})^n\right]dx\right)
$$

$$
-2we^{\imath\omega t}\left(\frac{\imath\kappa}{2}P_0+P_1\right)e^{\imath\kappa}\int_1^{\infty}\left(1-\frac{x}{\sqrt{x^2-1}}\right)e^{-\imath\kappa x}dx
$$

$$
-we^{\imath\omega t}P_1\imath\kappa e^{\imath\kappa}\int_1^{\infty}\left(-2x+\frac{2x^2}{\sqrt{x^2-1}}-\frac{1}{\sqrt{x^2-1}}\right)e^{-\imath\kappa x}dx
$$

$$
= -we^{\imath\omega t}\left[\left(P_0+2\sum_{n=1}^{\infty}(-1)^n P_n\right)-2\frac{\imath\kappa}{2}e^{\imath\kappa}P_0 K_1(\imath\kappa)+2\frac{\imath\kappa}{2}e^{\imath\kappa}P_1 K_0(\imath\kappa)\right] \quad \text{(B.4)}
$$

where

$$
\frac{\imath\kappa}{2}\left(\frac{1}{n+1}\frac{\partial}{\partial x}\left[(x+\sqrt{x^2-1})^{n+1}\right]-\frac{1}{n-1}\frac{\partial}{\partial x}\left[(x+\sqrt{x^2-1})^{n-1}\right]\right)
$$

$$
= \frac{\imath\kappa}{2}\frac{(x+\sqrt{x^2-1})^n}{\sqrt{x^2-1}}\left((x+\sqrt{x^2-1})-(x+\sqrt{x^2-1})^{-1}\right)
$$

$$
= \imath\kappa(x+\sqrt{x^2-1})^n
$$

$$
= \frac{\imath\kappa}{n}\sqrt{x^2-1}\frac{\partial}{\partial x}\left[(x+\sqrt{x^2-1})^n\right] \quad \text{(B.5)}
$$

Bibliography

Abbott, I. H. and von Doenhoff, A. E.: 1959, *Theory of Wing Sections*, Dover Publications.

Adamczyk, J. J.: 1974, The passage of an infinite swept airfoil through an oblique gust, *Technical Report NASA CR-2395*, NASA.

Amiet, R. K.: 1975, Acoustic radiation from an airfoil in a turbulent stream, *J. Sound and Vibr.* **41**, 407–420.

Atassi, H. M.: 1984, The sears problem for a lifting airfoil revisited - new results, *J. Fluid Mech.* **141**, 109–122.

Batchelor, G. K.: 1967, *An introduction to fluid dynamics*, Cambridge University.

Fox, L. and Parker, I. B.: 1968, *Chebychev Polynomials in Numerical Analysis*, Oxford University Press.

Fuglsang, P., Antoniou, I., Sørensen, N. N. and Madsen, H. A.: 1998, Validation of a wind tunnel testing fascility for blade surface pressure measurements, *Technical Report Risø–R–981(EN)*, Risø National Laboratory.

Fung, Y. C.: 1969, *An introduction to the Theory of Aeroelasticity*, 2 edn, Dover.

Gaunaa, M., Fuglsang, P., Bak, C. and Antoniou, I.: 2004, Open-jet wind tunnel validation using a naca 0012 airfoil, *In: Proceedings. Special topic conference: The science of making torque from wind, Delft (NL), 19-21 Apr 2004*, Delft University of Technology, Delft, 2004, pp. 37–48.

Goldstein, M. E. and Atassi, H. M.: 1976, A complete second-order theory for the unsteady flow about an airfoil due to a periodic gust, *J. Fluid Mech.* **74**, 741–765.

Graham, J. M. R.: 1970, Lifting surface theory for the problem of an arbitrarily yawed sinusoidal gust incident on a thin aerofoil in incompressible flow, *Aero. Quart.* **XXI**, 182–198.

Guidati, G.: 2004, *Berechnung und Verminderung von Strömungsgeräuschen an Profilen*, PhD thesis, Institut für Aerodynamik und Gasdynamik Universität Stuttgart. In german.

Henderson, G.: 2005, Development of noise reduction technology for a 500 kw prototype wind turbine, *Wind Turbine Noise: Perspectives for Control*, INCE, Berlin.

Howe, M. S.: 2003, *Theory of Vortex Sound*, Cambridge University Press.

Kristensen, L. and Jensen, N. O.: 1979, Lateral coherence in isotropic turbulence and in the natural wind, *Boundary-Layer Meteorol.* **17**, 353–373.

Larose, G. L.: 1997, *The Dynamic Action of Gusty Winds on Long-Span Bridges*, PhD thesis, DTU Byg. R-029. ISBN 87-7877-088-2.

Larose, G. L.: 2003, The spatial distribution of unsteady loading due to gusts on bridge decks, *J. Wind Eng. Ind. Aerodyn.* **91**, 1431–1443.

Larose, G. L. and Mann, J.: 1998, Gust loading on streamlined bridge decks, *Journal of Fluids and Structures* **12**(5), 511–536.

Lowson, M. V.: 1994, A new prediction model for wind turbine noise, *Wind Eng.* **18**(2), 51–61.

Mann, J.: 1994a, *Models in Micrometeorology*, PhD thesis, University of Aalborg. *Risø Rep. R-727(EN)*.

Mann, J.: 1994b, Models in micrometeorology, *Technical Report Risø–R–727*, Risø National Laboratory.

Mann, J., Kristensen, L. and Courtney, M. S.: 1991, The great belt coherence experiment – a study of atmospheric turbulence over water, *Technical Report R–596*, Risø National Laboratory.

Martin, G., Mus, B. and Mus, M.: 2004, *Introduction to Sound Recording.* Purchased at http://www.tonmeister.ca/main/textbook/index.html.

McLachlan, N. W.: 1955, *Bessel Functions for Engineers*, Oxford at the Clarendon Press.

Mish, P. F. and Devenport, W. J.: 2006, An experimental investigation of unsteady surface pressure on an airfoil in turbulence–part 1: Effects of mean loading.

Moriarty, P. J., Guidati, G. and Migliore, P.: 2005, Prediction of turbulent inflow and trailing-edge noise for wind turbines, *American Institute of Aeronautics and Astronautics Paper 2005-2881*.

Moriarty, P. and Migliore, P.: 2003, Semi-empirical aeroacoustic noise prediction code for wind turbines, *Technical Report NREL/TP-500-34478*, NREL.

Mugridge, B. D.: 1971, Gust loading on a thin aerofoil, *Aero. Quart.* pp. 301–310.

Nielsen, M.: 1998, Dense gas dispersion in the atmosphere, *Technical Report Risø–R–1030(DA), note = PhD-Thesis*, Risø National Laboratory.

Oerlemans, S., Sijtsmaa, P. and López, B. M.: 2007, Location and quantification of noise sources on a wind turbine, *J. Sound and Vibr.* **299**, 869–883.

Panofsky, H. A. and Dutton, J. A.: 1984, *Atmospheric Turbulence*, John Wiley & Sons, New York.

Sears, W. R.: 1941, Some aspects of non-stationary airfoil theory and its practical application, *J. Aeron. Sc.* **8**(3), 104–108.

Theodorsen, T. and Garrick, I. E.: 1942, Nonstationary flow about a wing-aileron-tab combination including aerodynamic balance, *NACA Rept.* **736**.

von Kármán, T.: 1948, Progress in the statistical theory of turbulence, *Proc. National Akad. Sci.* **34**, 530–539.

Wagner, S., Bareiß, R. and Guidati, G.: 1996, *Wind Turbine Noise*, Springer.

Watson, G. N.: 1952, *A Treatise on the Theory of Bessel Functions*, Cambridge at the University Press.

Zhu, W. J.: 2007, *Aero-Acoustic Computations of Wind Turbines*, PhD thesis, DCAMM Special Report No. S100.

Risø DTU is the National Laboratory for Sustainable Energy. Our research focuses on development of energy technologies and systems with minimal effect on climate, and contributes to innovation, education and policy. Risø has large experimental facilities and interdisciplinary research environments, and includes the national centre for nuclear technologies.